

**INVESTIGATION ON SHOCK CELL PARAMETERS IN  
JETS EMANATING FROM CONICAL, BELL AND DOUBLE  
PARABOLIC NOZZLES**

*A THESIS*

Submitted by

**MUBARAK A. K.**

*for the award of the degree*

*of*

**DOCTOR OF PHILOSOPHY**



**DIVISION OF MECHANICAL ENGINEERING  
SCHOOL OF ENGINEERING  
COCHIN UNIVERSITY OF SCIENCE AND TECHNOLOGY, KOCHI**

**OCTOBER 2018**

**DIVISION OF MECHANICAL ENGINEERING  
SCHOOL OF ENGINEERING  
COCHIN UNIVERSITY OF SCIENCE AND TECHNOLOGY**



**CERTIFICATE**

This is to certify that the thesis entitled INVESTIGATION ON SHOCK CELL PARAMETERS IN JETS EMANATING FROM CONICAL, BELL AND DOUBLE PARABOLIC NOZZLES submitted by Mubarak A. K. to the Cochin University of Science and Technology, Kochi for the award of the degree of Doctor of Philosophy is a bonafide record of research work carried out by him under my supervision and guidance at the Division of Mechanical Engineering, School of Engineering, Cochin University of Science and Technology. The contents of this thesis, in full or in parts, have not been submitted to any other University or Institute for the award of any degree or diploma. All the relevant corrections and modifications suggested by the audience during the pre-synopsis seminar and recommended by the Doctoral committee have been incorporated in this thesis.

Kochi-22

8<sup>th</sup> October 2018

**Dr. Tide P. S.**  
(Supervising Guide)

## **DECLARATION**

I hereby declare that the work presented in the thesis entitled INVESTIGATION ON SHOCK CELL PARAMETERS IN JETS EMANATING FROM CONICAL, BELL AND DOUBLE PARABOLIC NOZZLES is based on the research work carried out by me under the supervision and guidance of Dr. Tide P. S. for the award of degree of Doctor of Philosophy with Cochin University of Science and Technology. I further declare that the contents of this thesis, in full or in parts, have not been submitted to any other University or Institute for the award of any degree or diploma.

Kochi-22

8<sup>th</sup> October 2018

Mubarak A. K.

Research Scholar

## **ACKNOWLEDGEMENTS**

All praise and thanks are due to the Almighty GOD, who always guides me to the right path, for blessing me with health, knowledge, and circumstances required for the completion of this work as well as getting along with life.

I would like to express my sincere gratitude to my supervising guide Dr. Tide P. S., Professor in Mechanical Engineering, School of Engineering, Cochin University of Science and Technology for the constant inspiration, motivation, excellent guidance, competent advice, keen observations, and persistent encouragement during the entire course of research work. I was able to successfully complete the work and deliver this thesis only because of his able guidance and immense patience. I have been extremely lucky to have a supervisor and I could not have imagined having a better advisor and mentor for my Ph. D work.

I extend my deep gratitude to Dr. Sreejith P. S., Professor and Dean, Faculty of Engineering, CUSAT for his valuable suggestions and support throughout this work. I am extremely thankful to Dr. Jayadas N. H., Professor in Mechanical Engineering, SOE, CUSAT and member of Doctoral Committee for the valuable suggestions and advices during the period of this work.

I am extremely thankful to Dr. Gireeshkumaran Thampi B. S., Head, Division of Mechanical Engineering, SOE, CUSAT for providing all sort of support including administrative for the successful completion of my thesis. I take this opportunity to thank all faculty members in the Division of Mechanical Engineering, SOE, CUSAT especially Dr. Bhasi A. B., and Dr. Biju N., for their constant support at all stages of this research. I am obliged to our Principal, Dr. M. R. Radhakrishna Panicker and office staff for all other logistical support. I would like to thank all non-teaching staff including library staff of CUSAT who have helped and supported me during the entire course of work.

The experimental part of this research was conducted at Gas Dynamics Laboratory, Indian Institute of Technology Madras. The experimentation process in this project could not have been completed without Dr. Chidambaram M., Professor, IIT Madras

and Former BoG member GEC Thrissur, Dr. Indiradevi K.P., Director DTE and Former Principal GEC Thrissur, Dr. Sheeba V.S. Former TEQIP Academic coordinator GEC Thrissur who gave the opportunity to do experiment at IIT Madras under TEQIP (Technical Education Quality Improvement Programme) Phase II scheme. I would like to gratefully thank Dr. G. Rajesh, Associate Professor, Department of Aerospace Engineering, IIT Madras for his immense help during the entire course of the experiments.

I am extremely thankful to Dr. A. Ramesh, Head, Department of Mechanical Engineering, Govt. Engineering College Thrissur for providing me the facilities in the Computational lab for my research work. I am very much grateful to Dr. B. Jayanand, Principal, GEC, Thrissur for providing all sort of support including administrative, to facilitate my study at CUSAT. I express my heartfelt thanks to Prof. Sandhya M. and Prof. Sunil A. S., my colleagues at GEC, Thrissur, and the constant companions throughout the research at CUSAT for being good friends to share my anxieties and to build up confidence throughout the course of my research. I express special thanks to Prof. Abdul Samad P. A., Prof. Jayee K. Varghese, Dr. Rekha L, and Dr. Sunilkumar C.P. my colleagues at GEC, Thrissur, for all fruitful discussions and encouraging talks. I express my heartiest gratitude to all my friends and colleagues for their support throughout my work.

I record my sincere and utmost gratitude to my parents, Mr. Kunju Moideen M. A. and Mrs. Beevi P. P. for showering love and showing faith in me. I salute you all for the selfless love, care, pain, and sacrifice you did to shape my life. Also, I express my thanks to my brothers, sisters, parents-in-law (Mr. Abdul Azees K.A. and Mrs. Amina Azeez) without whose prayers, encouragement and loving care for me, this work would not have become a reality.

Finally, let me mention the encouragement, love, and affection that I got from my beloved daughter Fiza Mariyam and son Muhammed Yaseen which had been an everlasting inspiration to complete my work at a good pace. My wife, Mrs. Sharija has been extremely supportive of me throughout this entire process and has made countless sacrifices to help me get to this point.

**MUBARAK A.K.**

## ABSTRACT

Supersonic nozzle designs for commercial aircrafts become acceptable only when they are able to meet both economic and environmental metrics, especially augmentation of thrust, minimal weight and noise suppression. Nozzle thrust optimisation has enormous practical importance as a minute fraction of increase in thrust can result in a momentous gain in payload. A novel concept of double parabolic (*DP*) nozzle has been introduced for increasing thrust by eliminating internal shock formation that causes thrust loss in conventional conical and bell nozzles.

The investigation focuses on experimental measurements and computational predictions of flow characteristics and performance of supersonic nozzles with different profiles for the divergent portion. Tests were carried out on conical, bell, and double parabolic nozzles at a design Mach number of 1.5. The divergent length of conical, bell, and double parabolic nozzle with *PM/3* profile was kept the same for the sake of comparison. The throat diameter of the nozzles was kept identical as 20 mm and the nozzles were designed for a Mach number of 1.5. The double parabolic nozzle with *PM/3* profile has been designed in such a way that the maximum slope of the divergent portion of the convergent-divergent nozzle is taken as one-third of the Prandtl-Meyer (*PM*) angle. The studies were conducted at different nozzle pressure ratios (*NPRs*) such as 3.7, 4.5, 5, and 5.5. The flow characteristics were measured by using static/stagnation pitot probes and visualization by Schlieren imaging technique. It was observed that the nozzle exit pressure of the double parabolic nozzle was close to atmospheric at design condition, whereas conical and bell nozzles exhibited slightly higher values than atmospheric.

Numerical simulations were carried out in a two-dimensional computational domain incorporating density based solver with *RANS* equations and *SST k- $\omega$*  turbulence model. The predictions were found to be in reasonable agreement with the measured experimental data. It was observed that the shock cell length and shock cell count are almost same for double parabolic nozzle with different Prandtl Meyer expansion angles in the divergent portion of the nozzle. Both potential core and supersonic core lengths increase with increasing nozzle pressure ratios. It has been observed that the nozzle discharge/thrust coefficients of all nozzles decrease with increasing *NPR* and *DP* nozzle with *PM/3* profile has the highest magnitude for these parameters.

The effect of maximum expansion angle in the diverging portion of a double parabolic nozzle was also investigated experimentally and numerically. Double parabolic nozzles with different expansion angles such as one-third, one-fourth, and one-fifth of Prandtl-Meyer angles (*PM/3*, *PM/4*, and *PM/5*) were developed. However, the lengths of the nozzles are different due to the variation in divergence angle and hence *DP* nozzle with *PM/3* profile is having the least length among the three different profiles under study. The thrust coefficient and discharge coefficient are found to be same for double parabolic nozzles with different PM expansion profiles. However, *DP* nozzle with *PM/3* profile has the least length and in turn minimum weight making it favourable for aerospace applications. The double parabolic nozzle with *PM/3* profile has 1.01% shorter potential core length, 1.08% shorter shock cell length, 1.18% lesser shock wave angle, 1% larger thrust coefficient and 0.27% larger discharge coefficient. After analysing the flow and performance characteristics together with the benefit of weight, the double parabolic nozzle with *PM/3* profile seems to be better than conventional conical and bell nozzles.

# CONTENTS

ACKNOWLEDGEMENTS	i-ii
ABSTRACT	iii-iv
LIST OF TABLES	viii-ix
LIST OF FIGURES	x-xiv
LIST OF ABBREVIATIONS	xv
LIST OF NOMENCLATURE	xvi-xvii
<b>CHAPTER 1 INTRODUCTION</b>	<b>1-5</b>
1.1 Jet Dynamics of Supersonic Flows	1
1.2 Thesis Outline	4
<b>CHAPTER 2 LITERATURE SURVEY</b>	<b>6-41</b>
2.1 Nozzle Design	7
2.1.1 Conical Nozzle	8
2.1.2 Ideal Contour Nozzle	10
2.1.3 Truncated Ideal Contour Nozzle	13
2.1.4 Thrust Optimised Contour Nozzle	14
2.1.5 Losses in Nozzle	22
2.1.6 Supersonic Jet Flow	23
2.1.7 Shock cell Parameters	24
2.2 Experimental Works	25
2.3 Numerical Simulations	33
2.4 Motivation	36
2.5 Scope of Present Work	40
<b>CHAPTER 3 NOZZLE DESIGN AND MANUFACTURING</b>	<b>42-54</b>
3.1 Nozzle Design	42
3.1.1 Double Parabolic Nozzle	43
3.1.1.1 Double Parabolic <i>PM/3</i> Nozzle	44
3.1.1.2 Double Parabolic <i>PM/4</i> Nozzle	47
3.1.1.3 Double Parabolic <i>PM/5</i> Nozzle	48
3.1.2 Bell Nozzle	49
3.1.3 Conical Nozzle	50
3.1.4 Convergent Portion of the Nozzle	51
3.2. Nozzle Fabrication	51
<b>CHAPTER 4 EXPERIMENTATION ON SUPERSONIC NOZZLES</b>	<b>55-63</b>
4.1 Supersonic Free Jet Facility	55
4.1.1 Compressor	55



4.1.2	Storage Tank -----	56
4.1.3	Settling Chamber and Pressure Regulating Valve -----	56
4.1.4	Nozzles -----	57
4.2	Experimental Measurement Techniques -----	58
4.2.1	Pressure Measuring Devices -----	58
4.2.2	Schlieren Set-up -----	59
4.3	Experimentation on Nozzles -----	60
<b>CHAPTER 5      NUMERICAL MODELLING &amp; SIMULATION -----</b>		<b>64-74</b>
5.1	Governing Equations -----	64
5.2	Turbulence Modelling -----	65
5.2.1	Closure Problem in Turbulence -----	65
5.2.2	Boussinesq's Hypothesis -----	66
5.2.3	Standard $k-\varepsilon$ Model -----	67
5.2.4	<i>RNG</i> $k-\varepsilon$ Model -----	68
5.2.5	Realizable $k-\varepsilon$ Model -----	68
5.2.6	<i>SST</i> $k-\omega$ Model -----	69
5.3	Numerical Simulations -----	70
5.3.1	Domain Selection and Mesh Generation -----	70
5.3.2	Results and Discussions -----	71
<b>CHAPTER 6      COMPARISON OF DOUBLE PARABOLIC NOZZLE WITH <i>PM/3</i> PROFILE WITH CONICAL AND BELL NOZZLES -----</b>		<b>75-112</b>
6.1	Experimental Measurements & Analysis -----	75
6.1.1	Static Pressure -----	75
6.1.2	Mach Number -----	78
6.1.3	Schlieren Image -----	79
6.2	Numerical Procedure & Analysis -----	86
6.2.1	Governing Equations -----	86
6.2.2	Geometry and Boundary Conditions -----	88
6.2.3	Discretisation and Grid Independence Study -----	89
6.3	Nozzle Flow Characteristics -----	92
6.4	Nozzle Performance Parameters -----	97
6.4.1	Shock Cell Length -----	98
6.4.2	Shock Wave Angle -----	102
6.4.3	Shock Cell Count -----	102
6.4.4	Potential Core Length -----	104
6.4.5	Supersonic Core Length -----	106
6.4.6	Nozzle Thrust -----	109
6.4.7	Nozzle Thrust Coefficient -----	110

6.4.8	Nozzle Discharge Coefficient -----	111
-------	------------------------------------	-----

**CHAPTER 7      EFFECT OF THE MAXIMUM EXPANSION ANGLE  
IN THE DIVERGENT PORTION OF A DOUBLE  
PARABOLIC NOZZLE -----113-129**

7.1	Introduction -----	113
7.2	Experimental Analysis-----	114
7.2.1	Static & Stagnation Pressure Measurements -----	114
7.2.2	Mach Number-----	115
7.2.3	Schlieren Image-----	116
7.3	Numerical Analysis -----	118
7.4	Nozzle Performance Parameters -----	121
7.4.1	Shock Cell Length-----	121
7.4.2	Shock Cell Count-----	124
7.4.3	Potential Core Length-----	126
7.4.4	Nozzle Thrust -----	127
7.4.5	Nozzle Thrust and Discharge Coefficients -----	128
7.5	Summary-----	128

**CHAPTER 8      CONCLUSIONS -----130-135**

8.1	Experimental & Numerical Analysis of Performance Parameters of Conical, Bell, and Double Parabolic Nozzles-----	130
8.2	Effect of Expansion Angle in the Divergent Portion of Double Parabolic Nozzles-----	134
8.3	Future Work-----	135

**REFERENCES ----- 136-145**

**LIST OF PUBLICATIONS**

**CURRICULUM VITAE**

## LIST OF TABLES

Table	Title	Page
2.1	Momentum correction factor for conical nozzles (Sutton and Biblarz, 2010)-----	9
2.2	Comparison of nozzle contour type -----	22
3.1	Nozzle coordinates of $PM/3$ -----	46
3.2	Nozzle coordinates of $PM/4$ -----	48
3.3	Nozzle coordinates of $PM/5$ -----	49
3.4	Nozzle coordinates of Bell-----	50
3.5	Coordinates of the convergent portion of the $CD$ nozzle-----	51
6.1	Boundary and operating conditions when the nozzle is operated at design conditions-----	89
6.2	Variation of shock cell lengths of conical, bell, and $PM/3$ double parabolic nozzles at $NPRs$ 4.5, 5, and 5.5 -----	101
6.3	Variation of shock wave angle of conical, bell, and double parabolic ( $PM/3$ ) nozzles at $NPRs$ of 4.5, 5, and 5.5-----	102
6.4	Potential core length of conical, bell, and $PM/3$ double parabolic nozzles at $NPRs$ 4.5, 5, and 5.5 -----	106
6.5	Variation of supersonic core lengths of conical, bell and $PM/3$ double parabolic nozzles at $NPRs$ 4.5, 5, and 5.5 -----	109
6.6	Thrust generation of conical, bell and $PM/3$ double parabolic nozzles at $NPRs$ 4.5, 5, and 5.5 -----	110
6.7	Variation of nozzle thrust coefficients of conical, bell, and $PM/3$ double parabolic nozzles at $NPRs$ 4.5, 5, and 5.5 -----	111
6.8	Variation of nozzle discharge coefficients of conical, bell, and $PM/3$ double parabolic nozzles at $NPRs$ 4.5, 5, and 5.5-----	112

7.1	Variation of shock cell lengths of the double parabolic nozzles with $PM/3$ , $PM/4$ , and $PM/5$ profiles at $NPRs$ 4.5, 5, and 5.5 -----	124
7.2	Potential core length of the double parabolic nozzles with $PM/3$ , $PM/4$ , and $PM/5$ profiles at $NPRs$ 4.5, 5, and 5.5 -----	126
7.3	Thrust generation of the double parabolic nozzles with $PM/3$ , $PM/4$ , and $PM/5$ profiles at $NPRs$ 4.5, 5, and 5.5 -----	127
7.4	Nozzle thrust coefficients of the double parabolic nozzles with $PM/3$ , $PM/4$ , and $PM/5$ profiles at $NPRs$ 4.5, 5, and 5.5 -----	127

## LIST OF FIGURES

Figure	Title	Page
2.1	Flow through different nozzles at various operating conditions (Sutton and Biblarz, 2010)-----	11
2.2	Basic flow structures in an Ideal Contoured nozzle (Ostlund, 2002)-----	11
2.3	Basic flow structures in a Thrust Optimised Contoured nozzle (Ostlund, 2002)-----	15
2.4	Length comparison with different types of nozzles (Rao, 1961)-----	16
2.5	Flow inside axisymmetric Minimum Length Nozzle (Zebbiche, 2011)-----	18
2.6	TOP nozzle based on Rao's approximation (Kulhanek, 2012)-----	20
2.7	Variation of $\theta_i$ and $\theta_e$ with $\varepsilon$ and KL (Meerbeek, 2013)-----	21
2.8	Flow over the initial length of a supersonic jet (Zapryagaev <i>et al.</i> , 2018)-----	24
2.9	Structure of shock cells (Mehta and Prasad, 1996)-----	24
2.10	(a) Formation of weak shocks-----	27
	(b) Formation of coalescing shocks-----	27
	(c) Formation of reflecting shocks-----	27
3.1	Contours of different nozzle configurations-----	44
3.2	Nozzles used for experimentation-----	52
3.3	(a) Machine drawing of conical nozzle-----	52
	(b) Machine drawing of bell nozzle-----	53
	(c) Machine drawing of $PM/3$ double parabolic nozzle-----	53
	(d) Machine drawing of $PM/4$ double parabolic nozzle-----	53
	(e) Machine drawing of $PM/5$ double parabolic nozzle-----	54
4.1	Compressor-----	56
4.2	Storage tanks-----	56
4.3	Settling chamber-----	57
4.4	$CD$ nozzles used for experiments-----	57
4.5	(a) Static pitot probe (b) Stagnation pitot tube-----	58
4.6	Three-axis traverse-----	59

4.7	Z-type Schlieren system -----	60
4.8	(a) Photron <i>FASTCAM</i> viewer (b) <i>DAQ</i> system -----	60
4.9	Schematic diagram of the experimental set-up- -----	61
4.10	Experimental measurement locations (660 positions) -----	62
4.11	Typical static pressure signal during centreline Pitot pressure measurement -----	62
5.1	Domain with boundary conditions -----	71
5.2	Comparison of density (numerical) along the jet axis from nozzle exit with experimental data-----	72
5.3	Comparison of the radial profile of density (numerical) at $2D_e$ from nozzle exit with experimental data-----	73
5.4	Comparison of the radial profile of temperature (numerical) at $6D_e$ from nozzle exit with experimental data-----	73
5.5	Comparison of the radial profile of velocity (numerical) at $8D_e$ from nozzle exit with experimental data-----	74
6.1	Comparison of pressure variation along the jet axis for different nozzles at $NPR = 3.7$ (Experimental)-----	76
6.2	Comparison of pressure variation along the jet axis for different nozzles at $NPR = 5$ (Experimental)-----	77
6.3	Comparison of pressure variation along the jet axis for different nozzles at $NPR = 3.7$ (Experimental)-----	78
6.4	Comparison of Mach number variation along the jet axis for different nozzles at $NPR = 5$ (Experimental)-----	79
6.5	Schlieren images of conical, bell, and double parabolic nozzle with $PM/3$ profile at $NPR = 3.7$ (Experimental) -----	80
6.6	Schlieren images of conical, bell, and double parabolic nozzle with $PM/3$ profile at $NPR = 4.5$ (Experimental) -----	81
6.7	Schlieren images of conical, bell, and double parabolic nozzle with $PM/3$ profile at $NPR = 5$ (Experimental) -----	81
6.8	Schlieren images of conical, bell, and double parabolic nozzle $PM/3$ profile at $NPR = 5.5$ (Experimental) -----	82

6.9	Schlieren images of flow through the conical nozzle at an interval of 0.000278 sec at $NPR = 3$ (Experimental)-----	83
6.10	Schlieren images of flow through the conical nozzle at an interval of 0.000278 sec at $NPR = 3.7$ (Experimental) -----	83
6.11	Schlieren images of flow through the conical nozzle at an interval of 0.000278 sec at $NPR = 4.5$ (Experimental) -----	84
6.12	Schlieren images of flow through the conical nozzle at an interval of 0.000278 sec at $NPR = 5$ (Experimental)-----	84
6.13	Schlieren images of flow through the conical nozzle at an interval of 0.000278 sec at $NPR = 5.5$ (Experimental) -----	85
6.14	Computational domain with boundary conditions-----	88
6.15	(a) Computational grid at the nozzle exit -----	89
	(b) Total computational grid-----	90
6.16	Variation in nozzle exit pressure with grid size for the double parabolic nozzle with $PM/3$ profile at $NPR = 5$ -----	91
6.17	Grid independence study on the nozzle core region of the double parabolic nozzle with $PM/3$ profile at $NPR = 5$ -----	91
6.18	Comparison of experimental data and numerical predictions of pressure variation along the jet axis of different nozzles at $NPR = 3.7$ (a) Conical (b) Bell (c) Double parabolic ( $PM/3$ ) -----	93
6.19	Comparison of experimental data and numerical predictions of Mach number variation along the jet axis of different nozzles at $NPR = 3.7$ (a) Conical (b) Bell (c) Double parabolic ( $PM/3$ )-----	94
6.20	Comparison of experimental data and numerical predictions of pressure variation along the jet axis of different nozzles at $NPR = 5$ (a) Conical (b) Bell (c) Double parabolic ( $PM/3$ ) -----	95
6.21	Comparison of experimental data and numerical predictions of Mach number variation along the jet axis of different nozzles at $NPR = 5$ (a) Conical (b) Bell (c) Double parabolic ( $PM/3$ ) -----	96
6.22	Pitot pressure and Schlieren image comparison for the double parabolic nozzle with $PM/3$ profile at $NPR = 5$ -----	98

6.23	Comparison of Schlieren images of the conical nozzle at <i>NPRs</i> of 4.5, 5, and 5.5 (Experimental)-----	100
6.24	Comparison of Schlieren images of the bell nozzle at <i>NPRs</i> of 4.5, 5, and 5.5 (Experimental)-----	100
6.25	Comparison of Schlieren images of the double parabolic nozzle with <i>PM/3</i> profile at <i>NPRs</i> of 4.5, 5, and 5.5 (Experimental)-----	101
6.26	Velocity contours (m/s) of conical, bell, and the double parabolic nozzle with <i>PM/3</i> profile at <i>NPR</i> = 5 (Numerical) -----	103
6.27	Pressure contours (Pa) of the double parabolic nozzle with <i>PM/3</i> profile at <i>NPRs</i> of 4.5, 5, and 5.5 (Numerical)-----	103
6.28	Density contours ( $\text{kg/m}^3$ ) of the double parabolic nozzle with <i>PM/3</i> profile at <i>NPRs</i> of 4.5, 5, and 5.5 (Numerical) -----	104
6.29	Variation of <i>u/uj</i> centreline of the double parabolic nozzle with <i>PM/3</i> profile along the jet axis at <i>NPR</i> = 4.5, 5 and 5.5 -----	105
6.30	Variation of <i>u/uj</i> centreline of the conical nozzle along the jet axis at <i>NPRs</i> 4.5, 5, and 5.5 -----	105
6.31	Comparison of the mean axial velocity of different nozzles at <i>NPR</i> = 5 -----	106
6.32	Variation of centreline Mach number of the double parabolic nozzle with <i>PM/3</i> profile along the jet axis at <i>NPR</i> = 4.5, 5, and 5.5-----	107
6.33	Variation of centreline Mach number of the conical nozzle along the jet axis at <i>NPRs</i> 4.5, 5 and 5.5 -----	107
6.34	Total pressure decay of the double parabolic nozzle with <i>PM/3</i> profile along the jet axis at <i>NPR</i> = 4.5, 5, and 5.5 -----	108
6.35	Total pressure decay of conical nozzle along the jet axis at <i>NPRs</i> 4.5, 5, and 5.5 -----	108
7.1	Pressure variation along the jet axis for different nozzles at <i>NPR</i> = 3.7 (Experimental)-----	114
7.2	Pressure variation along the jet axis for different nozzles at <i>NPR</i> = 5 (Experimental) -----	115



7.3	Mach number variation along the jet axis for different nozzles at $NPR = 3.7$ (Experimental) -----	116
7.4	Mach number variation along the jet axis for different nozzles at $NPR = 5$ (Experimental)-----	116
7.5	Schlieren images of $PM/3$ , $PM/4$ , and $PM/5$ nozzles at $NPR = 4.5$ (Experimental) -----	117
7.6	Schlieren images of double parabolic nozzles with $PM/3$ , $PM/4$ , and $PM/5$ profiles at $NPR = 5$ (Experimental)-----	117
7.7	Schlieren images double parabolic nozzles with $PM/3$ , $PM/4$ , and $PM/5$ profiles at $NPR = 5.5$ (Experimental)-----	118
7.8	Comparison of experimental data and numerical predictions of pressure variation along the jet axis of different nozzles at $NPR = 5$ (a) $PM/3$ (b) $PM/4$ (c) $PM/5$ -----	119
7.9	Experimental data and numerical predictions of Mach number variation along the jet axis of different nozzles at $NPR = 5$ (a) $PM/3$ (b) $PM/4$ (c) $PM/5$ -----	120
7.10	Schlieren images of the double parabolic nozzle with $PM/3$ profile at $NPRs$ of 4.5, 5 and 5.5 (Experimental) -----	122
7.11	Schlieren images of the double parabolic nozzle with $PM/4$ profile at $NPRs$ of 4.5, 5 and 5.5 (Experimental) -----	123
7.12	Schlieren images of the double parabolic nozzle with $PM/5$ profile at $NPRs$ of 4.5, 5 and 5.5 (Experimental) -----	123
7.13	Velocity contours (m/s) of the double parabolic nozzles with $PM/3$ , $PM/4$ , and $PM/5$ profiles at $NPR = 5$ (Numerical) -----	125
7.14	Density contours ( $kg/m^3$ ) of the double parabolic nozzles with $PM/3$ , $PM/4$ , and $PM/5$ profiles at $NPR = 5$ (Numerical) -----	125
7.15	Comparison of the mean axial velocity of the double parabolic nozzles with $PM/3$ , $PM/4$ , and $PM/5$ profiles at $NPR = 5$ -----	126

## LIST OF ABBREVIATIONS

CARS	Coherent Anti-Stokes Raman Spectroscopy
CD	Convergent Divergent
CFD	Computational Fluid Dynamics
CMOS	Complementary Metal Oxide Semiconductor
CTIC	Compressed Truncated Ideal Contour
CTP	Compressed Truncated Perfect
DP	Double Parabolic
FSS	Free Shock Separation
IC	Ideal Contour
ICAO	International Civil Aviation Organisation
LES	Large Eddy Simulation
MLN	Minimum Length Nozzle
MOC	Method of Characteristics
NPR	Nozzle Pressure Ratio
PIV	Particle Image Velocimetry
RANS	Reynolds Averaged Navier-Stokes
RSM	Reynolds Stress Model
RSS	Restricted Shock Separation
SST	Shear Stress Transport
TIC	Truncated Ideal Contour
TOC	Thrust Optimised Contoured
TOP	Thrust Optimised Parabolic
QTH	Quartz Tungsten Halogen

## NOMENCLATURE

$A$	Area	$m^2$
$A_e$	Exit area	$m^2$
$A_t$	Throat area	$m^2$
$C_d$	Discharge coefficient	
$C_f$	Thrust coefficient	
$D$	Diameter	m
$D_j$	Jet diameter	m
$D_t$	Throat diameter	m
$F$	Thrust	N
$I_{sp}$	Specific impulse	$s^{-1}$
$k$	Turbulent kinetic energy	$m^2/s^2$
$L_n$	Nozzle length	m
$\dot{m}$	Mass flow rate	kg/s
$M$	Mach number	
$n$	Refractive index	
$p$	Pressure	Pa
$p_a$	Ambient pressure	Pa
$p_e$	Exit pressure	Pa
$p_t$	Throat pressure	Pa
$p_0$	Stagnation Pressure	Pa
$R$	Characteristic gas constant	J/kgK
$r$	Radial coordinates	m
$T$	Temperature	K
$t$	Time	s
$u, v, w$	Velocity components in Cartesian coordinates	m/s
$u', v', w'$	Fluctuating velocity components in Cartesian coordinates	m/s

$\rho$	Density	$\text{kg/m}^3$
$\mu$	Dynamic viscosity	$\text{Pa}\cdot\text{s}$
$\nu$	Kinematic viscosity	$\text{m}^2/\text{s}$
$\mu_t$	Turbulent viscosity	$\text{m}^2/\text{s}$
$\delta_{ij}$	Kronecker delta	
$\varepsilon$	Viscous dissipation rate	$\text{m}^2/\text{s}^3$
$\omega$	Specific rate of dissipation of turbulent kinetic energy	$\text{s}^{-1}$
$\gamma$	Ratio of specific heats	
$\lambda$	Shock cell length	$\text{m}$
$\lambda_m$	Momentum correction factor	
$\alpha$	Half cone angle	0

# **CHAPTER - 1**

## **INTRODUCTION**

### **1.1 JET DYNAMICS OF SUPERSONIC FLOWS**

The current need of achievement of better performance, environmental and economical benefits of aircraft and rocket engines lead to an optimum design of supersonic nozzle. Conical nozzles are simple in design and construction but are very long and heavy. Even though bell nozzle gives a better performance than conical, internal shocks are formed in the spherical to the transition region of the parabola. Avoiding these internal shocks in the divergent section will lead to better thrust and performance. Supersonic nozzle designs for commercial aircrafts become acceptable only when they are able to meet both economical and environmental metrics. Usually, economical metrics are associated with thrust, weight and mechanical complexity whereas environmental metrics are associated with noise (Seiner and Gilinsky, 1997). Nozzle thrust optimisation has enormous practical importance, as a minute fraction of increase of jet nozzle thrust can result in a momentous gain in payload and thereby satisfy economical metrics.

The flow characteristics of a supersonic nozzle jet such as shock cell length, shock cell count, potential core length etc. have great importance in economical and environmental aspects. The shock cell parameters can be found by pressure measurements along the jet flow and also from Schlieren images. By linking the pressure measurements and Schlieren images, an insight into the jet flow development and dynamics will be obtained. These images provide the intricate phenomenon happening in the trailing shock diamond downstream of the jet.

High-speed jets are issued out of the nozzles from supersonic aircraft engines and rocket engines. Mostly these engines work in over expanded or under expanded mode with shock cells leading to shock diamonds developed in the jet core. The shock cell strength depends on nozzle design Mach number and fully expanded Mach number. This type of dependence is valid only over a very limited range of off-design Mach numbers. For moderately imperfectly expanded jets, this relation is highly non-linear. *CFD* plays a major role in the analysis of these types of jets. The numerical solution of exhaust flow from a supersonic nozzle is a challenging problem in fluid dynamics. The computational analysis based on the solution of Reynolds Averaged Navier-Stokes (*RANS*) equations and the execution of an appropriate turbulence model for closure of *RANS* equations. In the case of viscous flows, an algebraic model is enough as the turbulent viscosity is determined by local function. Two equations with second-order closure are used for investigating complex viscous flow features such as separated flow and shear layer. Hamed and Vogiatzist (1997) have carried out a *2D* simulation with the algebraic turbulence models of *RNG*, one equation model of Baldwin-Barth and the two equation  $k-\epsilon$  and  $k-\omega$  models of Chien and Wilcox. They noticed that the pressure variation and shock position are firmly affected by the turbulence model. The perception of jet development by numerical simulation and its analysis without the aid of huge and expensive experimental set up enables the manufacturers to design and develop novel concepts quickly.

Current researches in the aerospace industry focus on the development of nozzles which gratify economical and environmental constraints such as thrust augmentation and noise reduction. The imperative use of supersonic jet and rocket engines leads to great attention on the optimisation of supersonic nozzles. The quality of expansion

produced in the divergent portion of the supersonic nozzle has a direct impact on the performance of propulsion vehicle. The thrust produced by the exhaust gases mainly depends on the way of expansion in the divergent portion. For achieving the maximum thrust the nozzle exit pressure should be the same as ambient, once the complete expansion of gases is completed. Such conical nozzles were heavy and widely used in rocket propulsion because of its simplicity and ease of construction. Later, conical nozzles were replaced with bell nozzles and presently bell nozzles have wide application in the aerospace industry. However, in the case of bell nozzle also, shock formation persists in the divergent portion near the meeting point of arc and parabola.

Common main stage rocket nozzles are designed at sea-level conditions, to avoid flow separation and undesired side loads. Hence the study of flow structure at design and under-expanded condition seems to be very significant in the calculation of thrust. The flow characteristics which are the major contributor to thrust and noise can be obtained from Schlieren images and pressure measurements. This led to the experimentation on different nozzle configurations to determine the shock cell parameters such as shock cell length, shock cell count, shock wave angle etc. by using Schlieren imaging techniques and static/stagnation probe measurements downstream of the flow.

The *CFD* analysis of supersonic jet flow is a challenging problem in aerospace industry. The jet flow solution may be obtained with an appropriate turbulence model for the closure of *RANS* equations. Different turbulence model can be used for numerical study ranging from algebraic to linear and non linear turbulence models. The accuracy of the numerical prediction of flow characteristics mainly depends on

the turbulence model employed. In order to accomplish a comprehensive study on the dynamic of supersonic jets, the flow characteristics and performance analysis have to be carried out meticulously both experimentally and numerically.

## **1.2 THESIS OUTLINE**

Chapter 1 provides an introduction to the current status of researches in nozzle design, experimental and numerical analysis of supersonic flow and performance characteristics.

A detailed review of the available literature on different nozzle profiles, experimental measurements and numerical simulations of supersonic flow is presented in Chapter 2. The scope of the work is derived from motivation on a wider perspective.

Chapter 3 describes the procedure for the design and manufacture of conical, bell and double parabolic nozzles at a designed Mach number of 1.5.

Chapter 4 illustrates the experimentation of these different nozzle configurations developed using a supersonic free jet test facility and Schlieren apparatus.

Numerical modelling and simulation are explained in Chapter 5, starting from the governing equations, domain and grid generation, turbulence modelling and solution techniques. Selection of an appropriate turbulence model suited for predicting mean flow parameters of the supersonic jet has also been explained in this Chapter.

Chapter 6 compares the flow behaviour and performance metrics of conical, bell and double parabolic nozzle with  $PM/3$  profile obtained from the experimental data and numerical predictions at different nozzle pressure ratios.



Chapter 7 describes the effect of the maximum expansion angle in the diverging portion of the double parabolic nozzle on the flow and performance characteristics.

Chapter 8 presents the overall conclusion of experimental and numerical studies and also the scope for future work.

## **CHAPTER - 2**

### **LITERATURE SURVEY**

Aerospace industry focuses on the development of more efficient thrust augmented aircraft engines and also consistent methods of bringing payloads into orbit economically. The four major systems of the rocket engines are the structural system, payload system, guidance system, and propulsion system. The nozzle is one of the major components of the propulsion system. Rocket nozzles are used to expand the combustion products from the combustion chamber to high velocities by converting potential and internal energy to kinetic energy. The thrust produced by the engine depends on the mass flow rate through the nozzle, exit velocity, and pressure relative to the ambient.

The hot flue gases from the combustion chamber enter the convergent portion of the nozzle which accelerates the flow to attain a unit Mach number at the throat. The throat is the part of the nozzle where the area of cross-section is a minimum. The flow is said to be choked when it attains a unit Mach number at the throat and the maximum mass flow rate is obtained at that particular upstream conditions. The flow later enters the divergent section of the nozzle downstream of the throat, which is the main focus of the modern nozzle study. In the divergent portion, the flow is accelerated to supersonic velocities and the static pressure of the gas decreases.

The factors affecting the nozzle efficiency are viscous losses in the internal boundary layer, flow separation, and the exit pressure. In the case of an ideal contoured nozzle, the maximum efficiency is achieved when the gas is expanded isentropically and pressure at the exit plane of the nozzle is same as atmospheric pressure. However

ambient pressure is a function of altitude. Conventional nozzles are designed to be exquisitely expanded at one mid-range altitude. So these nozzles are overexpanded at low altitude and underexpanded at high altitudes (Ostlund, 2002). If the nozzle is designed at sea level, it works at underexpanded conditions for all altitudes. In underexpanded condition, the exhaust gases expand even after it leaves the nozzle exit and results in a significant loss of thrust and engine efficiency (Genin and Stark, 2009).

## **2.1 NOZZLE DESIGN**

The nozzle is a device which is used for producing thrust by transforming the energy from expanded gases travelling at high speeds. The convergent portion of a Convergent-Divergent (*CD*) nozzle is encountering favourable pressure gradient and hence profile has not much significance in the flow characteristics. However, the profile of the divergent portion of the nozzle significantly affects the flow characteristics and thrust. The gain or loss of specific impulse of nozzle decides the gain or loss of several hundreds of kilograms of payload (Yang *et al.*, 2004). Maximum thrust can be achieved by the complete expansion of the gases to the ambient pressure through the nozzle with a parallel uniform flow at the nozzle exit. This can be achieved by increasing the length of the divergent portion keeping the angle of divergence a minimum. A long nozzle is required to maximise the geometric efficiency at ideal conditions with a penalty on the nozzle drag. But high-speed vehicles must be compact with minimum space and weight requirements. Hence minimum length nozzles got much acceptance and practical importance. Nowadays the design of the divergent portion of the *CD* nozzle has received major attention in order to enhance thrust and efficiency. In the subsequent sections, a review on the nozzle design based on the divergent profile is analysed for different nozzle configurations mentioned below.

- Conical Nozzle
- Ideal Contoured Nozzle
- Truncated Ideal Contoured Nozzle
- Thrust Optimised Nozzle

### 2.1.1 Conical Nozzle

Conical nozzles are widely used in rocket propulsions due to its simplicity and ease of construction. A small cone angle produces a greater thrust as it maximises axial component and therefore specific impulse. However, it is too long due to low values of divergence angle. The major effects of increasing nozzle divergence angle are flow divergence and thrust reduction as the flow is not aligned with the nozzle axis. In the case of a conical nozzle a theoretical correction factor  $\lambda$ , which is the ratio between the momentum of the gas in the conical nozzle and the momentum corresponding to the ideal nozzle with all gases flowing in the axial direction, can be introduced. The correction factor can be obtained from Equation 2.1 where  $\alpha$  is the half cone angle.

$$\lambda_m = \frac{1}{2}(1 + \cos \alpha) \quad (2.1)$$

Table 2.1 shows the variation of  $\lambda_m$  with different values of  $\alpha$ . The value of the correction factor  $\lambda_m$  for ideal rockets is unity. It is clear from the table that the exit velocity and therefore exit momentum will be reduced to 96.98% for a conical nozzle with a cone angle of  $40^\circ$ , when compared with the value calculated from Equation 2.2. It is applicable only to momentum thrust and not to pressure thrust. However, the total thrust is the sum of pressure thrust and momentum thrust.

$$v_2 = \sqrt{\left(\frac{2\gamma}{\gamma-1}RT_1 \left[1 - \left(\frac{p_2}{p_1}\right)^{\frac{\gamma}{\gamma-1}}\right] + v_1^2\right)} \quad (2.2)$$

Table 2.1: Momentum correction factor for conical nozzles (Sutton and Biblarz, 2010)

Half cone angle, $\alpha$ in degree	Correction factor, $\lambda_m$
0	1.0000
2	0.9997
4	0.9988
6	0.9972
8	0.9951
10	0.9924
12	0.9890
14	0.9851
16	0.9806
18	0.9755
20	0.9698

When a conical nozzle discharges into vacuum the thrust coefficient can be calculated from Equation 2.3.

$$C_{f_{\text{conical}}} = \frac{p_e A_e}{p_c A_t} + \left(\frac{1+\cos \alpha}{2}\right) \frac{\rho_e V_e^2 A_e}{p_c A_t} \quad (2.3)$$

The thrust produced can be calculated from Equation 2.4

$$F = (\dot{m}v_e + p_e A_e) - p_a A_e = C_f p_c A_t = \dot{m} I_{sp} \quad (2.4)$$

where  $\dot{m}$  is the mass flow rate of the engine,  $C_f$  is the thrust coefficient,  $v_e$  is the averaged value of velocity over the nozzle exit area ( $A_e$ ),  $p_e$  is the averaged value of pressure over the nozzle exit area and  $I_{sp}$  is the specific impulse in m/s.

Rao (1958) suggested that due to the nonuniformity of flow in the nozzle throat resulting from the configuration geometry yields critical section area at nozzle throat which is less than the plane cross-sectional area at nozzle throat  $A_t$ . The performance of conical nozzles depends on wall angle, area expansion ratio, and thermodynamic properties. Samitha *et al.* (2007) carried out experiments on conical and wave-shaped nozzles and found that the momentum flux is higher at the central core and then decreases in the radial direction up to the wall of the conical nozzle. Migdal and Landis (1962) pointed out that the conventional conical nozzles are not shock free. Cuppoletti *et al.* (2014) made certain modifications at the throat by varying curvature to eliminate shocks by providing overturning of flow. Due to high-performance losses of conical nozzles, these nozzles are currently being replaced with bell nozzles (Huzel and Huang, 1992). Contoured nozzle gives more uniform flow with a higher average Mach number at nozzle exit than that of a conical nozzle (Mehta *et al.*, 2012).

### **2.1.2 Ideal Contour Nozzle**

The thrust of a conical nozzle decreases with an increase in nozzle cone angle and in turn a reduction in length. This is primarily because of the nonparallel flow of the jet along the nozzle axis at the exit. By contouring the nozzle profile, the flow can be turned closer to axial direction and losses in momentum thrust can be reduced. In the overexpanded mode, the exhaust plume separates from the nozzle wall before the nozzle lip. This flow separation inside the nozzle produces dangerous side loads. Side loads are caused by the interaction between internal shocks and the boundary layer of the separated flow. The conical nozzle at overexpanded condition shows such phenomenon (Figure 2.1). In the case of a bell nozzle, the flow at the exit is nearly axial. Several methods are available for contouring divergent portion of the nozzle.

The Ideal Contour (IC) nozzle is constructed by using the direct-design techniques based on Methods of Characteristics (MOC) (Anderson, 1997). Figure 2.2 shows an outline of flow through an ideal contoured nozzle. In Figure 2.2, contour  $TNE$  is the divergent portion of the nozzle and  $TN$  is the initial expansion region.

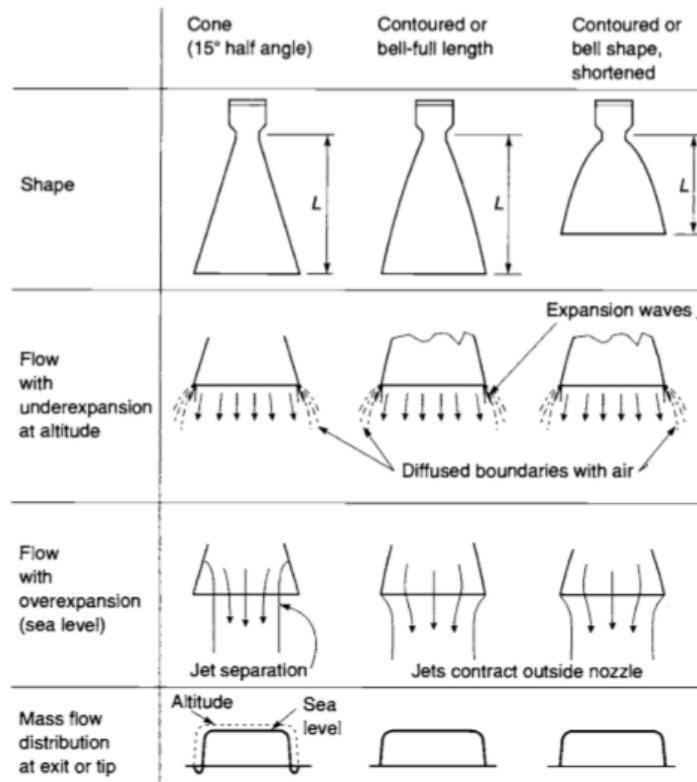


Fig. 2.1 Flow through different nozzles at various operating conditions (Sutton and Biblarz, 2010)

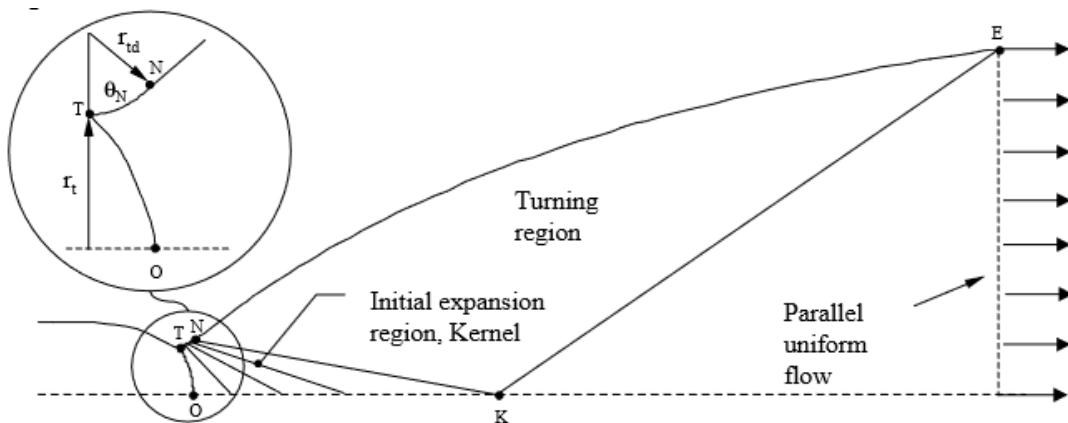


Fig. 2.2 Basic flow structures in an Ideal Contoured nozzle (Ostlund, 2002)

After the initial expansion, the contour  $NE$  turns the flow over to axial direction. At point  $K$  the Mach number is the same as that of nozzle exit and is defined by  $TN$ . The streamline between  $N$  and  $E$  is constructed with the use of  $MOC$  which patches the flow to become uniform and parallel at the exit and thus complete the nozzle design. The vital idea is to incorporate the requirement of a uniform nozzle exit flow at some Mach number distribution, varying monotonically from sonic flow at the nozzle throat to the exit. This allows the construction of a characteristic network, starting at the nozzle exit and marching upstream. Any streamline in this flow gives an appropriate definition of an inviscid nozzle wall and can be solved in three steps. The first step is the finding of characteristic lines. These are some particular directions (lines) in the  $xy$ -space where flow variables are continuous, but the derivatives are indeterminate. The second step is to find the compatibility equations by combining the partial differential conservation equations in such a way that ordinary differential equations obtained hold only along the characteristic lines. The third step is the solving of the compatibility equations step by step along the characteristic lines, starting from the given initial conditions at some point or region in the flow. By this procedure, the complete flow field can be mapped out along the characteristics. In general, the characteristic lines depend on the flow field and the compatibility equations are a function of geometric location along the characteristic lines. Direct design anchored in  $MOC$  stays feasible as an initialisation procedure for design-by-analysis methods (Shope, 2006).

Ideal thrust can be determined by expanding the flow isentropically in diverging portion to ambient conditions. A non-dimensional ideal thrust parameter may be obtained from Equation 2.5.



$$\frac{F_{ideal}}{p^*A^*} = mV_e + \frac{(P_e - P_a)A_e}{P^*A^*} \quad (2.5)$$

Optimum performance is obtained when  $P_e = P_a$  referred to as design expansion ratio.

Nozzle performance or  $C_{Fg}$  is defined as the ratio of actual thrust to the ideal thrust.

$C_{Fg}$  is obtained from Equation 2.6.

$$C_{Fg} = \frac{F_{actual}}{F_{ideal}} \quad (2.6)$$

Ideal thrust for a fixed area ideal contour nozzle is obtained only at design conditions

(Gamble *et al.*, 2004).

### 2.1.3 Truncated Ideal Contour Nozzle

Although Ideal Contour (*IC*) nozzle constructed by *MOC* offers high performance, it is too long (around 50 times of the throat radius) and hence heavy (Rao, 1958). The thrust contribution by the last part of the contour is negligible as it has low wall slopes. A feasible nozzle contour is obtained by truncating the contour of *IC*, called Truncated Ideal Contour (*TIC*). *TIC* nozzle can offer a length reduction with relatively small performance losses (Ostlund, 2002). A particular contour may be preferred by examining truncated portions of several uniform exit flow nozzles of different area ratios. At design condition, the contoured throat nozzle offers an equivalent thrust with a lesser nozzle pressure ratio of 4% and marginal acoustic benefit (Gustaffson *et al.*, 2012). Genin and Stark (2016) did an experimental investigation of cold flow *TIC* nozzles in which they did wall pressure, side load measurements and Schlieren images.

An extremely short nozzle called Compressed Truncated Ideal Contour (*CTIC*) is obtained by linearly compressing a *TIC* nozzle. The discontinuity in the nozzle slope due to this compression procedure is eliminated by a cubic equation which smoothly connects the linearly compressed curve with the initial circular curve. It is claimed *CTIC* nozzle has higher efficiency than Rao nozzle. However, Hoffman (1987) found that Rao nozzle is better than *CTIC* and the difference in performance is marginal. An example of *CTIC* nozzle is LE7A (Ostlund, 2002). Melnikova *et al.* (1976) suggested truncated nozzles combining two-parameter family of contours for specified expansion ratio with minimum length.

#### **2.1.4 Thrust Optimised Contour Nozzle**

A direct and graceful approach for the design of nozzle profile is the method using the calculus of variations. In this a characteristic surface was introduced and that acts as a control surface for mass flow, momentum, and the length of the nozzle. By this method, the governing equations are reduced to the ordinary differential equation from partial differential equations and a one-dimensional variation problem is obtained. It was concluded that all optimum nozzles of different length can be represented by a single contour for a given ambient pressure. Rao (1958) simplified this complex method and the nozzle developed by him was labelled as Rao nozzle in the west. The same method was developed by Shmyglevsky (Shmyglevsky, 1958) in Russia and the nozzle was known as Shmyglevsky nozzle.

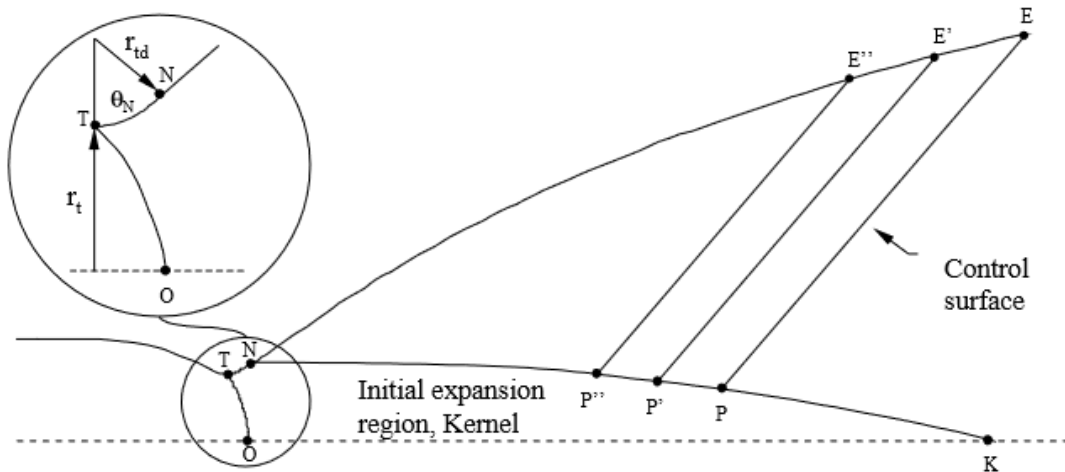


Fig. 2.3 Basic flow structures in a Thrust Optimised Contoured nozzle (Ostlund, 2002)

Figure 2.3 shows an outline of flow through a Thrust Optimised Contoured (*TOC*) nozzle. Initially, a kernel flow is generated with *MOC* for a variety of  $\theta_N$  and a given throat curvature  $r_{td}$ . For particular design parameters (such as  $M_E$  and  $\epsilon$ , or  $L$  and  $\epsilon$ ) the points  $P$  and  $N$  shall be calculated by satisfying the following two conditions simultaneously.

- i) Mass flow across  $PE$  equals the mass flow across  $NP$ .
- ii) The resulting nozzle produces maximum thrust

These conditions are formulated by using the calculus of variations. After finding  $N$  and  $P$ , the kernel line  $TNKO$  is fixed and the contour line  $NE$  is constructed by the following method. By selecting  $P', P''$ , etc. along line  $NK$ , a series of control surfaces  $P'E', P''E''$ , etc. can be created to define  $E', E''$ , etc. along the contour  $NE$ .

Here the nozzle wall has to satisfy Equation 2.7 where  $p, \rho, V, M$  and  $\theta$  denote the pressure, density, velocity, Mach number, and flow direction respectively.

$$\frac{p-p_a}{\frac{1}{2}\rho V^2} \sqrt{M^2-1} = \sin 2\theta \quad (2.7)$$

Knuth (1960) proposed that the flow condition at each point of the nozzle contour is independent of the rest of the other points in the contour for small divergence angles. Equation 2.7 was applied at each point and the nozzle contour was then created through stepwise integration. Figure 2.4 shows the length comparison between the contoured nozzle and the conical nozzle having 15° half cone angle for the same vacuum thrust coefficient.

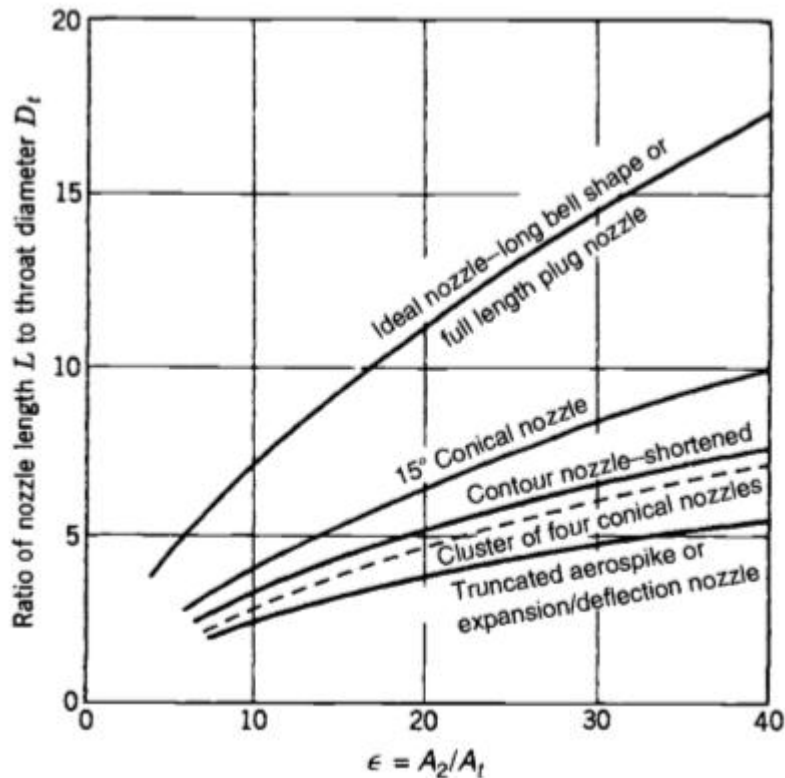


Fig. 2.4 Length comparison with different types of nozzles (Rao, 1961)

The maximum angle which will produce a smooth flow without compression waves is one-half the Prandtl-Meyer angle (Zucker and Biblarz, 2002). The expansion angle shall be smaller than the maximum possible angle for getting a more uniform flow

(Puckett, 1946). Puckett pointed out that there is radial flow at the maximum slope cross-section and need to design the contour after the inflection point only. From throat to inflection point a smooth curve can be fitted.

The nozzle flow can be divided into two parts, a subsonic and supersonic region. The subsonic region is employed for giving a sonic flow at the throat. The supersonic region is independent of the upstream conditions of the sonic line. There are two categories of Minimum Length Nozzle (*MLN*) according to the shape of the sonic line; *MLN* with a straight sonic line and *MLN* with a curved sonic line. For *MLN* with a straight sonic line, the wall at the throat produces centred and divergent expansion waves. The *MLN* with a straight sonic line is analysed in (Anderson, 1982, 1988) and Argrow and Emanuel (1988). Dumitrescu (1975) reported the analysis of axisymmetric *MLN* with the straight sonic line. The flow inside nozzle does not have the presence of centred Mach line for *MLN* with curved sonic line. Emanuel (1986) and Dumitrescu (1975) analysed the flow characteristics of axisymmetric *MLN* with a curved sonic line.

Figure 2.5 shows the flow inside the axisymmetric *MLN* with straight sonic line. For the 2D as well as axisymmetric case the area *OAB*, which is called the Kernel region, is a non-simple wave region. In the case of 2D flow, the area of transition (*ABE*) is a simple region and the solution can be analytically found (Anderson 1988). However, in axisymmetric case, area *ABE* is of a non-simple region and a numerical solution is necessary (Oosthuisen and Carscallen, 1997).

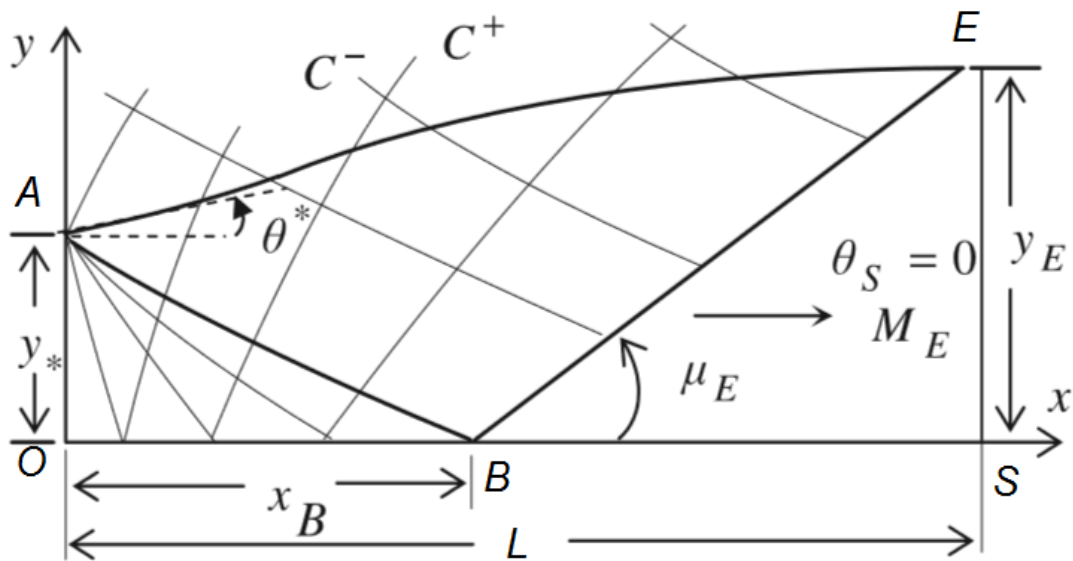


Fig. 2.5 Flow inside the axisymmetric Minimum Length Nozzle (Zebbiche, 2011)

The area  $BSE$  is a uniform flow region in which the Mach number is the same as that at the nozzle exit. Rao (1958) used  $MLN2D$  with a straight sonic line for their experiments assuming that the specific heat of the gas is independent of temperature. As the assumption is realistic only for low stagnation temperatures (up to 1000K). Raltson and Rabinowitz (1985) made a polynomial interpolation to these values in an analytical form. Zebbiche and Youbi (2006) and Zebbiche (2006, 2007) used a 9<sup>th</sup> degree polynomial for this application. In an axisymmetric nozzle, the expansion is faster than that of a  $2D$  nozzle. The axisymmetric nozzle is short as compared to the  $2D$  nozzle for the same Mach number and nearly equal to the square root of the length of the  $2D$  nozzle (Zebbiche, 2011).

A *TOC* nozzle offers the highest performance for a certain length and expansion ratio. In a *TOC* the curve at the throat turns more sharply which corresponds to a higher initial expansion and wall angle that turns the flow more quickly (Ostlund, 2002). Yen and Martindale (2008) employed inviscid supersonic nozzle design approach for obtaining an ideal uniform test section flow in wind tunnel applications. In the rhombus region, the accelerating Mach number turned constant and the following compression waves became absolutely linear. The wave cancellation in the divergent section of the nozzle was not executed in their design. Jegede and Crowther (2016) developed a new method in the design of non-axisymmetric *3D* nozzle geometries by applying the *2D* method of characteristics and later carried out experimental and numerical analysis. The accuracy of their predictions improved significantly by considering viscous effects and boundary layer corrections.

Sternin (2000) designed a contour by conjugating circular arcs which have higher thrust characteristics to those of extremal nozzles by 0.7 - 1%. Allman and Hoffman (1981) assumed maximum thrust contour as a second degree polynomial having a fixed initial expansion contour. The three coefficients of the polynomial were varied by direct optimisation methods for finding the maximum thrust contour. Schomberg *et al.* (2015) avoided the flow separation under initial operating conditions by designing the expansion curve by two arc methods for supersonic nozzles.

The calculation for the design of Rao-Shmyglevsky nozzle was complicated and hence Rao proposed a skewed parabolic geometric approximation from the inflection point to the nozzle exit (Rao, 1960). A Thrust Optimised Parabolic (*TOP*) nozzle was constructed by using three curves as shown in Figure 2.6. Converging section was made by using a large circle of radius  $1.5R_t$ , a small circle of radius  $0.382R_t$ , and a parabola to extend the approximated bell contour to the nozzle exit plane (Kulhanek, 2012).

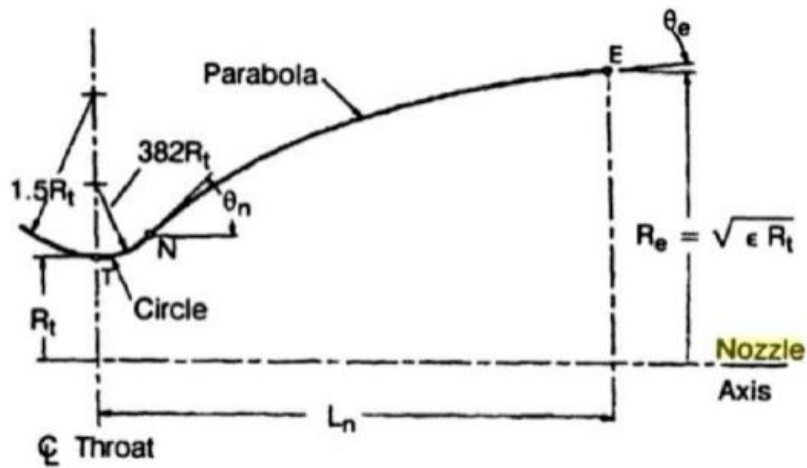


Fig. 2.6 *TOP* nozzle based on Rao's approximation (Kulhanek, 2012)

In the figure,  $L_n$  is the length of the nozzle and is determined by the Equation 2.8.

$$L_n = \frac{K(\sqrt{\epsilon}-1)R_t}{\tan \theta_e} \quad (2.8)$$

where  $K$  is the value chosen based on the percentage of the length of a conical nozzle with  $15^\circ$  half cone angle,  $\epsilon$  is the expansion ratio,  $\theta_e$  is the nozzle exit angle and  $R_t$  is the throat radius. The expansion ratio  $\epsilon$  can be calculated by the Equation 2.9

$$\epsilon = \frac{A_e}{A_t} = \frac{1}{M_e} \sqrt{\left[ \frac{2}{\gamma+1} \left( 1 + \frac{\gamma-1}{2} M_e^2 \right) \right]^{\frac{\gamma+1}{\gamma-1}}} \quad (2.9)$$



The optimal wall angles for a wide range of length ratios and expansion ratios are shown in Figure 2.7. In the figure  $\varepsilon$  is the expansion ratio  $KL$  is the length ratio  $\theta_i$  and  $\theta_e$  are initial wall angles respectively. Meerbeeck (2013) obtained a performance increase of 0.5% by nozzle contour optimisation.

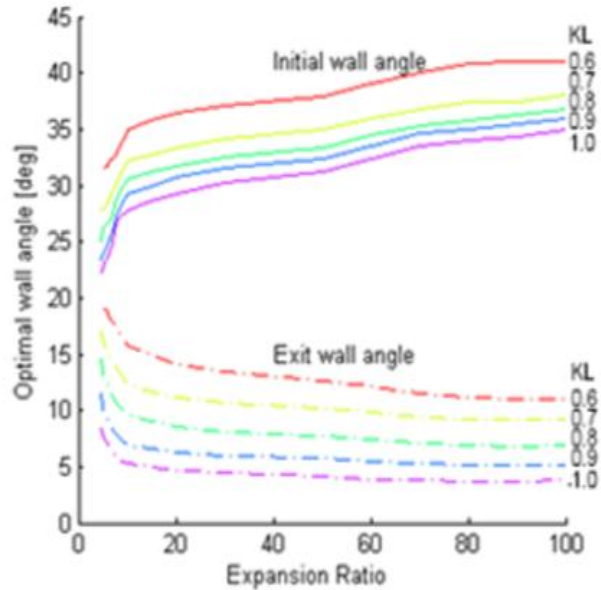


Fig. 2.7 Variation of  $\theta_i$  and  $\theta_e$  with  $\varepsilon$  and  $KL$  (Meerbeeck, 2013)

A geometric discontinuity occurs at the point where the throat meets the parabolic arc which produces internal shocks that increase the wall pressure at the exit. However, it is helpful in avoiding destructive side loads in the case of highly overexpanded cases (Ostlund, 2002). *TOC* nozzles are mainly used in rocket propulsion whereas *TOP* nozzles are commonly used in the Space Shuttle Main Engines which experiences Free Shock Separation (*FSS*) and Restricted Shock Separation (*RSS*) during their use (Hagemann and Frey, 2008). Table 2.2 shows the comparison of key features for the types of nozzle contours.

Table 2.2: Comparison of nozzle contour type

Nozzle name	Key Features
Conical	Straight wall from throat up to the nozzle exit Incomplete flow turning Simple in construction
Ideal Contour <i>IC</i>	Transition of curved walls near throat to almost straight walls near the nozzle exit Method of Characteristics is used Virtually complete flow turning The nozzle is too long
Truncated Ideal Contour <i>TIC</i>	Transition of curved walls near throat to nearly straight walls near the nozzle exit A shortened version of <i>MOC</i> Virtually complete flow turning Nozzle length is lesser than <i>IC</i>
Thrust Optimised Contour <i>TOC</i>	Transition of curved walls near throat to nearly straight walls near the nozzle exit More sudden transition than <i>TIC</i> Virtually complete flow turning

### 2.1.5 Losses in Nozzle

The four categories of nozzle losses for vacuum-optimised nozzles are kinetic losses, friction losses, two-dimensional losses, and shock losses. When the combustion is incomplete in the combustion chamber, the flue gas from the combustion chamber enters to the nozzle and reaction will continue in the nozzle. Due to the rapid decrease in pressure and temperature, chemical equilibrium gets altered and this leads to the kinetic losses. The main cause of frictional losses is the viscous effects in the boundary layer. For a non-ideal contoured nozzle, due to the two-dimensional expansion, an inhomogeneous exit flow field is created. At the nozzle exit, the flow is not aligned with the nozzle axis resulting in kinetic energy loss and therefore a loss in

axial thrust. These losses are called two-dimensional losses. The shock losses are due to the internal shock formation near the throat region. The shock losses and two-dimensional losses are together called divergence losses as these two losses depend purely on the expansion process and are difficult to calculate separately. An additional performance loss will occur in the case of altitude optimised nozzle and it is due to the integral force exerted by the ambient pressure on the nozzle wall. This loss is a minimum when the nozzle exit pressure is the same as ambient pressure (Meerbeek *et al.* 2013). Manski and Hagemann (1996) examined the effect of mixture ratio and combustion chamber pressure on the nozzle losses. Miyajima *et al.* (1983) examined the influence of mixture ratio on nozzle losses for engines using H<sub>2</sub> and O<sub>2</sub>. The works mentioned above are mainly focussed on vacuum optimisation of rocket nozzles. Sternin (2003) found that in the case of de Laval nozzle, at large expansion ratios, the viscous loss is almost independent of the exit cross-section parameter and is found only by the parameter values on the nozzle contour.

### **2.1.6 Supersonic Jet Flow**

Figure 2.8 shows the flow over the initial length of a supersonic jet at underexpanded condition. Here,  $r_1$  is the radial distance from the nozzle axis to the location of the inner boundary and  $r_3$  is the distance from the nozzle axis to the centreline of the inner boundary and outer mixing layer. Regions I and II symbolise the outer and inner boundaries of the mixing layer respectively. Region III symbolises the centreline of the mixing layer and  $\delta$  denotes shear layer thickness.

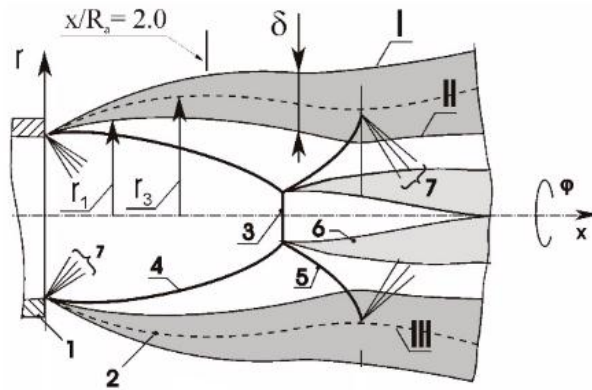


Fig. 2.8 Flow over the initial length of a supersonic jet (Zapryagaev *et al.*, 2018)

In the Fig. 2.8, 1 is the nozzle, 2 is the mixing layer, 3 is the Mach disc, 4 and 5 are the barrel and reflected shocks, 6 is the inner shear layer formed behind the point of interaction of compression shocks 3, 4 & 5, and 7 is the expansion fan.

### 2.1.7 Shock Cell Parameters

At underexpanded condition, a wedge shaped expansion waves occur at the nozzle exit. These waves cross each other and get reflected back from jet boundaries as compression waves. Due to these compression and expansion waves a periodic diamond pattern named shock cell structure is formed as shown in Figure 2.9.

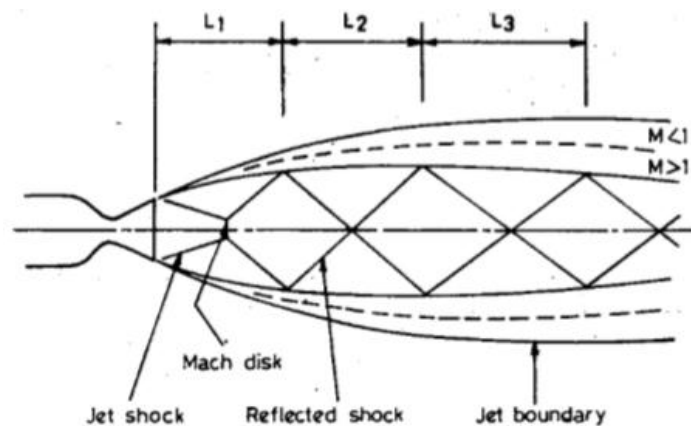


Fig. 2.9 Structure of shock cells (Mehta and Prasad, 1996)

In Fig. 2.9  $L_1$  is the first shock cell length, which is the length of the first diamond pattern from nozzle exit. The angle which the shock wave makes with the initial direction of flow is called shock wave angle. The potential core length is defined as the axial distance up to which the shock wave succeeds or the distance from the nozzle exit to a point farthest downstream where the flow Mach number becomes unity.

## 2.2 EXPERIMENTAL WORKS

Static and stagnation pressure probes are standard instrumentation in most of the flow measuring systems. The flow structure of underexpanded jet was investigated experimentally through static pressure measurements (Norum and Seiner 1982; Norum and Shearin 1988; Andre *et al.* 2014a). Katanoda *et al.* (2000) analysed Mach disks with Pitot pressure measurements and compared the data with that of computational predictions. Direct measurement of thrust in jet flow is a tedious effort because of measurement difficulties. The total thrust can be calculated by using the Equation 2.4 by measuring pressure and velocity at the nozzle exit plane. Cuppoletti *et al.* (2014) calculated thrust at  $x/D_j = 0.05$  by using pressure and velocity profiles. The velocity profiles from *PIV* (Particle Image Velocimetry) measurements were used to calculate the upstream Mach number by using isentropic expansion relation with the assumption of constant temperature at the nozzle exit. However, the assumption of constant temperature is the main source of error in the calculations (Hiers *et al.* 2004).

At lower altitudes, the nozzle exit pressure is less than the ambient pressure and nozzle flow adjusts to the ambient by oblique shock waves. Oblique shocks may be formed inside the nozzle divergent portion itself if the nozzle wall pressure is much lesser than atmospheric pressure. Due to this phenomenon, flow separation may occur and the boundary layer is unable to withstand this pressure rise. Once this separation occurs, the

pressure further increases along the nozzle wall to settle as atmospheric pressure. Structural failures in rocket engines may occur because of the addition of large aerodynamic side loads due to the flow separation (Allamaprabhu, 2016). From the experiment results of Hunter (1998) at the overexpanded condition, shock induced boundary layer separation divides the flow into two flow regimes such as (i) three-dimensional separation with fractional reattachment and (ii) two-dimensional separation with full detachment. Love *et al.* (1959) made theoretical and experimental studies on the axisymmetric jets exhausting from supersonic nozzles to still air. Their work focused on the effects of nozzle exit Mach number and divergence on jet static pressure ratio, shock cell length and the curvature of the jet boundary. Numerical and experimental studies have been carried out for enhancing insight into the effects of side load and flow separation inside the nozzles (Terhardt M. *et al.*, 1999; Frey and Hagemann, 2000). Earlier studies (Andreopoulou *et al.*, 1988; Verma and Koppenwallner, 2002) reported that boundary layer shock wave interaction causes the generation of severe fluctuations and the separation shocks exhibit a streamwise oscillatory motion. Frey *et al.* (2000), Hagemann *et al.* (2002), Reijasse *et al.* (2001), Verma and Haidn (2009), etc. studied the effects of free shock and restricted shock separations by experiments. In the case of *FSS*, a back-flow region downstream of the separation location occurs due to the entrainment of ambient air. Ramsey *et al.* (2012) observed cap shock pattern in *TOC* nozzle at overexpanded conditions. This pattern is related to *RSS* and it results in side loads. Hydroxyl tagging velocimetry has been used to measure the instantaneous planar *2D* velocity field.

In the case of underexpanded flows, the jet from the axisymmetric nozzle expands to the atmospheric pressure at the jet boundary by expansion fans at the nozzle lip. The constant pressure condition along the jet boundary causes this boundary to bend back towards the flow axis. The compression waves do not meet at a single point on the free

surface and will cross each other ahead of this point forming weak shocks as shown in Figure 2.10 (a). By increasing the pressure ratio, the compression waves will cross further upstream and can result in coalescing of shocks, as illustrated in Figure 2.10 (b). When the pressure ratio increases further, these grabbing shocks do not congregate the axis but are attached with a normal shock or Mach disc, as shown in Figure 2.10 (c).

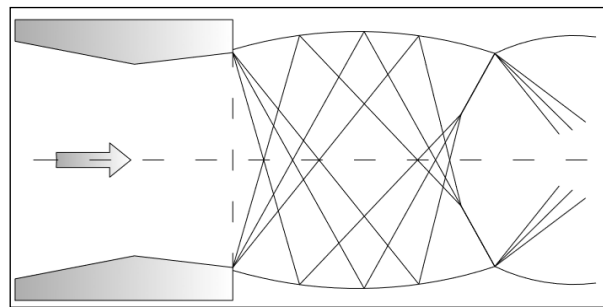


Fig. 2.10 (a) Formation of weak shocks

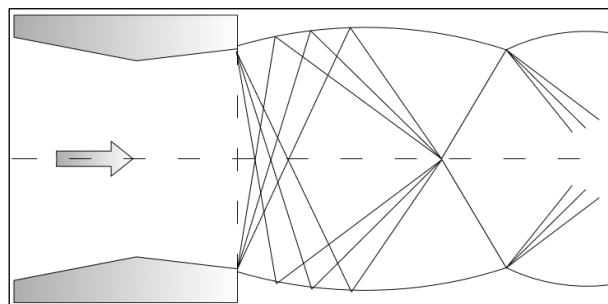


Fig. 2.10 (b) Formation of coalescing shocks

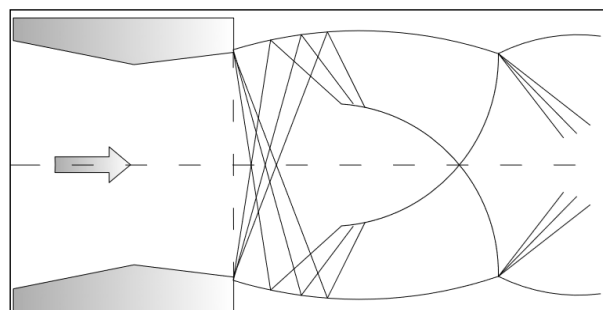


Fig. 2.10 (c) Formation of reflecting shocks

The shock structure is prolonged until the viscous effects become predominant. Panda and Seasholtz (1999) obtained the density field of underexpanded jet issuing from a supersonic nozzle using Rayleigh scattering-based technique and related this to the screeching phenomenon. The shock cell structure of underexpanded supersonic nozzles was studied by Andre *et al.* (2014a) using Pitot probe and Schlieren visualisation. Beyeh (2009) made an analysis of Mach disks from an underexpanded nozzle using experimental and computational methods. A spontaneous Rotational-Vibrational Raman scattering spectrometer for measuring pressure and temperature and Schlieren system for locating the position of Mach disks were used. A Schlieren system with three types of knife edges viz. circular cut off, a horizontal knife edge and a vertical knife edge were used. It was observed that a horizontal knife edge detected the vertical gradient of density whereas a vertical knife edge detected the horizontal gradient.

Mach disks are the high-pressure regions in the exhaust flow at high underexpanded conditions. Kuehner *et al.* (2002) have carried out experiments on Mach disks by using Coherent Anti-Stokes Raman Spectroscopy (CARS). In the case of a supersonic nozzle, the flow accelerates from the throat of the nozzle and pressure decreases. A nozzle is said to be at underexpanded condition if the nozzle exit pressure is higher than the surroundings. The jet from the nozzle tends to achieve atmospheric pressure through an expansion fan and these waves reflect back from the free jet boundary as compression waves. These compression waves join together and consequently oblique shock waves are formed. These oblique shock waves then seemingly reflect off from the flow centre line and this produces a shock triple point. Jeronimo *et al.* (2002) examined the Mach disk formed in the first shock cell of an overexpanded jet and analysed the shock cell parameters.



Baek *et al.* (2006) conducted experiments to find the effects of relative humidity on underexpanded supersonic jet structure, such as Mach disk location, Mach disk diameter, jet boundary location, barrel shock wave, etc. It was observed that relative humidity had certain influence on Mach disk location and Mach disk diameter. At moist condition, Mach disk was located farther upstream and Mach disk diameter was smaller than that of dry air condition. The jet boundary configuration and barrel shock wave were not much influenced by humidity. Zhu and Jiang (2014) used the Schlieren imaging for analysing the flow structure. The light generated by the tungsten halogen lamp was passed through a lens which was being cut by a slit. Then it is allowed to get reflected by a parabolic mirror of 200 mm diameter to produce a collimated light beam. This parallel beam is reflected by a plane mirror and then passed through the test section and again focused by another parabolic mirror to a single-lens reflex camera for taking images.

Robert Hooke developed the Schlieren imaging technique which is an optical technique for studying homogenous media and Leon Foucault introduced the knife edge cut off technique to capture images (Mitra *et al.*, 1981). August Toepler is the first person who visualised the movement of shock waves by using Schlieren images (Meier, 2002). Schlieren technique gives an instructive, non-intrusive method for the study of transparent and optical media. This technique is very useful in fluid dynamics as they are very sensitive and do not obstruct the flow (Richard and Raffel, 2001). By Schlieren imaging one can visualise density gradients in flows by using the property that light travels non-uniformly through density-inhomogeneous media. Equation 2.10 shows the relation between refractive index and density of gases.

$$n-1 = k\rho \quad (2.10)$$

where  $n$  is the refractive index,  $\rho$  is the density and  $k$  is the Gladstone-Dale coefficient for gases. However, the refractive index changes with density and light ray get turned away from its original direction based on the density gradient of the media. Even if the deflections are small, one can focus it by using the lens (Settles, 2006). In cold flow testing of dual bell nozzle, Schlieren images were used to study the transition behaviour between two nozzle contours (Genin and Stark, 2010). Stark *et al.* (2006) used Schlieren imaging for determining transition duration and angle of tilt of the Mach disk in a dual bell nozzle. Andre *et al.* (2014b) experimentally investigated an underexpanded supersonic jet, with a design Mach number of 1.5, from a *CD* nozzle by using a conventional Z-type Schlieren system. It consists of a *QTH* (Quartz Tungsten Halogen) light source, two parabolic mirrors with 203.2 mm diameter and focal ratio  $f/8$  and a high-speed *CMOS* camera. A razor blade has been set perpendicular to the flow direction for filtering purpose. Panda (1999) visualised the flow field by Schlieren imaging with two spherical mirrors having a diameter of 152 mm and a focal length of 194 mm. The horizontal density gradient becomes visible by keeping the knife edge in a vertical position. The images were taken by using a Nikon F4 camera. The experiments were carried out in a dark room by keeping the camera shutter in an open position.

Shadowgraph imaging is almost similar to Schlieren imaging and works with the same basic principle of refraction through inhomogeneous media. There is no need for employing knife edge cut-off in shadowgraph and is easy to use. Shadowgraphs are normally not much sensitive to smaller density gradient and it can be used for

visualising shock waves and high turbulent flows (Settles, 2006). According to Kaushik and Hanmaiahgari (2015), the reduction in jet core length is sturdily controlled by the levels of expansion at the nozzle exit. The shadowgraph images were used for finding the efficacy of jet in mixing augmentation and weakening the shock-cell structures, which is beneficial from the acoustics point of view.

Verma and Ciezki (2003) conducted an experimental investigation on *TOP* nozzle to observe the unsteady nature of flow phenomenon at different nozzle pressure ratios. The study was carried out by using wall pressure measurements both in axial and radial directions, surface oil visualisation technique and colour Schlieren images. The results show that the asymmetric flow condition during the transition to be extremely unstable with the separation front oscillating in a wavy pattern. Researchers such as Panda (1999), Beyeh (2009), Suzuki *et al.* (2013), etc. took Schlieren images of underexpanded supersonic jets with different positions of knife edges. The underexpanded jet is not uniform due to the presence of expansion waves, compression waves and shock waves corresponding to white and dark regions obtained in the Schlieren image. The deformation of white and dark regions becomes stronger as one move further away from the exit of the nozzle. Hence the jet becomes unsteady and oscillates laterally or helically. Panda (1998) and Suzuki *et al.* (2013) explained the oscillatory motion of the shocks formed when the nozzles were operated at the underexpanded conditions. This phenomenon is due to the large, ordered turbulent structures through the jet shear layer in the flow field.

Munday *et al.* (2009) investigated the flow structures from a conical *CD* nozzle by using *PIV* and also captured images by shadowgraph technique. They observed two sets of shock diamonds, one shed from the nozzle lip and other attached at the throat of the nozzle, generating a double diamond in the flow. Andre *et al.* (2014a) carried out experiments using *PIV*, focusing on shock cell structure, mixing layer thickness and turbulence levels. The strength of the shock cell structure was analysed based on the profiles of mean velocity. The velocity gradient diminishes towards the mixing layer in the downstream direction inside the jet plume. In the case of slightly underexpanded jets, the turbulence level is almost constant along the downstream direction, whereas for highly underexpanded jets the turbulent fluctuations are very high. Gustafsson *et al.* (2012) conducted experimental investigations on supersonic conical *CD* nozzles with sharp throat and splined profile. They used *PIV* for measuring flow properties. The uncertainty of *PIV* depends on flow conditions and measurement parameters such as equipment calibration, sampling, particle dynamics and image processing. Wilson and Smith (2013) presented a systematic evaluation of the uncertainty of a rectangular laminar jet by comparing hot wire and *PIV* data. It was proved that the velocity gradient and particle displacement are the main sources of uncertainty.

The uncertainty estimates reported by previous researchers are also taken into consideration while setting procedures for measurements. Rao *et al.* (2016) have reported an uncertainty of  $\pm 4\%$  in the measurement of stagnation pressure including accuracy of sensor ( $\pm 1\%$ ) and operation of mechanical elements. Tropea *et al.* (2007) have conducted invasive pitot pressure measurements and used a finite area tube which introduce errors besides the accuracy of the sensor ( $\pm 1\%$ ) such as anticipated variation across the pitot area ( $\pm 3\%$ ) and effect of viscosity ( $\pm 2\%$ ).

## 2.3 NUMERICAL SIMULATIONS

The numerical solution of supersonic flows emanating from nozzles is a challenging problem in fluid dynamics applications. The flow field characteristics of *CD* nozzles are anchored based on Reynolds Averaged Navier Stokes calculations and the execution of an appropriate turbulence model for the closure of the equations. A number of turbulence models can be applied to the numerical study ranging from algebraic to linear and nonlinear turbulence models. An algebraic model is enough for analysing simple viscous flow. However, two equation models with second-order closure give better results for determining complex viscous flow features with limited computational resources. Hamed and Vogiatzist (1997) carried out *2D* simulations with five different turbulence models for predicting centreline pressure distribution of overexpanded nozzle flows. The turbulence models such as the algebraic model of Baldwin-Lomax, *RNG*, one equation model of Baldwin-Barth and the two equation  $k-\epsilon$  and  $k-\omega$  models of Chien and Wilcox were employed. It was observed that the shock position and pressure variation were stoutly affected by the selection of turbulence models. Hamed and Vogiatzist (1998) used the two equation  $k-\omega$  turbulence model for predicting the surface pressure distribution and internal thrust coefficient of a two dimensional *CD* nozzle.

Chen *et al.* (1994), Frey and Hagemann (1998), Gross and Weiland (2004), Morinigo and Salva (2008), Nasuti *et al.* (2007), Nasuti and Onofri (2009), etc. carried out numerical works on overexpanded nozzle flow with separation. The asymmetry in flow separation causes heavy aerodynamic side loads which leads to structural failure of rocket engines. Allamaprabhu *et al.* (2016) predicted the flow separation occurring

in the overexpanded mode. There is under-prediction at low nozzle pressure ratios (*NPRs*) in the conical nozzle, whereas it occurs at high *NPRs* in the case of two contoured nozzle. The impact of jet spreading on pressure recovery is not remarkable at low nozzle wall angles and the flow separation location is habitually under-predicted at small nozzle wall angles. In the case of *TOP* nozzle, the *SST* (Shear Stress Transport) *k- $\omega$*  model gave better results than that of Wilcox *k- $\omega$*  model. However, an over-prediction for the separation location at *NPR*=12 was observed (Ostlund, 1999). For *TOC* nozzle an over-prediction for *NPR*<23.9 was also reported (Nebbache and Pilinski, 2006). The same trends of over-prediction were also observed for *TIC* nozzles (Pilinski and Nebbache, 2004). Yonezawa *et al.* (2007) reported that there is no significant difference in the performance of *SA* and *SST* models in the simulation of *CTP* (Compressed Truncated Perfect) nozzles.

Otobe *et al.* (2008) studied the influence of nozzle geometry on the near-field flow structures of highly underexpanded jets. It was clear from the *CFD* (Computational Fluid Dynamics) analysis, that the jet pressure ratio has an influence on the jet boundary shape and also the distance between the nozzle exit and Mach disk. A correlation of Mach disk diameter with the jet pressure ratio was also developed. However, it was observed that the nozzle geometries had less influence on the near-field flow structure. There are no specific universal guidelines for the simulation of nozzle flows in various modes of expansion. However, Mern and Agarwal (2013) have established best practice guidelines for specific problems related to high-speed jet flows. The flow structures of highly underexpanded jets from different nozzle geometries were carried out by Li *et al.* (2017). Large Eddy Simulations (*LES*) were employed for analysing the flow characteristics of jets from circular, elliptic, square,

and rectangular nozzles. It was observed that both square and the circular jets correspond to a  $3D$  helical instability mode, while the other two nozzle jets have a  $2D$  flapping instability. Among these nozzles, flow from elliptical configuration seems to have slow penetration with a larger overall mixing area. Mousavi and Roohi (2014) numerically investigated the shock train in a  $CD$  nozzle by using  $RSM$  (Reynolds stress model) and compared the predictions with experimental results of Weiss *et al.* (2010). The location of the first shock cell was accurately predicted in their work.

The prediction of jet noise requires vast information on the mean flow and turbulent characteristics of jets emanating from nozzles. Tide and Babu (2009) accurately predicted mean and fluctuating quantities for round jets with  $RANS$  (Reynolds-averaged Navier-Stokes) calculations with moderately less computational resources. Balabel *et al.* (2011) have carried out  $2D$  numerical simulations of the experimental work conducted by Hunter (1998) and reported that the shear stress transport  $k-\omega$  model showed the best agreement with the experimental data.

Venkatapathy and Feiereisen (1988) predicted the various flow properties like density, temperature and velocity distributions by  $CFD$  simulations. Taha *et al.* (2001) and Allamaprabhu *et al.* (2011) have used the Fluent  $CFD$  code for predicting the flow through nozzles. Comparative studies on supersonic jets from nozzles with complex geometries by centreline Pitot pressure measurements and  $3DRANS$  simulations were reported by Rao *et al.* (2016). Emami *et al.* (2009) made an analytical approach to an inviscid imperfectly expanded axisymmetric supersonic jet and the results were in reasonable agreement with the experimental data of Seiner and Norum (1980). Spotts *et al.* (2013) conducted a  $CFD$  analysis on conical nozzles of

15<sup>0</sup>, 25<sup>0</sup>, and 40<sup>0</sup> half cone angle. They found that the discharge coefficient inversely proportional to the nozzle angle and the nozzle pressure ratio at choked condition is lower for a smaller nozzle angle. The discharge coefficient is directly proportional to the nozzle pressure ratio until the choked condition is achieved. The thrust coefficient is directly proportional to the nozzle angle and inversely proportional to the nozzle pressure ratio.

It is clear from the above discussions that the profile of *CD* nozzle plays a crucial role in the development of shock cell structures and the performance of nozzles. Hence the present work focuses on capturing the flow characteristics of jets, variation in shock cell structures and enhancement in performance parameters by pressure measurements, flow visualizations and numerical calculations so as to attain a quantitative measure of the jet flow dynamics.

## **2.4 MOTIVATION**

From the above literature survey, it is observed that the design of the supersonic nozzle is a challenging task as both economic and environmental aspects have to be taken into account meticulously. Moreover, nozzle profile plays a crucial role in enhancing thrust and the quantum of work carried out in this area, especially experimental investigations are significantly less. Hence the design and development of the nozzle profile and geometry have to be given primary focus followed by the evaluation of the performance characteristics for these concepts, both experimentally and numerically.



The commonly used nozzle contours reported in the literature are Conical, Ideal Contoured nozzle, Truncated Ideal Contoured nozzle, Thrust Optimised Contoured nozzle, Thrust Optimised Parabolic nozzle, etc. and are seen to be associated with kinetic, frictional, and shock losses. It is observed that an inhomogeneous exit flow field is formed for a non-ideal contoured nozzle and the flow is not aligned with the nozzle axis at the exit which results in loss of axial thrust. The shock losses are primarily due to the internal shock formation near the throat region and depend purely on expansion processes which are difficult to calculate. The nozzle thrust can be improved tremendously by reducing these divergence losses. Hence nozzle thrust optimisation has enormous practical importance, as a minute fraction of thrust from a jet nozzle can result in a momentous gain in the payload, which gave motivation for this research. This has led to the main objective of research to develop a nozzle for enhancing thrust in propulsive devices operating on supersonic jets.

Thrust optimisation is an art in which it has to meet the thrust requirements with minimum length and certain nozzle configurations already developed by the researchers satisfy this criterion. However, even in these nozzles, internal shocks are formed at the inflection point enhancing thrust losses. The thrust can be significantly improved by eliminating the formation of internal shocks. This inadequacy in design gave the motivation to develop a new concept of double parabolic profile on *CD* nozzle configuration with minimum internal shock formation in the divergent section and also to generate axial flow at the exit.

Theoretically, the maximum angle which will produce a smooth flow without any shocks is reported to be one half of the Prandtl-Meyer angle. However, for getting a more uniform flow it is observed that the expansion angle must be smaller than this maximum possible angle. Hence the concept of varying slopes in parabolic profiles based on Prandtl-Meyer expansion angles and its effect on shock cell and performance parameters has to be investigated meticulously.

Mostly, nozzles are designed at sea level conditions to avoid overexpansion at the exit as it induces side loads. Hence the study of jet flow at under-expanded conditions has much practical relevance and applications. This leads to the motivation for investigation of flow parameters at underexpanded conditions for various nozzle pressure ratios. Experimental works related to supersonic nozzle flows are found to be scarce in literature due to the enormous expenditure incurred in experimental set-up and instrumentation. Hence thorough experimental investigations are required for capturing flow characteristics and conducting performance analysis on conical, bell and double parabolic nozzles using a precise supersonic free jet facility. Also, direct measurement of thrust in a jet flow is a tedious job because of measurement difficulties without intruding the flow. It is felt that flow structure obtained by using static and stagnation pressure probes together with Schlieren images may provide better insight into the performance characteristics of the nozzles.

It is clear from the numerical works discussed in the previous section that large-scale structures in the flow field are generally more energetic whereas the small scales are weaker and have a universal character. *LES* appears to be a better methodology for a wide class of flows, where the large-scales are simulated with the aid of a grid with

appropriate resolution and the effect of the small scales are modelled. Although the predictions are quite accurate, a model has to be selected for quick evaluation which is computationally less expensive. Due to this constraint, the nozzle geometries were simulated using *RANS* with suitable turbulence model to avoid the additional computational burden. Among the different turbulence model used, *SST  $k-\omega$*  model was reported to provide better predictions, especially for supersonic nozzle flows. The investigations will be complete only when the predictions of performance and flow characteristics obtained from the *CFD* codes are validated with the experimental data measured for the different nozzle geometries under consideration.

The main objectives of the work derived from motivation after conducting literature survey can be summarized as follows:

1. To enhance thrust in propulsive devices working on high-speed jets.
2. To design and fabricate conventional conical and bell nozzles for achieving a Mach number of 1.5 at design condition.
3. To develop a new concept of double parabolic profile on *CD* nozzle configuration to generate nearly axial flow at the exit.
4. To extend the concept of varying slopes in parabolic profiles based on Prandtl-Meyer (*PM*) expansion angle.
5. To conduct experimental studies on conical, bell, and double parabolic nozzles using a supersonic free jet facility.

6. To perform numerical simulations on conical, bell, and double parabolic nozzles using *RANS* calculations enabling appropriate turbulence model.
7. To evaluate the thrust developed and analyse the shock cell structures in the issuing jet at various expansion modes.
8. To determine different flow parameters such as shock cell length, shock cell count, shock wave angle, potential core length, supersonic core length etc. at different nozzle pressure ratios (*NPRs*) both experimentally and numerically.
9. To compare the performance parameters such as thrust, thrust coefficient, discharge coefficient, variation in pressure and Mach number of conical and bell nozzles with that of the newly designed double parabolic nozzle with varying slopes (*PM/3*, *PM/4*, and *PM/5*) in the divergent portion.

## **2.5 SCOPE OF PRESENT WORK**

The scope of the research work in a wider perspective is abridged as follows:

1. To enhance thrust in propulsive devices by developing a new concept of double parabolic profile on convergent-divergent nozzle configuration so as to generate nearly axial flow at exit based on Prandtl-Meyer expansion angle.
2. To conduct experimental studies on conical, bell, and double parabolic nozzles (for three different expansion angles) using a precise supersonic free jet facility and determine the shock cell parameters and performance parameters at different nozzle pressure ratios.

3. To perform numerical simulations on conical, bell, and double parabolic nozzles using computationally less expensive *RANS* calculations for quick evaluation of performance and flow characteristics of jets emanating from different nozzle configurations and also to validate the *CFD* code with the measured experimental data.

## **CHAPTER - 3**

### **NOZZLE DESIGN AND MANUFACTURING**

Rocket nozzles are used to expand the combustion products from the combustion chamber to high velocities by converting potential and internal energy to kinetic energy. The nozzle design becomes successful, only when it produces the required thrust with minimum weight.

#### **3.1 NOZZLE DESIGN**

Basic laws used for nozzle design are law of conservation of mass, momentum, energy and equation of state. The main assumptions used for nozzle design are

1. Working fluid is homogenous and in gaseous state as the chemical equilibrium is attained in the combustion chamber itself.
2. Working fluid obeys perfect gas laws.
3. The flow through the nozzle is adiabatic as heat transfer through the nozzle wall is neglected.
4. Friction and boundary layer effects are neglected as interior of the nozzle is very smooth.
5. There are no shock waves or discontinuities inside the smooth profile of nozzle.

6. The nozzle flow and expansion are steady as transients such as start-up and tail-off are neglected.
7. The flow is assumed to be quasi-one-dimensional. The gas velocity, pressure, temperature and density are considered to be uniform at any cross section of the nozzle normal to the axis as the variation of cross section area is very smooth.

The supersonic flow for aerospace applications can be created by using a Convergent Divergent (*CD*) nozzle alone. The design of the convergent portion of a *CD* nozzle is simple and easy as it encounters a favourable pressure gradient. However, the profile of the divergent portion of a *CD* nozzle is complicated as it influences the flow characteristics and thrust. The different profiles developed in this investigation are double parabolic (*PM/3*, *PM/4*, and *PM/5*), bell, and conical. The length of *PM/3*, bell, and conical nozzles was kept the same for the sake of comparison.

### **3.1.1 Double Parabolic Nozzle**

The double parabolic nozzle is a *CD* nozzle in which the divergent portion is a combination of two parabolas; one starting from the throat and the other ending at the nozzle exit and the intersection point of the two parabolas is a function of the Prandtl-Meyer (*PM*) angle. The Prandtl-Meyer angle is the maximum angle through which a sonic flow can be turned isentropically around a convex corner. Figure 3.1 shows the profiles of double parabolic, bell, and conical nozzle where *ABC* is the diverging portion of the double parabolic nozzle. *AL* is the nozzle throat radius, *CM* is the nozzle exit radius and *LM* is the length of the divergent portion.

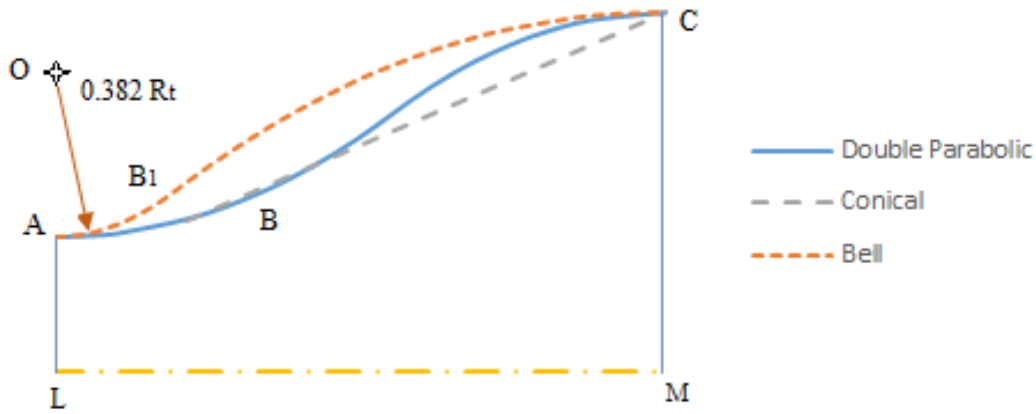


Fig. 3.1 Contours of different nozzle configurations

### 3.1.1.1 Double Parabolic $PM/3$ Nozzle

In Figure 3.1,  $ABC$  is the double parabolic profile.  $AB$  and  $BC$  are two different parabolas incorporating Equation (3.1) for the nozzle profile.

$$y = Px + Q + (Sx + T)^{0.5} \quad (3.1)$$

where  $P$ ,  $Q$ ,  $S$ , and  $T$  are constants.

The slope of the parabola  $\frac{dy}{dx} = \tan \theta$

$$\tan \theta = P + 0.5S(Sx + T)^{-0.5} \quad (3.2)$$

Four equations are obtained by applying initial and final coordinates and corresponding slopes. The initial slope of parabola  $AB$  is zero and the final slope is taken as one-third of Prandtl-Meyer angle. The Mach number at  $B$  is found from Equation 3.3.

$$\omega(M) = \sqrt{\frac{\gamma+1}{\gamma-1}} \tan^{-1} \sqrt{\frac{\gamma-1}{\gamma+1}(M^2-1)} - \tan^{-1} \sqrt{M^2-1} \quad (3.3)$$

Here  $\omega(M)$  is the one-third of Prandtl-Meyer angle for design Mach number ( $M=1.5$ ).



The area ratio is calculated from Equation 3.4.

$$\frac{A}{A^*} = \frac{1}{M} \left( \left( \frac{2}{\gamma + 1} \right) \left( 1 + \frac{\gamma - 1}{2} M^2 \right) \right)^{\frac{\gamma + 1}{2(\gamma - 1)}} \quad (3.4)$$

where  $A^*$  is the area of the throat. The throat diameter of the nozzle has been arrived at 20 mm based on the calculation of time taken for emptying the storage tank available in the experimental set-up. For obtaining a Mach number of 1.5 at the nozzle exit, the area ratio calculated from Equation 3.4 is  $A/A^*=1.176$  and the corresponding exit diameter is 21.69 mm. The Prandtl-Meyer angle for a Mach number 1.5 is  $11.905^\circ$ . From this, the slope at B is determined as  $3.968^\circ$ . For the first parabola AB, the coordinates at A is taken as (0, 0) and slope at A is  $0^\circ$ . Applying these conditions in Equations 3.1 and 3.2, the following Equations 3.5 and 3.6 are obtained as:

$$Q + \sqrt{T} = 0 \quad (3.5)$$

$$P + 0.5ST^{-0.5} = 0 \quad (3.6)$$

The diameter of the nozzle at which the first parabola ends *ie.* at point B, is 20.35 mm and the corresponding slope is  $3.968^\circ$ . The equations for coordinate and slope become;

$$0.1754 = Px_B + Q + \sqrt{(Sx_B + T)} \quad (3.7)$$

$$0.0693 = P + 0.5S(Sx_B + T)^{-0.5} \quad (3.8)$$

The constants  $P$ ,  $Q$ ,  $S$ , and  $T$  can be found by solving Equations 3.5, 3.6, 3.7, and 3.8 using the Newton-Raphson method with central derivative and quadratic extrapolation.

Table 3.1: Nozzle coordinates of *PM/3*

<b>x (mm)</b>	<b>Radius (mm)</b>
0	10
0.78	10.05
1.75	10.10
3.17	10.15
5.15	10.18
5.51	10.20
7.05	10.28
8.74	10.38
10.65	10.48
12.89	10.58
15.67	10.68
19.83	10.78
25.13	10.85

The initial values for optimisation are  $P = -1.3$ ,  $Q = -283$ ,  $S = 807$ , and  $T = 80614$ .

The optimum length of the parabola *AB* is calculated to be 5.15 mm.

For the second parabola *BC*, the coordinates at *B* is taken as (0, 0) and slope at *B* is  $3.968^0$ . Applying these conditions in Equations 3.1 and 3.2, the following Equations 3.9 and 3.10 are obtained as:

$$Q + \sqrt{T} = 0 \quad (3.9)$$

$$P + 0.5ST^{-0.5} = 0.0693 \quad (3.10)$$

The diameter of the nozzle at which the second parabola ends *ie.* at point *C*, is 21.69 mm and the corresponding slope is  $0^0$ . The equations for coordinate and slope become;

$$0.67 = Px_c + Q + \sqrt{Sx_c + T} \quad (3.11)$$

$$0 = P + 0.5S(Sx_c + T)^{-0.5} \quad (3.12)$$

The constants  $P$ ,  $Q$ ,  $S$ , and  $T$  can be found by solving Equations 3.9, 3.10, 3.11, and 3.12 using the Newton-Raphson method with central derivative and quadratic

extrapolation. The initial values for optimisation are  $P = -1.3$ ,  $Q = -283$ ,  $S = 807$ , and  $T = 80614$ . The optimum length of the parabola  $BC$  is calculated to be 19.98 mm. The axial and radial coordinates of the  $PM/3$  nozzle contour are provided in Table 3.1.

### 3.1.1.2 Double Parabolic $PM/4$ Nozzle

The initial slope of parabola  $AB$ (Figure 3.1) is zero and the final slope is taken as one-fourth of Prandtl-Meyer angle. For the first parabola  $AB$ , the coordinates at  $A$  is taken as  $(0,0)$  and slope at  $A$  is  $0^0$ . The diameter of the nozzle at which the first parabola ends *ie.* at point  $B$ , is 20.24 mm and the corresponding slope is  $2.98^0$ . Four equations are obtained by applying initial and final coordinates and corresponding slopes to Equation 3.1 and 3.2.

$$Q + \sqrt{T} = 0 \quad (3.13)$$

$$P + 0.5ST^{-0.5} = 0 \quad (3.14)$$

$$0.1181 = Px_B + Q + \sqrt{Sx_B + T} \quad (3.15)$$

$$0.052 = P + 0.5S(Sx_B + T)^{-0.5} \quad (3.16)$$

By solving these four equations with the same method as discussed in section 3.1.1.1, the optimum length of the parabola  $AB$  is calculated to be 4.51 mm. Similarly, the optimum length of parabola  $BC$  is 29.01 mm. The axial and radial coordinates of the  $PM/4$  nozzle contour are provided in Table 3.2.

Table 3.2: Nozzle coordinates of *PM/4*

<b>x (mm)</b>	<b>Radius (mm)</b>
0	10
0.2	10.01
0.4	10.02
0.85	10.04
1.36	10.06
1.98	10.08
2.79	10.10
4.51	10.12
5.49	10.17
6.51	10.22
8.69	10.32
11.1	10.42
13.83	10.52
17.05	10.62
21.14	10.72
27.76	10.82
33.52	10.85

### 3.1.1.3 Double Parabolic *PM/5* Nozzle

The initial slope of parabola *AB* (Figure 3.1) is zero and the final slope is taken as one-fifth of Prandtl-Meyer angle. For the first parabola *AB*, the coordinates at *A* is taken as (0,0) and slope at *A* is  $0^0$ . The diameter of the nozzle at which the first parabola ends *ie.* at point *B*, is 20.17 mm and the corresponding slope is  $2.38^0$ . Four equations are obtained by applying initial and final coordinates and corresponding slopes to Equation 3.1 and 3.2.

Table 3.3: Nozzle coordinates of *PM/5*

<b>x (mm)</b>	<b>Radius (mm)</b>
0	10
0.25	10.01
0.51	10.02
1.11	10.04
1.87	10.06
3.03	10.08
4.23	10.09
5.45	10.14
6.73	10.19
9.44	10.29
12.42	10.39
15.77	10.49
19.66	10.59
24.45	10.69
31.32	10.79
41.40	10.85

$$Q + \sqrt{T} = 0 \quad (3.17)$$

$$P + 0.5ST^{-0.5} = 0 \quad (3.18)$$

$$0.0868 = Px_B + Q + \sqrt{Sx_B + T} \quad (3.19)$$

$$0.0416 = P + 0.5S(Sx_B + T)^{-0.5} \quad (3.20)$$

By solving these four equations with the same method as discussed in section 3.1.1.1, the optimum length of the parabola *AB* is calculated to be 4.23 mm. Similarly, the optimum length of parabola *BC* is 37.17 mm. The axial and radial coordinates of the *PM/5* nozzle contour are provided in Table 3.3.

### 3.1.2 Bell Nozzle

In Figure 3.1, *AB<sub>1</sub>C* is the divergent portion of Bell nozzle, *O* is the centre of the arc *AB<sub>1</sub>* and radius given by  $0.382R_t$ , where  $R_t$  is the radius of the throat. The arc *AB<sub>1</sub>* is drawn in such a way that at point *B*, the slope is half of the design Prandtl-Meyer

angle.  $B_1C$  is a parabola which can be drawn by the method explained in section 3.1.1. The length of the divergent portion of the nozzle is taken same as that of the double parabolic nozzle for the sake of comparison. The axial and radial coordinates of the Bell nozzle contour are provided in Table 3.4. In the table (0, 10) and (0.4, 10.02) are the initial and final coordinates of the arc of radius 3.82 mm and centre  $O$  as shown in Figure 3.1. The initial and final coordinates of the parabola are (0.4, 10.02) and (25.13, 10.845) respectively.

Table 3.4: Nozzle coordinates of Bell

<b>x (mm)</b>	<b>Radius (mm)</b>
0	10
0.4	10.02
0.99	10.07
1.58	10.12
2.83	10.22
4.18	10.32
5.67	10.42
7.34	10.52
9.26	10.62
11.62	10.72
14.90	10.82
25.13	10.85

### 3.1.3 Conical Nozzle

In Figure 3.1,  $AC$  is the contour of the conical nozzle which has a cone angle of  $2.14^\circ$ . The length of the divergent portion of the nozzle is taken identical as that of the double parabolic nozzle for the sake of comparison. The initial and final coordinates of the conical nozzle are (0, 10) and (25.13, 10.85) respectively.

### 3.1.4 Convergent Portion of the Nozzle

The design of the convergent portion of a *CD* nozzle is relatively simple as it encounters a favourable pressure gradient. The converging portion of the *CD* nozzle is identical with the contour developed by Panda and Seasholtz (1999). The axial and radial coordinates of the convergent contour are provided in Table 3.5.

Table 3.5: Coordinates of the convergent portion of the *CD* nozzle

<b>x (mm)</b>	<b>Radius (mm)</b>
0	34.05
2.43	34.00
17.01	32.00
24.47	30.00
30.43	28.00
35.61	26.00
40.29	24.00
44.61	22.00
48.66	20.00
52.50	18.00
56.16	16.00
59.57	14.00
63.97	12.27
76.06	10.27
77.67	10.16
80.00	10.06
84.21	10.00

## 3.2 NOZZLE FABRICATION

The nozzles were manufactured at GPS Engineering Chennai. Inlet, throat and exit diameters of all the nozzles are 68.10 mm, 20 mm and 21.69 mm respectively. The length of the convergent portion of all the nozzles is 84.21 mm. The divergent length

of conical, bell and double parabolic ( $PM/3$ ) nozzles are identical and equal to 25.13 mm. However, double parabolic nozzles with  $PM/4$  and  $PM/5$  profiles have a divergent length of 33.52 mm and 41.40 mm respectively. All the nozzles are made of stainless steel and shown in Figure 3.2. The Fig. 3.3 (a), 3.3 (b), 3.3 (c), 3.3 (d), and 3.3 (e) show the drawings of conical, bell,  $PM/3$ ,  $PM/4$ , and  $PM/5$  double parabolic nozzles respectively.



Fig. 3.2 Nozzles used for experimentation

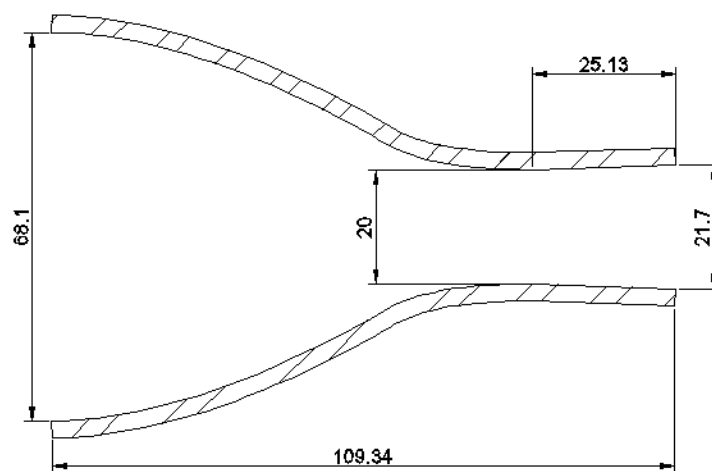


Fig 3.3 (a) Machine drawing of conical nozzle



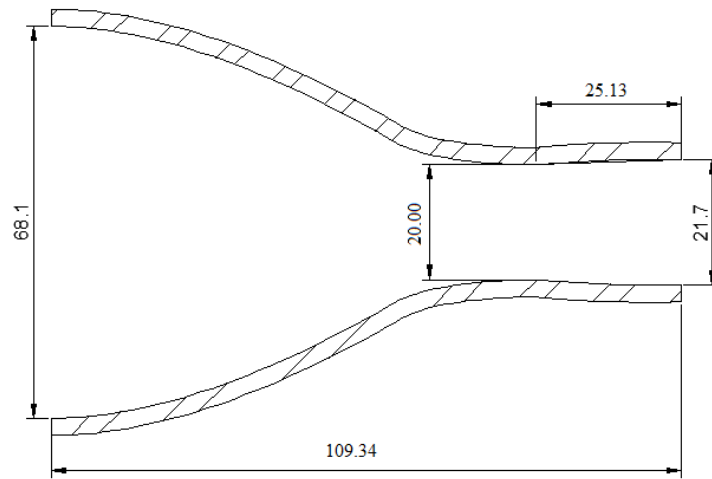


Fig. 3.3 (b) Machine drawing of bell nozzle

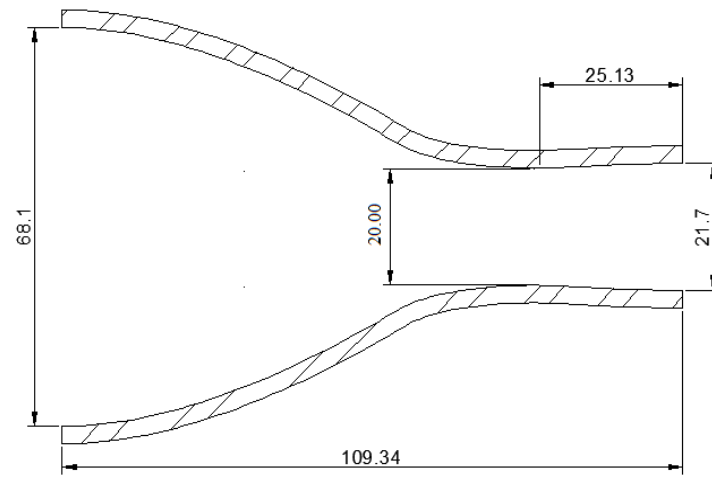


Fig 3.3 (c) Machine drawing of *PM/3* double parabolic nozzle

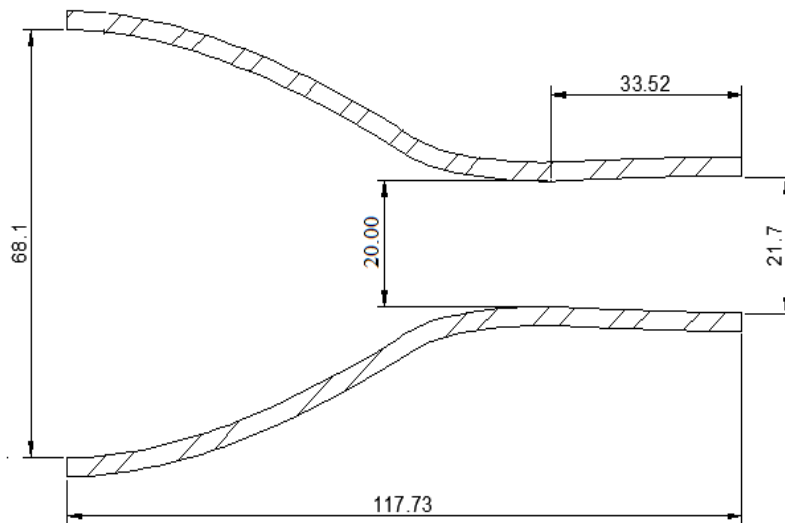


Fig 3.4 (d) Machine drawing of *PM/4* double parabolic nozzle

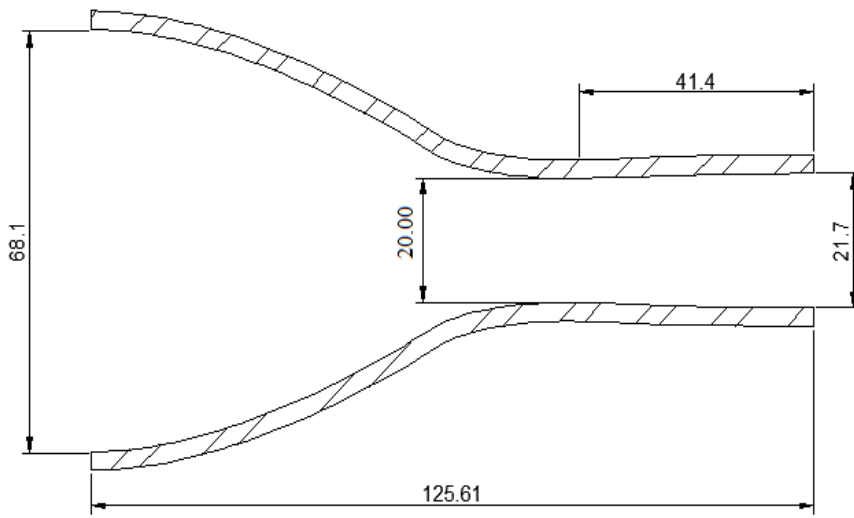


Fig. 3.5 (e) Machine drawing of *PM/5* double parabolic nozzle

## **CHAPTER - 4**

### **EXPERIMENTATION ON SUPERSONIC NOZZLES**

The experimental investigation was carried out at Gas Dynamics lab, IIT Madras under Technical Education Quality Improvement Programme (TEQIP Phase II, Government of India scheme). The experimentation involves two set-ups such as flow set-up and measuring set-up.

#### **4.1 SUPERSONIC FREE JET FACILITY**

The supersonic free jet facility consists of components and arrangements for producing supersonic flow. The main components are compressor, storage tank, pressure regulating valve, settling chamber, nozzle holder and convergent divergent nozzles.

##### **4.1.1 Compressor**

The compressor used is Khosla-Crepelle2HA2S two-stage reciprocating compressor and is shown in Figure 4.1.

The compressor has a flow rate of  $8.5 \text{ m}^3/\text{min}$  and a maximum pressure of 17.16 bar. The motor rating is 75 kW and the speed is 750 rpm. Compressed air from Khosla-Crepelle compressor is free from oil particles.

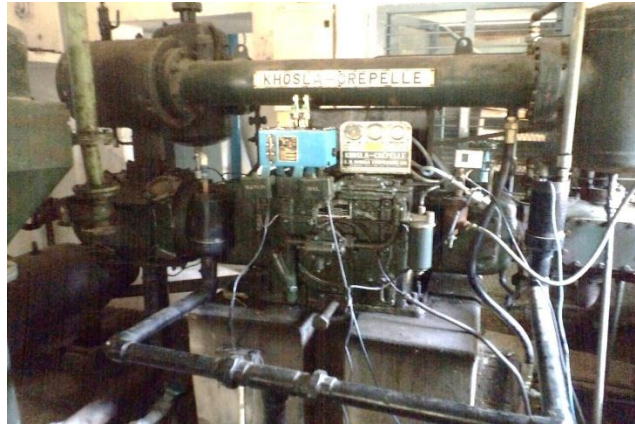


Fig. 4.1 Compressor

#### 4.1.2 Storage Tank

Three storage tanks of 10 m<sup>3</sup> capacity each are used for storing compressed air maintained at a pressure of 12 bar. The storage tanks are shown in Figure 4.2.



Fig. 4.2 Storage tanks

#### 4.1.3 Settling Chamber and Pressure Regulating Valve

The role of a settling chamber is to eliminate swirl and unsteadiness from the flow. The settling chamber consists of a special honeycomb and a series of screens. It is the most efficient method to suppress the lateral component of turbulence and also to make the flow more parallel to the nozzle axis. Figure 4.3 shows the settling chamber, pressure regulating valve, nozzle holder, nozzle etc.



Fig. 4.3 Settling chamber

#### 4.1.4 Nozzles

Figure 4.4 shows the different nozzles used for experimentation at the end of settling chamber. The nozzles include conical nozzle, bell nozzle and double parabolic nozzles (*PM/3*, *PM/4*, and *PM/5*) as shown in figure.



Fig. 4.4 CD nozzles used for experiments

The inlet, throat and exit diameters of all the nozzles are 68.10 mm, 20 mm and 21.69 mm respectively. The design Mach number of the nozzles is 1.5.

## 4.2 EXPERIMENTAL MEASUREMENT TECHNIQUES

The experimental set-up for measurements consists of pressure measuring devices and Schlieren imaging technique.

### 4.2.1 Pressure Measuring Devices

The pressure in the settling chamber was manually controlled by a pressure regulating valve. The stagnation pressure in the settling chamber was observed by a Bourdon tube pressure gauge and also by a pressure transducer as shown in Figure 4.3. The static and stagnation pressures at the nozzle exit were measured by pressure probes as shown in Figures 4.5 (a) and (b) respectively.



Fig. 4.5 (a) Static pitot probe

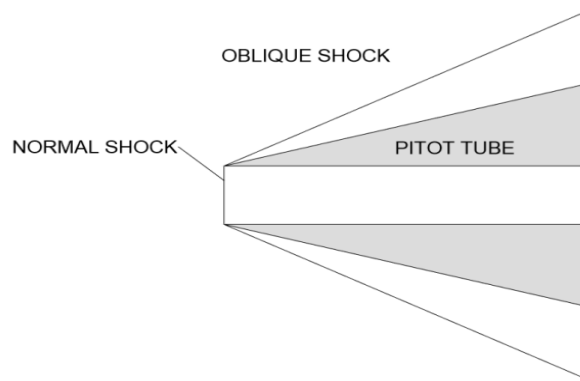


Fig. 4.5 (b) Stagnation pitot tube

The leading edge of the static pressure probe was closed and four holes were drilled on its surface at a distance of 4.89 mm along its circumference with a probe outer diameter of 1.524 mm. The pressure probes were fitted in a three-axis traverse of pitch 3 mm as shown in Figure 4.6.



Fig. 4.6 Three-axis traverse

#### 4.2.2 Schlieren Set-up

The flow field was visualised by using a conventional Z-type Schlieren system as shown in Figure 4.7, by using two 30 cm diameter and 200 cm focal length spherical mirrors. The light was accurately focused for avoiding aberrations and misalignment of the optical components. Each of the components was carefully aligned to pass the light without interference or distortion. A razor blade set perpendicular to the flow direction was used as a filter and the images were taken by photron *FASTCAM* viewer with a resolution of 1024x1024 and 2000 fps. The number of frames taken during a single run is 5457. The camera used is *FASTCAM SA4* model *500K-M1*, which can take images at 10000 frames per second and shown in Figures 4.8 (a) and (b).

The physical basis for Schlieren imaging transpires from Snell's law, which points towards the slowing down of light upon interaction with matter. In a homogeneous media, light travels uniformly at a constant velocity. But in an inhomogeneous media, light rays refract and deflect from their normal path, resulting in a Schlieren image. Snell's law states that the ratio of the sines of the angle of incidence and refraction is equal to the reciprocal to the ratio of the incidence of refraction.

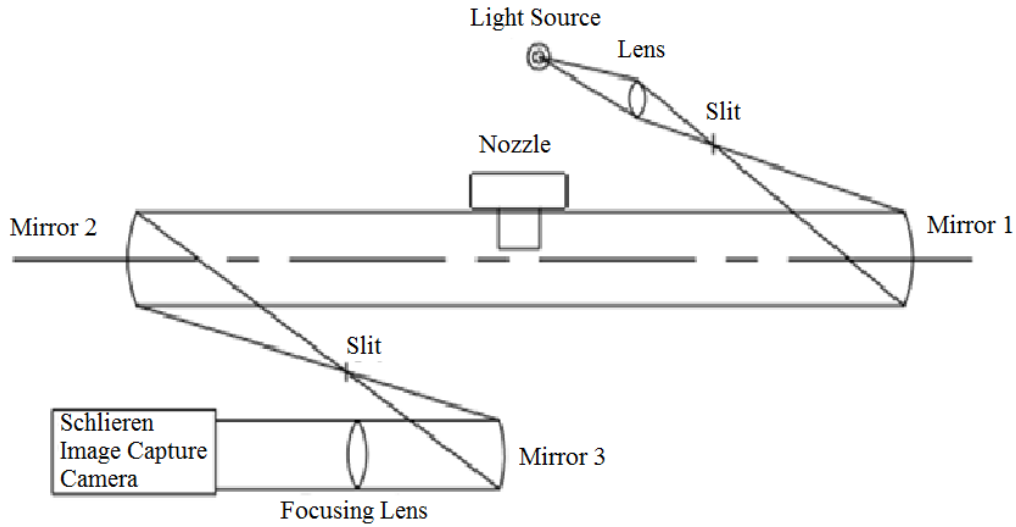


Fig. 4.7 Z-type Schlieren system

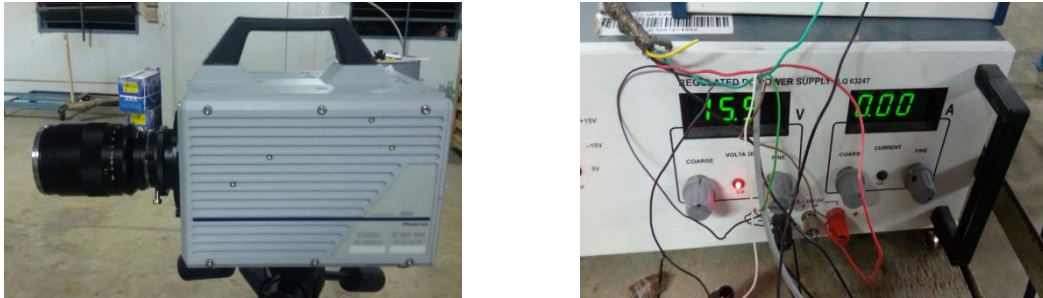


Fig 4.8 (a) Photron *FASTCAM* viewer (b) *DAQ* system

### 4.3 EXPERIMENTATION ON NOZZLES

The experimental investigation was carried out in a supersonic free jet test facility having a storage tank of 30 m<sup>3</sup> capacity maintained at a pressure of 12 bar. Compressed air from the compressor with a delivery pressure of 17.5 bar and a flow rate of 8.6 m<sup>3</sup>/minute is fed to a storage tank to maintain the above pressure. The experimental set up is shown in Figure 4.9.



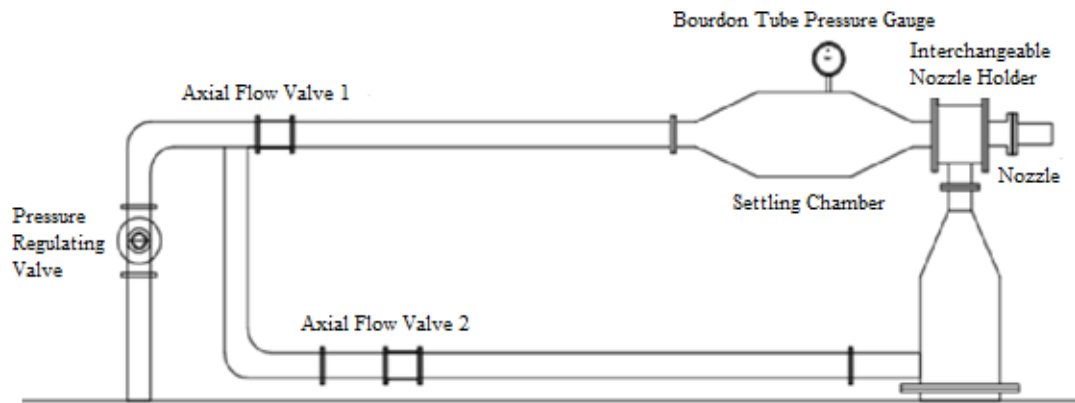


Fig. 4.9 Schematic diagram of the experimental set-up

Stagnation pressure in the settling chamber was manually controlled by a pressure regulating valve. Axial flow valves 1 and 2 are opened simultaneously for conducting experiments on coaxial dual nozzles when both primary and secondary jets are evolved. However axial flow valve 2 is kept closed for carrying out present experiments on a single jet emanating from convergent-divergent nozzles. The stagnation pressure in the chamber was observed by a Bourdon tube pressure gauge and also by a pressure transducer. At design condition of Mach number 1.5, the stagnation pressure required is 3.73 bar. The supersonic nozzles were mounted on an interchangeable nozzle holder downstream of the settling chamber unit and finally the jet exits directly to the ambient air. Static and stagnation pressure readings were taken at nozzle exit and also at an interval of 3 mm along the flow direction from the nozzle exit. Similar readings were taken for five vertical positions perpendicular to the nozzle axis at an interval of 3 mm along and perpendicular to the flow direction.

The static and stagnation pressures were measured by static pitot probe and stagnation pitot tube respectively. The pressure probe was housed in a 3 axis traverse of pitch 3 mm. The cylindrical pitot was connected to a KELLER pressure transducer of

pressure range 0-10 bar, accuracy 0.1% FS and resolution of 0.02% FS. Pressure signals were acquired at a sampling rate of 2 kHz and are digitally processed by the software Lab View to compute the mean pitot pressure at the various locations. The stagnation and static pressures were measured at 660 points in the flow field downstream of the nozzle and represented in Figure 4.10. The experimental data were measured at intervals of 3 mm in the axial and radial directions downstream of the nozzle exit.

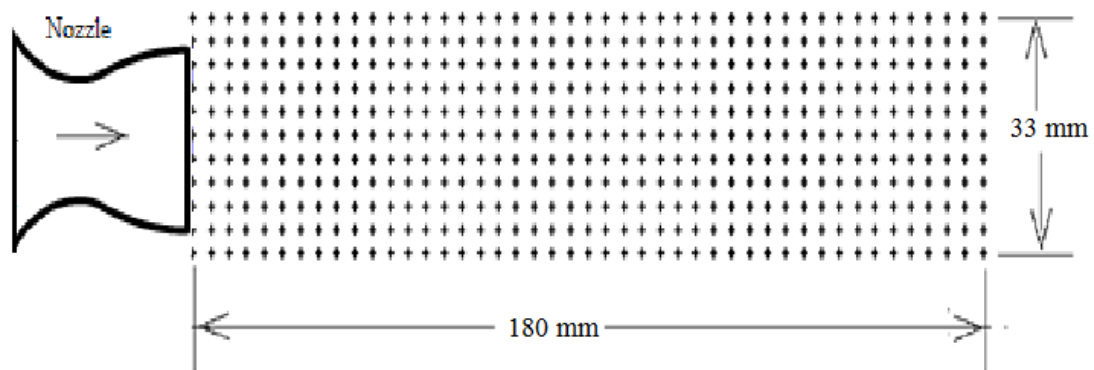


Fig. 4.10 Experimental measurement locations (660 positions)

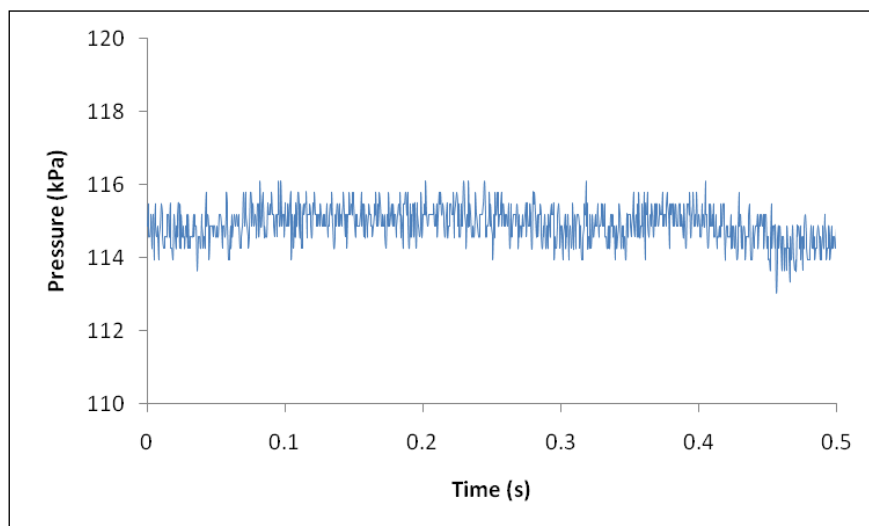


Fig. 4.11 Typical static pressure signal during centreline Pitot pressure measurement

Figure 4.11 shows a typical pressure signal obtained during the pitot pressure measurements. An average of one-second duration was taken as the mean steady pressure and the mean fluctuation was found to be less than 3% of mean value. A group average of five test runs at each position was taken for the analysis and found to be less than 2%, which is well within the expected uncertainty of 6.5%, indicating the reliability of the measured values. For the measurement of stagnation pressure, an uncertainty of 4% exists which includes the accuracy of the sensor ( $\pm 1\%$ ) and the functioning of mechanical elements. Pitot pressure measurement is invasive and uses a finite area tube which introduces errors besides the accuracy of the sensor ( $\pm 1\%$ ) such as accepted variation across the pitot area ( $\pm 1\%$ ) and the effect of viscosity. Rao *et al.* (2016) have already reported similar uncertainty estimates in their experimental work. The uncertainty analysis was carried out based on the experimental fluid mechanics procedures reported by Tropea *et al.* (2007).

The experimental work has been carried out in Gas dynamics lab, IIT Madras. The following procedures are initiated before proceeding with experimental measurements; by fixing required nozzle in the interchangeable nozzle holder, fixing pressure probes in the three-axis traverse, connecting pitot to pressure transducer etc. The static and stagnation pressures were measured at 660 points and 10 seconds are required for one run. A group average of five test runs at each position was taken for the analysis. Each nozzle is operated at 2 NPRs and a total of 40 hours are required for one course of nozzle experiments. The experiments have been done for 5 nozzles with Schlieren imaging and pressure measurements using 3 axis traverse.

## CHAPTER - 5

### NUMERICAL MODELLING & SIMULATION

Jet flow through the nozzle is governed by familiar fluid dynamic equations and the flow properties shall be predicted by solving these equations by applying appropriate boundary conditions.

#### 5.1 GOVERNING EQUATIONS

The governing equations of fluid flow represent mathematical statements of conservation laws of physics such as the law of conservation of mass, momentum, and energy. In the case of the high-speed jet, the governing equations used are Favre averaged continuity equation, momentum equations, and energy equation (Versteeg and Malalasekra, 1995). Here the air is treated as the ideal gas and so the ideal gas equation of state ( $p = \rho RT$ ) is used.

The equation for conservation of mass

$$\frac{\partial \bar{\rho}}{\partial t} + \text{div}(\bar{\rho}\tilde{\mathbf{U}}) = 0 \quad (5.1)$$

The equation for conservation of momentum

$$\begin{aligned} & \frac{\partial(\bar{\rho}\tilde{\mathbf{U}})}{\partial t} + \text{div}(\bar{\rho}\tilde{\mathbf{U}}\tilde{\mathbf{U}}) \\ &= -\frac{\partial \bar{P}}{\partial x} + \text{div}(\mu \text{grad}\tilde{\mathbf{U}}) + \left[ -\frac{\partial(\bar{\rho}u'^2)}{\partial x} - \frac{\partial(\bar{\rho}u'v')}{\partial y} - \frac{\partial(\bar{\rho}u'w')}{\partial z} \right] + S_{Mx} \end{aligned} \quad (5.2)$$

(5.3)

$$\begin{aligned} & \frac{\partial(\bar{\rho}\tilde{V})}{\partial t} + \text{div}(\bar{\rho}\tilde{V}\tilde{\mathbf{U}}) \\ &= -\frac{\partial\bar{P}}{\partial y} + \text{div}(\mu\text{grad}\tilde{V}) + \left[ -\frac{\partial(\bar{\rho}u'v')}{\partial x} - \frac{\partial(\bar{\rho}v'^2)}{\partial y} - \frac{\partial(\bar{\rho}v'w')}{\partial z} \right] + S_{My} \end{aligned}$$

(5.4)

$$\begin{aligned} & \frac{\partial(\bar{\rho}\tilde{W})}{\partial t} + \text{div}(\bar{\rho}\tilde{W}\tilde{\mathbf{U}}) \\ &= -\frac{\partial\bar{P}}{\partial z} + \text{div}(\mu\text{grad}\tilde{W}) + \left[ -\frac{\partial(\bar{\rho}u'w')}{\partial x} - \frac{\partial(\bar{\rho}v'w')}{\partial y} - \frac{\partial(\bar{\rho}w'^2)}{\partial z} \right] + S_{Mz} \end{aligned}$$

The equation for conservation of energy

$$\frac{\partial(\bar{\rho}\tilde{e})}{\partial t} + \text{div}(\bar{\rho}\tilde{e}\tilde{\mathbf{U}}) = -\bar{P}\text{div}\tilde{\mathbf{U}} + \text{div}(k\text{grad}T) + \Phi + S_e \quad (5.5)$$

## 5.2 TURBULENCE MODELLING

Turbulence modelling is the construction and use of a numerical model to forecast the turbulent characteristics. Turbulence causes the appearance of eddies in the flow with a wide range of time and length scales which interact in a dynamically complex way. A common approach is to average the governing equations of the flow, in order to focus on large-scale and non-fluctuating features of the flow.

### 5.2.1 Closure Problem in Turbulence

In the case of turbulent flow, pressure and velocity components in the Navier-Stokes equation may be decomposed into mean and fluctuating part. The mean flow can be governed by the Reynolds-Averaged Navier-Stokes (*RANS*) equations which are obtained by averaging Navier-Stokes equations. The nonlinear term  $-\overline{\rho u'_i u'_j}$  appearing

in the *RANS* equations causes an additional turbulent shear stress called Reynolds stress. The Reynolds stress is the component of the total stress tensor in a fluid obtained by averaging the Navier-Stokes equations to account for turbulent fluctuations in fluid momentum. We have to close the *RANS* equations for obtaining the equations which contain only the mean velocity and pressure. This is obtained by modelling the Reynolds term as a function of mean flow. This is the closure problem in turbulence.

### 5.2.2 Boussinesq's Hypothesis

In 1877 Boussinesq proposed a relation between Reynolds stress and mean rates of deformation. He was the first person who introduced the concept of eddy viscosity to attack the closure problem. Equation 5.6 was introduced by Boussinesq in which  $\mu_t$  is the turbulence eddy viscosity.

$$-\rho \overline{u'_i u'_j} = \mu_t \left( \frac{\partial U_i}{\partial x_j} + \frac{\partial U_j}{\partial x_i} \right) - \frac{2}{3} \rho k \delta_{ij} \quad (5.6)$$

where  $k$  is the turbulent kinetic energy per unit mass,  $k = \frac{1}{2} \overline{u'_i u'_i}$

$$\text{and } \delta_{ij} \text{ is Kronecker delta} = \begin{cases} 0, & \text{for } i \neq j \\ 1, & \text{for } i = j \end{cases}$$

The expressions for turbulent viscosity and turbulent kinetic energy vary across different turbulence models. The most common method of classifying the turbulence model is according to the additional number of partial differential equations that are being solved. The zero equation model (mixing length model), one equation model (Spalart-Allmaras model), two equation models ( $k$ - $\varepsilon$  and  $k$ - $\omega$  models) and seven equation model (Reynolds Stress Model) are some of the examples. In the present

study, Standard  $k$ - $\varepsilon$ ,  $RNG$   $k$ - $\varepsilon$  model, Realizable  $k$ - $\varepsilon$ , and Shear stress transport ( $SST$ )  $k$ - $\omega$  models were employed. Nallasami (1999) presented a review of turbulence models in which the flow solutions obtained with the  $k$ - $\varepsilon$  model, algebraic Reynold's stress model and Reynold's stress transport equation were analysed.

### 5.2.3 Standard $k$ - $\varepsilon$ Model

The standard  $k$ - $\varepsilon$  model has two model equations one for turbulent kinetic energy  $k$  and other for the rate of dissipation of turbulent kinetic energy per unit mass  $\varepsilon$ . Turbulent viscosity may be expressed as

$$\mu_t = \rho C_\mu \frac{k^2}{\varepsilon} \quad (5.7)$$

where,  $C_\mu$  is a dimensionless constant whose value is 0.09. The model equations for  $k$  and  $\varepsilon$  may be written as

$$\frac{\partial(\rho k)}{\partial t} + \text{div}(\rho k U) = \text{div} \left[ \frac{\mu_t}{\sigma_k} \text{grad} k \right] + 2\mu_t S_{ij} \cdot S_{ij} - \rho \varepsilon \quad (5.8)$$

$$\frac{\partial(\rho \varepsilon)}{\partial t} + \text{div}(\rho \varepsilon U) = \text{div} \left[ \frac{\mu_t}{\sigma_\varepsilon} \text{grad} \varepsilon \right] + C_{1\varepsilon} \frac{\varepsilon}{k} 2\mu_t S_{ij} \cdot S_{ij} - C_{2\varepsilon} \rho \frac{\varepsilon^2}{k} \quad (5.9)$$

The model equations for  $k$  and  $\varepsilon$  Equation (5.8) and (5.9), employs four constants namely,  $C_{1\varepsilon}$ ,  $C_{2\varepsilon}$ ,  $\sigma_k$  and  $\sigma_\varepsilon$ . By performing benchmark experiments, the values of these constants were found to be 1.44, 1.92, 1.00, and 1.30 respectively (Launder and Sharma, 1974). The velocity scale ' $V$ ' and length scale ' $l$ ' may be represented

$$\text{as } V = k^{1/2} \text{ and } l = \frac{k^{3/2}}{\varepsilon}$$

### 5.2.4 RNG $k$ - $\varepsilon$ Model

The renormalisation group (RNG) procedure systematically removes the small scales of motion from the governing equations by expressing their effects in terms of larger-scale motions and a modified viscosity term (Yakhot *et al.*, 1992). The model equations may be expressed as,

$$\frac{\partial(\rho k)}{\partial t} + \text{div}(\rho k U) = \text{div}[\alpha_k \mu_{\text{eff}} \text{grad} k] + \tau_{ij} \cdot S_{ij} - \rho \varepsilon \quad (5.10)$$

$$\frac{\partial(\rho \varepsilon)}{\partial t} + \text{div}(\rho \varepsilon U) = \text{div}[\alpha_k \mu_{\text{eff}} \text{grad} \varepsilon] + C_{1\varepsilon}^* \frac{\varepsilon}{k} \tau_{ij} \cdot S_{ij} - C_{2\varepsilon} \rho \frac{\varepsilon^2}{k} \quad (5.11)$$

with  $\tau_{ij} = -\overline{\rho u_i u_j} = 2\mu_t S_{ij} - \frac{2}{3} \rho k \delta_{ij}$  and  $\mu_{\text{eff}} = \mu + \mu_t$ . The values of model constants

are  $C_\mu = 0.0845$ ,  $\alpha_k = \alpha_\varepsilon = 1.39$ ,  $C_{1\varepsilon} = 1.42$ ,  $C_{2\varepsilon} = 1.68$  and  $C_{1\varepsilon}^* = C_{1\varepsilon} - \frac{\eta \left(1 - \frac{\eta}{\eta_0}\right)}{1 + \beta \eta^3}$ .

$$\eta = \frac{k}{\varepsilon} \sqrt{2S_{ij} \cdot S_{ij}}, \eta_0 = 4.377, \beta = 0.012 \text{ (Yakhot *et al.*, 1992)}$$

### 5.2.5 Realizable $k$ - $\varepsilon$ Model

The realizable  $k$ - $\varepsilon$  model has the same model equation for turbulent kinetic energy ( $k$ ) as in the standard  $k$ - $\varepsilon$  model. The model equation for the rate of viscous dissipation ( $\varepsilon$ ) has been modified as

$$\frac{\partial}{\partial t}(\rho \varepsilon) + \text{div}(\rho \varepsilon U) = \text{div} \left[ \frac{\mu_t}{\sigma_\varepsilon} \text{grad} \varepsilon \right] + \rho C_1 S \varepsilon - \rho C_2 \frac{\varepsilon^2}{k + \sqrt{\nu \varepsilon}} \quad (5.12)$$



$$\text{where, } C_1 = \max \left[ 0.43, \frac{\eta}{\eta + 5} \right], \quad \eta = S \frac{k}{\varepsilon}, \quad S = \sqrt{2S_{ij}S_{ij}}$$

Now, the turbulent viscosity may be expressed as,  $\mu_t = \rho C_\mu \frac{k}{\varepsilon}$  where,

$$C_\mu = \frac{1}{A_0 + A_s \frac{kU^*}{\varepsilon}}$$

is a variable unlike in the case of standard  $k-\varepsilon$  model.  $A_0=4.04$ ,

$A_s$ , and  $U^*$  are functions of velocity gradients. The value of constants  $\sigma_\varepsilon$  and  $C_2$  are found to be 1.2 and 1.9 respectively (Shih *et al.*, 1995).

### 5.2.6 SST $k-\omega$ Model

In the case of the  $k-\omega$  model, the rate of viscous dissipation  $\varepsilon$  is replaced by turbulence frequency  $\omega = \frac{\varepsilon}{k}$ . Correspondingly the length scales and velocity scales are calculated by the relation  $\nu = \sqrt{k}$  and  $t = \frac{\sqrt{k}}{\omega}$  (Menter, 1994). The model equations for  $k$  and  $\omega$  are as follows

$$\frac{\partial(\rho k)}{\partial t} + \text{div}(\rho k \bar{u}) = \text{div} \left[ \left( \mu + \frac{\mu_t}{\sigma_k} \right) \text{grad}(k) \right] + \left( 2\mu_t S_{ij} S_{ij} - \frac{2}{3} \rho k \frac{\partial \bar{u}_i}{\partial x_j} \delta_{ij} \right) - \beta^* \rho k \omega \quad (5.13)$$

$$\frac{\partial(\rho \omega)}{\partial t} + \text{div}(\rho \omega \bar{u}) = \text{div} \left[ \left( \mu + \frac{\mu_t}{\sigma_{\omega,1}} \right) \text{grad}(\omega) \right] + \gamma_2 \left( 2\rho S_{ij} S_{ij} - \frac{2}{3} \rho \omega \frac{\partial \bar{u}_i}{\partial x_j} \delta_{ij} \right) - \beta_2 \rho \omega^2 + 2 \frac{\rho}{\sigma_{\omega,2}} \frac{\partial k}{\partial x_k} \frac{\partial \omega}{\partial x_k} \quad (5.14)$$

The turbulent viscosity is given by  $\mu_t = \frac{\rho k}{\omega}$ . The Reynold stresses are then calculated in the same manner as that of a  $k-\varepsilon$  model.

## 5.3 NUMERICAL SIMULATIONS

In this section, four different turbulence models were employed for the numerical prediction of the flow field of the supersonic free jets emerging from convergent-divergent nozzles. The predicted results were then compared with the corresponding values obtained from literature (Panda and Seasholtz, 1999). The axial and radial components of velocity, temperature, and density of the supersonic free jets operating at Mach numbers 1.4 is compared with numerical predictions.

The simulations were done using a commercial *CFD* solver. The two dimensional compressible Reynolds Averaged Navier Stokes Equations (*RANS*) were solved in order to obtain the exact velocity field. Since the statistical averaging process was employed to obtain the *RANS* equations, additional unknowns were introduced in it. So to ensure closure of the *RANS* equations, additional equations are to be formulated. These additional equations are provided by the turbulence model. In the present study, four different turbulence models were employed *i.e* Standard  $k-\varepsilon$  model, *RNG*  $k-\varepsilon$  model, Realizable  $k-\varepsilon$  model and *SST*  $k-\omega$  model for the closure of the *RANS* equations. Density based coupled solver (*DBCS*) was employed to solve the discretized equations along with the initial conditions and appropriate boundary conditions.

### 5.3.1 Domain Selection and Mesh Generation

The geometry along with the boundary conditions are shown in Figure 5.1. The dimensions of the domain were taken as  $22D_e$  in the axial direction and  $5D_e$  in the radial direction (where ' $D_e$ ' is the nozzle exit diameter) after conducting domain independent study.

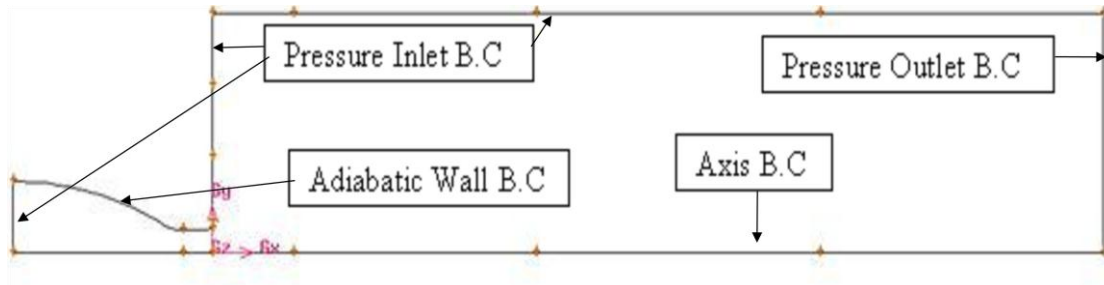


Fig. 5.1 Domain with boundary conditions

The boundary conditions are specified as follows. Nozzle inlet has a pressure inlet boundary condition and flows stagnation pressure (316000 Pa) is provided as the gauge total pressure. The other pressure inlet boundaries form part of the atmospheric domain and hence the gauge total pressure is set to ambient pressure (101325 Pa). Gauge total pressure at the pressure outlet boundary is also set to ambient pressure. Since the nozzle is a solid of revolution, axis boundary condition is applied at the bottom edge. No slip condition is provided at the nozzle walls.

### 5.3.2 Results and Discussions

The results obtained were compared with the experimental data obtained from Panda and Seasholtz (1999). The centerline profiles of velocity, temperature, and density as predicted by the Standard  $k-\varepsilon$  model,  $RNG\ k-\varepsilon$  model, Realizable  $k-\varepsilon$  model, and  $SST\ k-\omega$  model have plotted along with the corresponding experimental values. The radial profiles at  $x = 2D_e, 4D_e, 6D_e, 8D_e, 10D_e,$  and  $12D_e$  of these parameters were also plotted along with their experimental values.

Figure 5.2 shows a comparison of density along the jet axis from nozzle exit with experimental data and numerical predictions by four different turbulent models. It can be inferred from the plot that results predicted by the  $SST\ k-\omega$  model were much

closer to the experimental results, followed by the realizable  $k-\varepsilon$  model. The results predicted by the Standard  $k-\varepsilon$  model and the *RNG*  $k-\varepsilon$  model were extremely overpredicted and had large variations from the experimental values. Figures 5.3, 5.4 and 5.5 gave a comparison of the radial profile of density at  $2D_e$ , temperature at  $6D_e$ , velocity at  $8D_e$  respectively from nozzle exit with experimental data and numerical predictions. From these figures, it was found that the *SST*  $k-\omega$  model was giving the best results followed by Realizable  $k-\varepsilon$  model, Standard  $k-\varepsilon$  model, and *RNG*  $k-\varepsilon$  model in that order. *SST*  $k-\omega$  model gave overall a very good prediction of the shocks as well the velocity field. The *RNG*  $k-\varepsilon$  model and the Standard  $k-\varepsilon$  model gave overpredicted results especially in the case of temperature and density plots. Realizable  $k-\varepsilon$  model gave fairly good results.

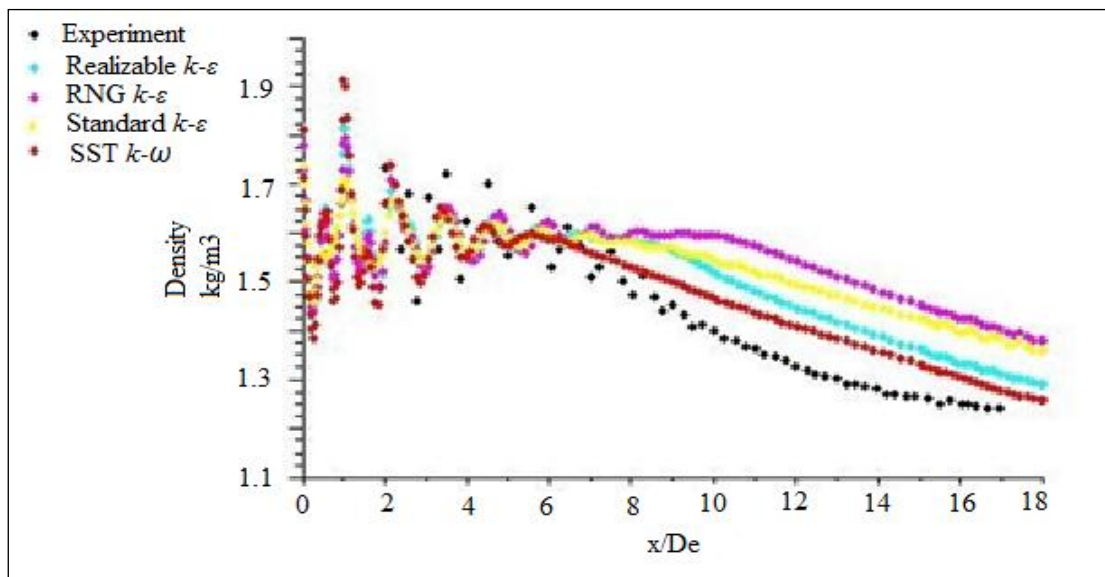


Fig. 5.2 Comparison of density (numerical) along the jet axis from nozzle exit with experimental data

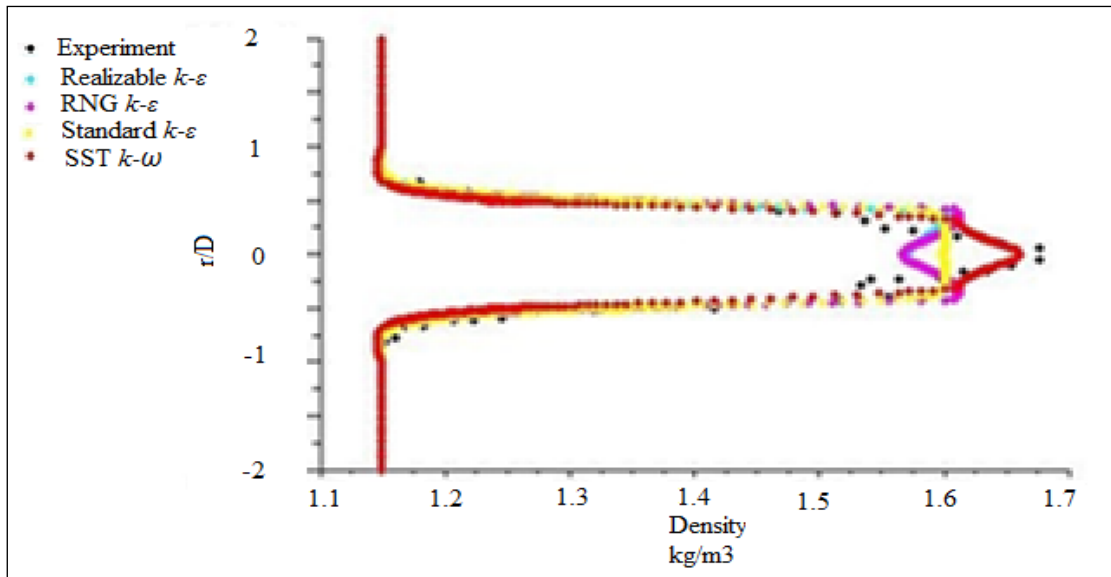


Fig. 5.3 Comparison of the radial profile of density (numerical) at  $2D_e$  from nozzle exit with experimental data

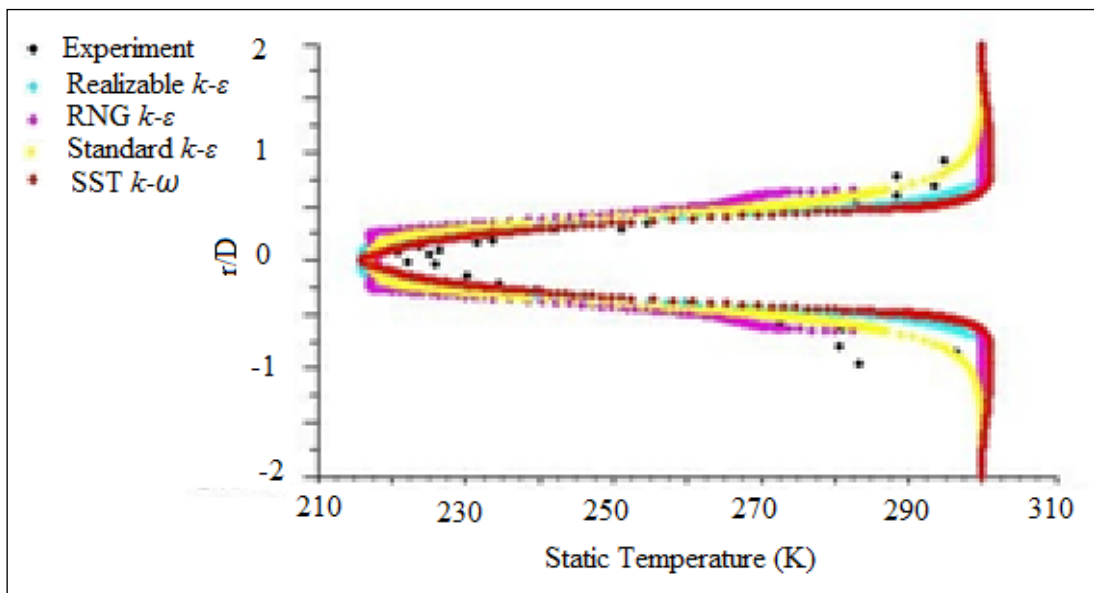


Fig. 5.4 Comparison of the radial profile of temperature (numerical) at  $6D_e$  from nozzle exit with experimental data

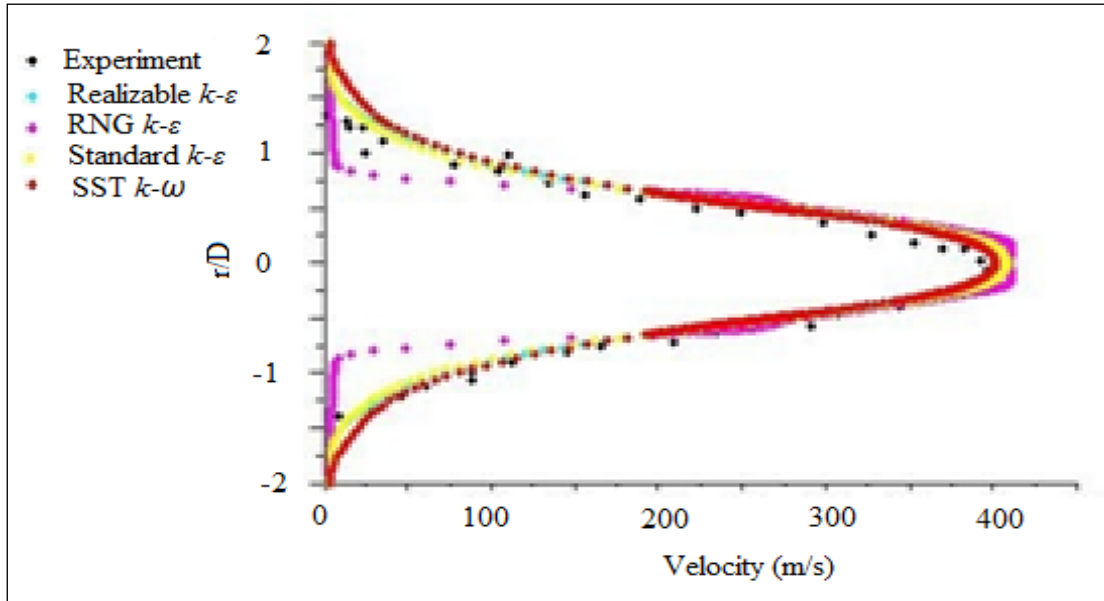


Fig. 5.5 Comparison of the radial profile of velocity (numerical) at  $8D_e$  from nozzle exit with experimental data

The high accuracy of the *SST k- $\omega$*  model may be attributed to its formulation. It incorporates the benefits of a *k- $\epsilon$*  model and a *k- $\omega$*  model in a single entity. It is a typical hybrid model which uses the formulations of a *k- $\omega$*  model in the near wall region (where a *k- $\epsilon$*  model's performance is often unsatisfactory) and in turn, uses the formulations of the Standard *k- $\epsilon$*  model in the fully turbulent region away from the wall. The failure of the Standard *k- $\epsilon$*  model may be due to the assumption that the term  $C_{\mu}$  is treated as a dimensionless constant. The moderate success of realizable *k- $\epsilon$*  model is attributable to the treatment of the term  $C_{\mu}$  as a variable. In the modelling of axisymmetric free jets, the modifications incorporated in the *RNG k- $\epsilon$*  model is not playing any significance. The analysis of the predictions and the comparison with the available experimental data reveals that the *SST k- $\omega$*  model is best suited for simulating compressible flow through a convergent-divergent nozzle.

## CHAPTER - 6

# COMPARISON OF DOUBLE PARABOLIC NOZZLE WITH $P/M=3$ PROFILE WITH CONICAL AND BELL NOZZLES

In the present chapter comparisons of the flow characteristics of the double parabolic nozzle with conical and bell nozzles have been carried out. The measured static pressure and Mach number of different nozzles at different nozzle pressure ratios ( $NPRs$ ) are compared. Schlieren imaging technique is used for finding shock cell length. Potential core length, supersonic core length, shock cell count, thrust, nozzle discharge coefficient and thrust coefficients of different nozzles are compared. Prediction of shock cell length of different nozzles at underexpanded conditions has also been conducted.

### 6.1 EXPERIMENTAL MEASUREMENTS & ANALYSIS

The exit flow from the nozzles of different contours was compared by static and stagnation pressure measurements together with Schlieren images captured from experiments.

#### 6.1.1 Static Pressure

The static pressure was measured at 660 points in the flow field downstream of the nozzle at intervals of 3 mm in the axial and radial directions from the nozzle exit. The static pressure data measured experimentally at different locations along the centre line of the jet from nozzle exit to a distance of 8 times nozzle exit diameter ( $D_e$ ) for different nozzles at  $NPR = 3.7$  is plotted in Figure 6.1.

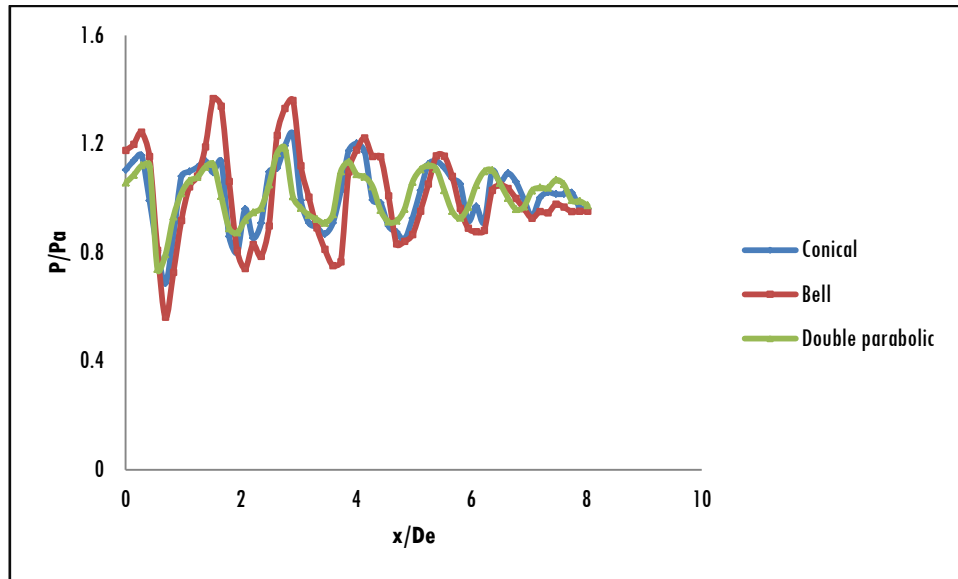


Fig. 6.1 Comparison of pressure variation along the jet axis for different nozzles at  $NPR = 3.7$  (Experimental)

Theoretically, the nozzle exit pressure must be atmospheric at the design condition. The nozzle exit pressure ( $x/D_e=0$ ) of the double parabolic nozzle is almost atmospheric whereas the other two nozzles have the values slightly higher than atmospheric. It is due to the internal shock formation at the throat especially in the case of the conical nozzle. There is also a formation of internal shock in bell nozzle along the circular arc region just downstream of the throat. The study reveals that the formation of these internal shocks can be considerably reduced by the introduction of parabolic arcs in the profile. Figure 6.2 shows the static pressure measurements at the under-expanded condition with  $NPR = 5$  at different locations along the centre line of the jet from the nozzle exit to a distance of  $8D_e$  for different nozzle configurations. The expected static pressure at nozzle exit at  $NPR = 5$  is 1.36 bar for isentropic conditions. However, a little higher value was observed in all the three nozzle configurations. The variation in Mach number clearly demonstrates the presence of shock cell structures in Fig. 6.2. Moreover, the variation in pressure is captured well downstream of the nozzle exit indicating the location of Mach disk.



In the case of conical and bell nozzles, the nozzle exit pressure is greater than atmospheric, even when they are operated at the design conditions. However, the pressure at the nozzle throat is the same for all the three nozzle configurations as the convergent portion for all the nozzles are identical. It may be noted that the convergent portion of the nozzle is working on a favourable pressure gradient ( $dp$  is negative) with subsonic flow velocities. The divergent section encounters supersonic flow which behaves in a complex mode, even for minute disturbances in the flow. Papamoschou *et al.* (2008) explained the presence of shocks spanning the entire jet of separated flow inside the nozzle indicating that flow downstream of the main shock accelerates to speeds that have locally supersonic values. This is accomplished by the slipstream forming sonic throat and later diverging, creating a wavy slip stream. Ostlund J. (2005) pointed out the formation of internal shocks in the divergent portion of the conventional *CD* nozzles such as conical and bell.

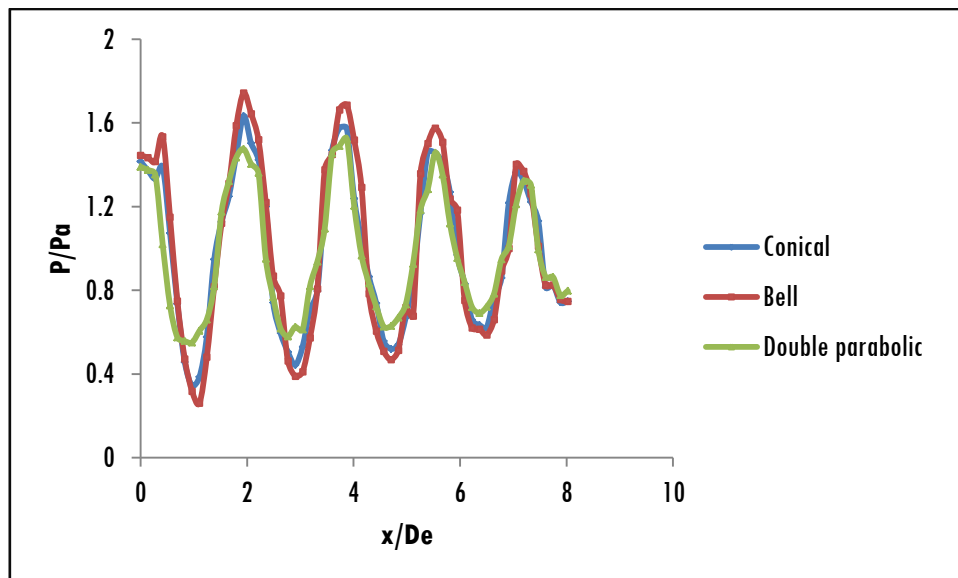


Fig. 6.2 Comparison of pressure variation along the jet axis for different nozzles at  $NPR = 5$  (Experimental)

### 6.1.2 Mach Number

Figure 6.3 shows the Mach number variation along the axis from the nozzle exit at  $NPR = 3.7$ . Here the area ratio of nozzle exit to the throat is 1.176 and hence the expected exit Mach number is 1.5. From the figure, it is clear that the Mach number at the exit of conical and bell nozzles are lower than that of the double parabolic nozzle. The formation of internal shocks in the vicinity of the throat region of conical and bell nozzles has lessened the exit Mach number.

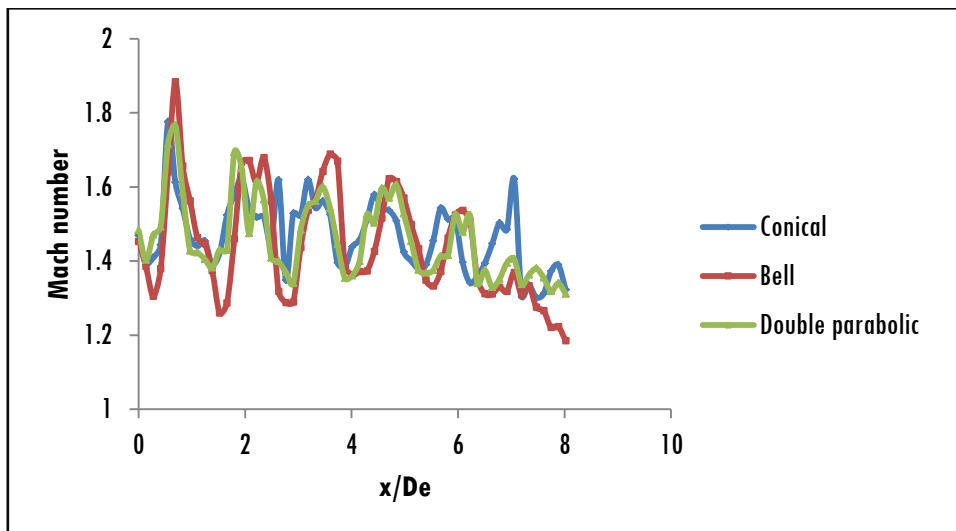


Fig. 6.3 Comparison of pressure variation along the jet axis for different nozzles at  $NPR = 3.7$  (Experimental)

The Mach number variations along the axis for different nozzle contours at  $NPR = 5$  is shown in Figure 6.4. The expected Mach number at the nozzle exit under these conditions based on area ratio is 1.5. Here also, the Mach numbers at the exit for conical and bell nozzles are less than the expected value because of the presence of internal shock formation in the regions close to the throat.

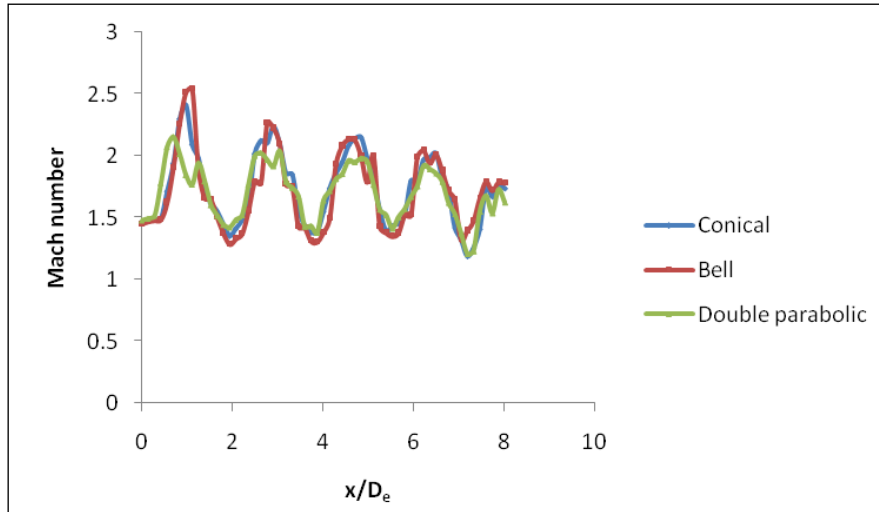


Fig. 6.4 Comparison of Mach number variation along the jet axis for different nozzles at  $NPR = 5$  (Experimental)

### 6.1.3 Schlieren Image

The Schlieren images (Figure 6.5) clearly demonstrate the presence of weak shock cells even at near design conditions for the conventional nozzles. From the figure, it is clear that the density variation of the double parabolic nozzle is lesser than that of the bell and conical nozzles.

Figures 6.6 - 6.8 show the Schlieren images of different nozzle profiles at different underexpanded conditions and seen to agree well with the results reported by Panda (1999). Schlieren images show multiple dark regions, which indicate the high-density compression zone, and the lighter regions linking them, represent the low-density expansion zone. The sharp vertical boundaries at the compression zone represent the extinction position of each shock in the shear layer. Shock cell structure of the conical, bell and double parabolic nozzles are similar and have approximately same shock cell lengths at same nozzle pressure ratios. From these figures, it may be inferred that the nozzle contour has less significance in the development of shock cell structure at under expanded conditions.

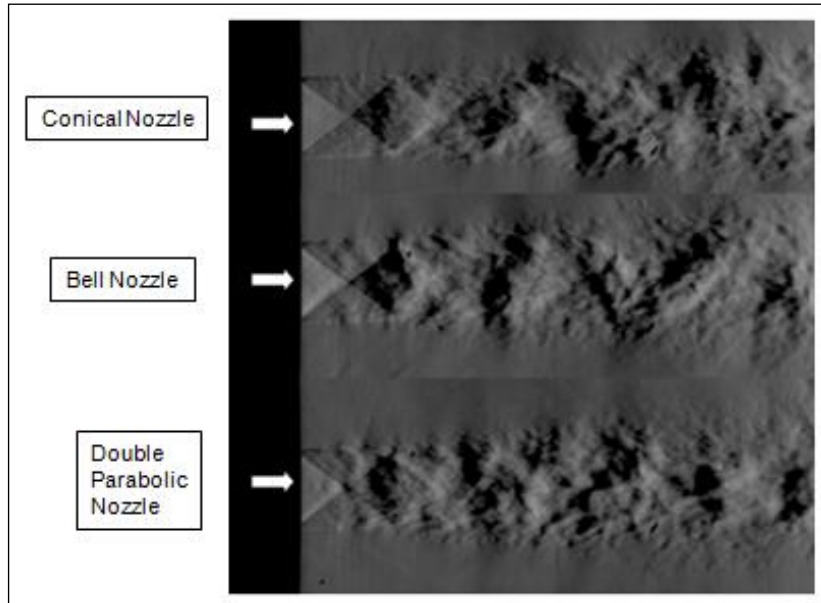


Fig. 6.5 Schlieren images of conical, bell, and double parabolic nozzle with  $PM/3$  profile at  $NPR = 3.7$  (Experimental)

Munday *et al.* (2011) reported that conical  $CD$  nozzles do not achieve a shock-free condition at a design Mach number ( $M_d = 1.5$ ) after analysing the shadowgraph images for the range of jet Mach numbers ( $M_j$ ) from 1.22 to 1.71. The profile of the  $CD$  nozzles diverges all the way from the throat to the exit creating an outward component of velocity in the exiting flow and causes a series of shock diamonds to exist, even when the nozzle is operated at correct expansion with perfect pressure match at the exit. It was also reported by Munday *et al.* (2009) that the flow exiting the outer edge of the nozzle will have a radially outward component of velocity under all conditions. In order to achieve a parallel flow, there must be turning of a supersonic flow, and this will produce a shock even when the pressures are matched perfectly.

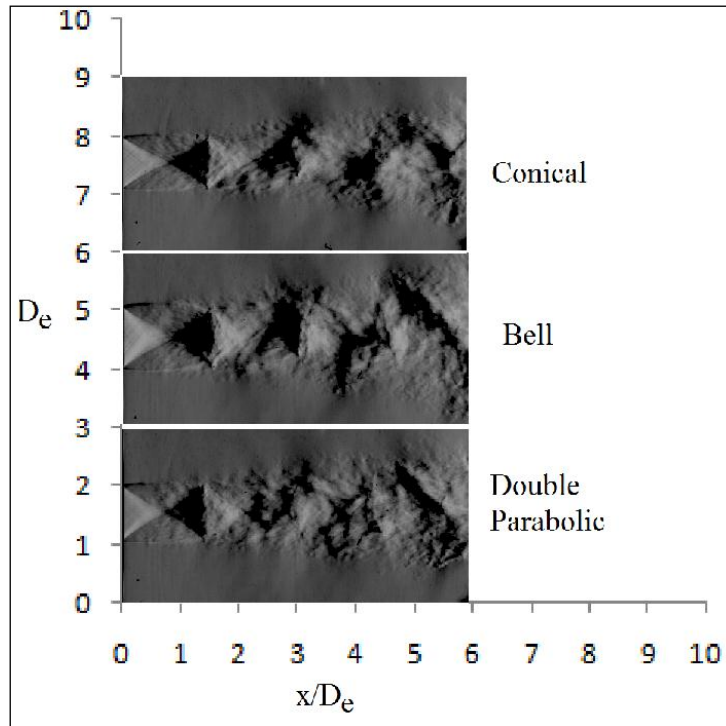


Fig. 6.6 Schlieren images of conical, bell, and double parabolic nozzle with  $PM/3$  profile at  $NPR = 4.5$  (Experimental)

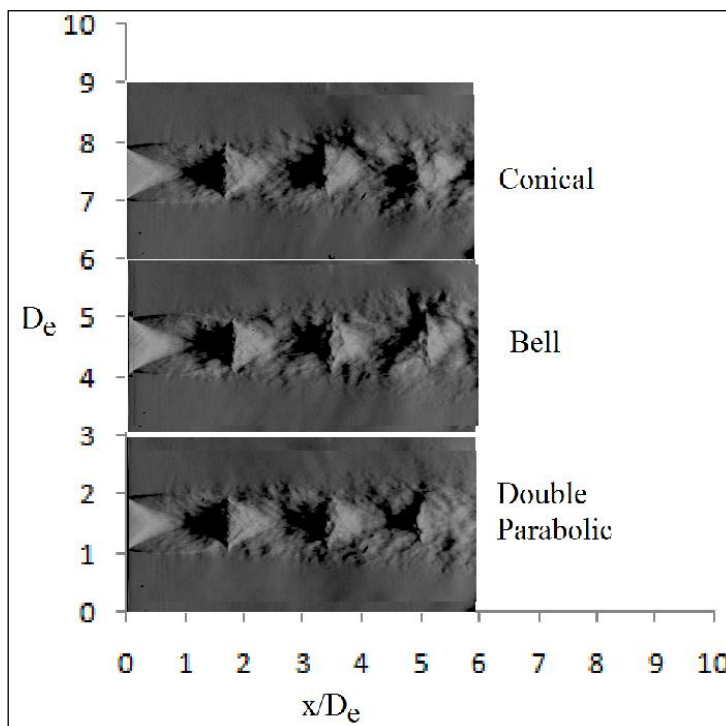


Fig. 6.7 Schlieren images of conical, bell, and double parabolic nozzle with  $PM/3$  profile at  $NPR = 5$  (Experimental)

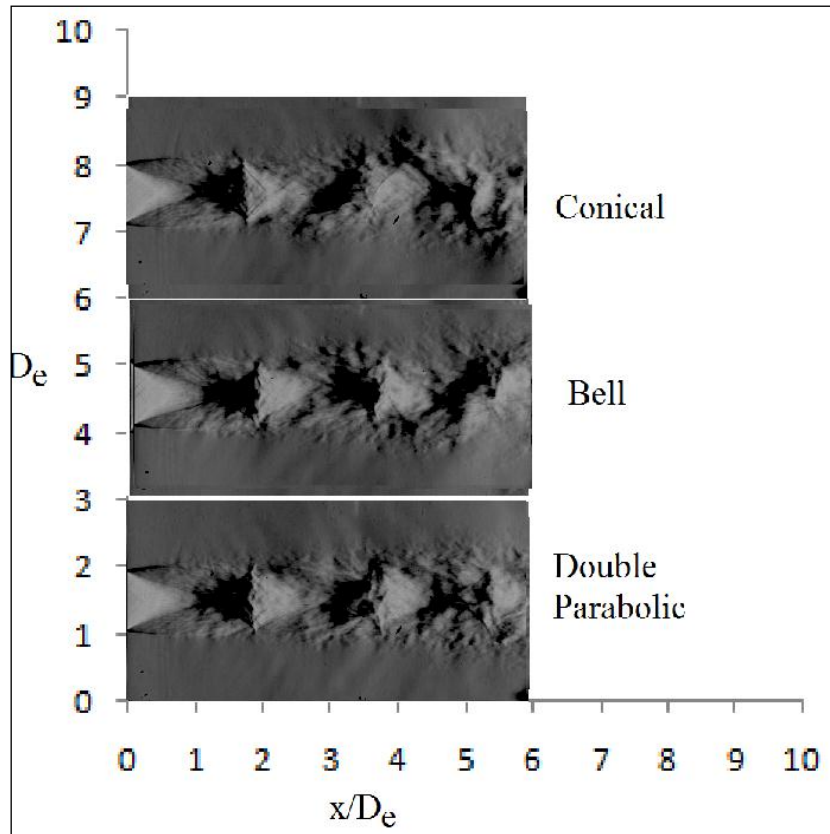


Fig. 6.8 Schlieren images of conical, bell, and double parabolic nozzle with  $PM/3$  profile at  $NPR = 5.5$  (Experimental)

Figure 6.9 shows the Schlieren images of flow through the conical nozzle at the overexpanded condition. At  $NPR = 3$  the nozzle exit pressure is in between second and third critical pressures and hence oblique shocks are formed from the nozzle exit. The flow tries to attain ambient pressure through a series of these compression and expansion waves. Even at design condition, there are shock waves in the flow (Figure 6.10). This is due to the sharp corner in the throat section of the convergent-divergent conical nozzle.

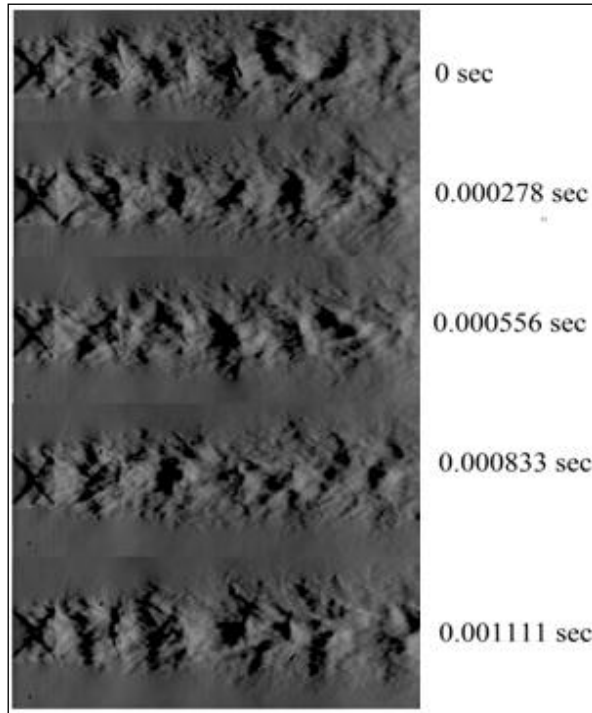


Fig. 6.9 Schlieren images of flow through the conical nozzle at an interval of 0.000278 sec at  $NPR = 3$  (Experimental)

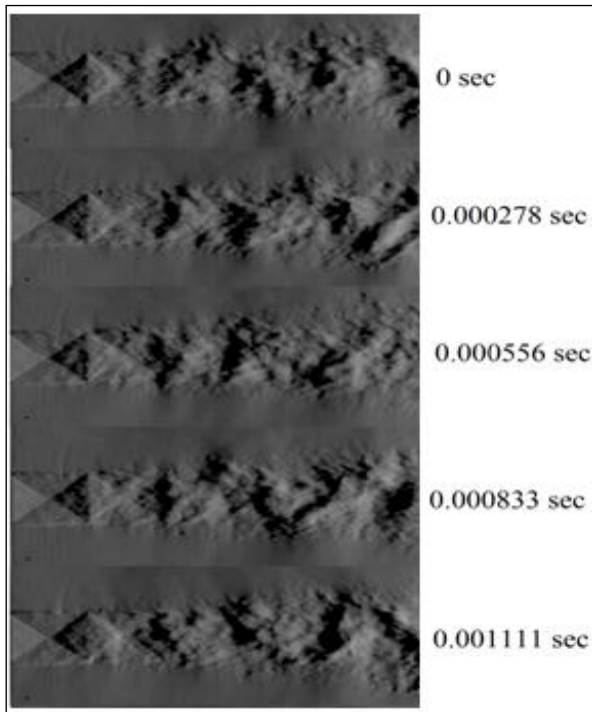


Fig. 6.10 Schlieren images of flow through the conical nozzle at an interval of 0.000278 sec at  $NPR = 3.7$  (Experimental)

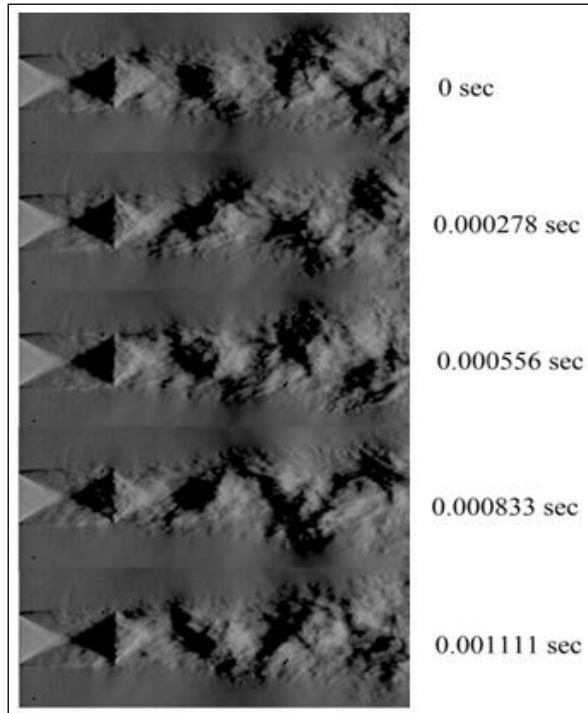


Fig. 6.11 Schlieren images of flow through the conical nozzle at an interval of 0.000278 sec at  $NPR = 4.5$  (Experimental)

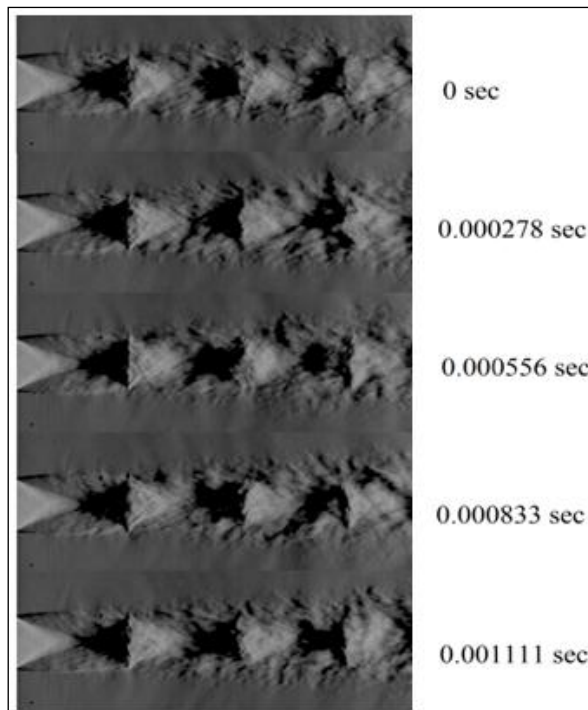


Fig. 6.12 Schlieren images of flow through the conical nozzle at an interval of 0.000278 sec at  $NPR = 5$  (Experimental)



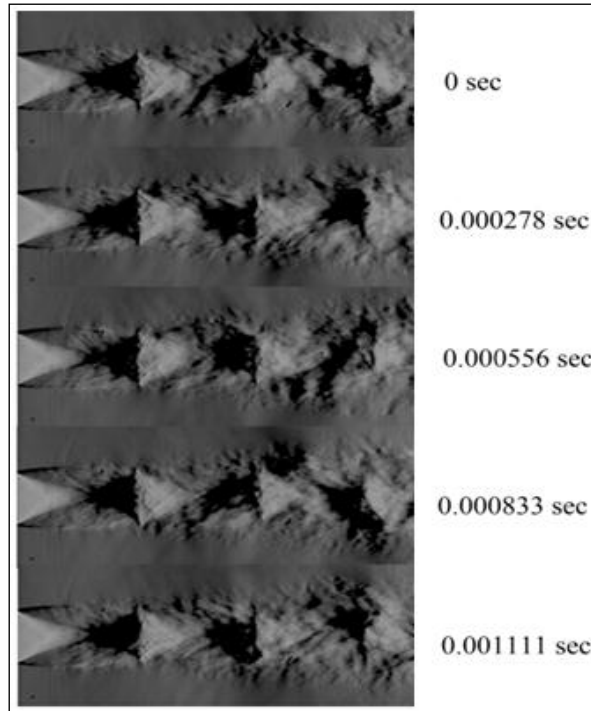


Fig. 6.13 Schlieren images of flow through the conical nozzle at an interval of 0.000278 sec at  $NPR = 5.5$  (Experimental)

Figure 6.11 - 6.13 represent flow at underexpanded conditions. Here the nozzle exit pressure is greater than atmospheric pressure and hence expansion waves are created from the nozzle exit to the jet boundary at ambient pressure. Due to the state of constant pressure at the jet boundary, it bent back to the flow axis as expansion waves. Again compression waves are formed at the intersection of jet boundary and expansion waves creating a series of shock cells. As shown in Figure 6.11, these intercepting shock waves congregate at the axis and a diamond configuration is formed. As the  $NPR$  increases, a normal shock wave or Mach disk is formed (Figure 6.13). The whole process is repeated and a series of shock cells formed continuously until the viscous effects become predominant.

From the figures taken at small time intervals, it is clear that the shock is unsteady with axisymmetric and helical oscillations. The darker regions in the flow field represent compression zone and brighter ones represent expansion zones. The displacement and distortion gradually increase for the shocks formed in the flow direction. The first shock is almost stationary. Schlieren images show that there is bobbing motion and associated deformation of the triangular shape of second and third shocks. These bobbing motion and deformation are two-dimensional impressions of helical oscillation. A shock splitting (second and third shock) is also seen in the images and this is due to the shock-turbulence interaction. Again, oscillation amplitude increases progressively in the flow direction. The main reason for shock oscillation is the periodic pressure perturbation from passing sound waves. The other reasons of shock oscillations are pairing between the motion of each shock, fluctuations of pressure linked with the way of the big organised structure along the shear layer of jet and the distortion of the subsonic-supersonic boundary in the shear layer of jet caused by the same organised vortices (Panda, 1998).

## **6.2 NUMERICAL PROCEDURE & ANALYSIS**

*ANSYS CFD Academic Version 16.0* with unlimited nodes was used to obtain the numerical solutions of turbulent compressible supersonic jets incorporating *SST  $k-\omega$*  turbulence model.

### **6.2.1 Governing Equations**

The governing equations used are Favre averaged continuity equation, momentum equation, energy equation and two transport equations for  $k$  and  $\omega$ . Boussinesq

approximation has been used to resolve the closure problem by replacing the velocity fluctuations with the gradient of mean velocities. The Reynolds stresses were determined by this approximation.

Continuity equation

$$\frac{\partial \bar{\rho}}{\partial t} + \text{div}(\bar{\rho} \tilde{U}) = 0 \quad (6.1)$$

Momentum Equations

$$\frac{\partial(\bar{\rho} \tilde{U})}{\partial t} + \text{div}(\bar{\rho} \tilde{U} \tilde{U}) = -\frac{\partial \bar{p}}{\partial x} + \text{div}(\mu \text{grad} \tilde{U}) + \left[ -\frac{\partial(\overline{\rho u'^2})}{\partial x} - \frac{\partial(\overline{\rho u'v'})}{\partial y} \right] + S_{M_x} \quad (6.2)$$

$$\frac{\partial(\bar{\rho} \tilde{v})}{\partial t} + \text{div}(\bar{\rho} \tilde{V} \tilde{U}) = -\frac{\partial \bar{p}}{\partial y} + \text{div}(\mu \text{grad} \tilde{V}) + \left[ -\frac{\partial(\overline{\rho u'v'})}{\partial x} - \frac{\partial(\overline{\rho v'^2})}{\partial y} \right] + S_{M_y} \quad (6.3)$$

Energy equation

$$\frac{\partial(\bar{\rho} \tilde{e})}{\partial t} + \text{div}(\bar{\rho} \tilde{e} \tilde{U}) = -\bar{p} \text{div} \tilde{U} + \text{div}(k \text{grad} T) + \phi + S_e \quad (6.4)$$

Transport equation for  $k$

$$\frac{\partial(\rho k)}{\partial t} + \text{div}(\rho k U) = \text{div} \left[ \left( \mu + \frac{\mu_t}{\sigma_k} \right) \text{grad}(k) \right] + p_k - \beta^* \rho k \omega \quad (6.5)$$

Transport equation for  $\omega$

$$\frac{\partial(\rho\omega)}{\partial t} + \text{div}(\rho\omega U) = \text{div}\left[\left(\mu + \frac{\mu_t}{\sigma_{\omega,1}}\right)\text{grad}(\omega)\right] + \gamma_2\left(2\rho S_{ij} \cdot S_{ij} - \frac{2}{3}\rho\omega\frac{\partial U_i}{\partial x_j}\delta_{ij}\right) - \beta_2\rho\omega^2 + 2\frac{\rho}{\sigma_{\omega,2}}\frac{\partial k}{\partial x_k}\frac{\partial \omega}{\partial x_k}$$

(6.6)

$$-\rho\overline{u'_i u'_j} = \mu_t\left(\frac{\partial u_i}{\partial x_j} + \frac{\partial u_j}{\partial x_i}\right) - \frac{2}{3}\rho k\delta_{ij}$$

(6.7)

### 6.2.2 Geometry and Boundary Conditions

After analyzing the potential core and shear layer length obtained from experiments, a two-dimensional computational domain was chosen with a domain length of  $30D_t$  downstream of the nozzle exit and a domain height of  $5D_t$  normal to the jet axis, where  $D_t$  is the nozzle throat diameter. A 2D computational domain with the assigned boundary types and boundary condition is shown in Figure 6.14.

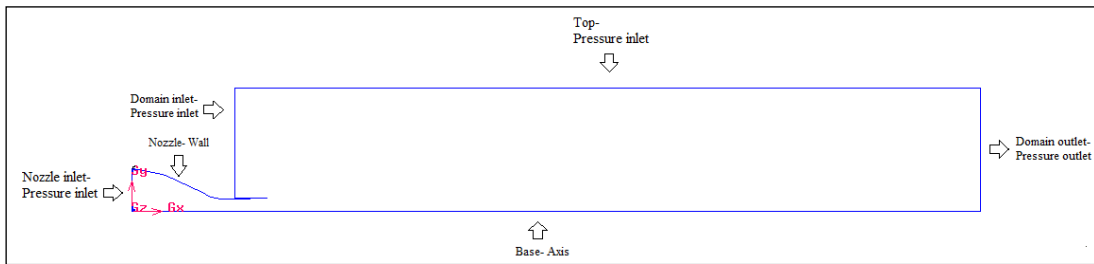


Fig. 6.14 Computational domain with boundary conditions

The nozzle inlet has been defined with a boundary type 'pressure inlet' and the gauge total pressure, supersonic/initial gauge pressure and total temperature were specified. The domain inlet has also been taken as 'pressure inlet' and the gauge total pressure,

supersonic/initial gauge pressure and total temperature have been specified as ambient conditions. The domain outlet was taken as 'pressure outlet' and the gauge pressure and total pressure were set to ambient. The bottom boundary has been specified as 'axis' as the domain is axi-symmetric. The boundary and operating conditions when the nozzle is operated at design conditions are shown in Table 6.1.

Table 6.1: Boundary and operating conditions when the nozzle is operated at design conditions

Domain	Boundary condition	Absolute pressure (Pa)	Turbulent intensity
Nozzle inlet	Pressure inlet	372518	5%
Domain inlet	Pressure inlet	101325	5%
Top inlet	Pressure inlet	101325	5%
Domain outlet	Pressure outlet	101325	5%
Base	Axis	-	-
Nozzle wall	Wall	-	-

### 6.2.3 Discretisation and Grid Independence Study

A multi-block strategy was used for the construction of grid. The closer view of the computational grid for the nozzle exit is shown in Figure 6.15 (a), while the entire computational grid is shown in Figure 6.15 (b).

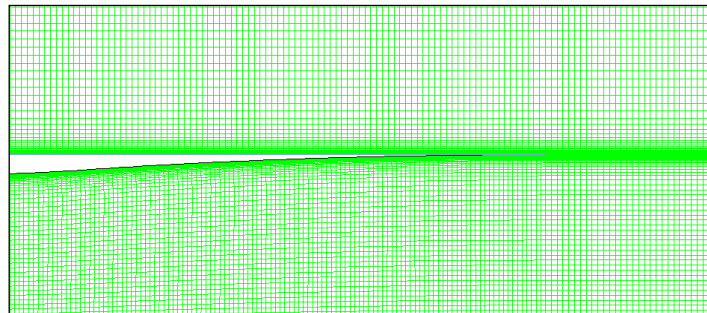


Fig. 6.15 (a) Computational grid at the nozzle exit

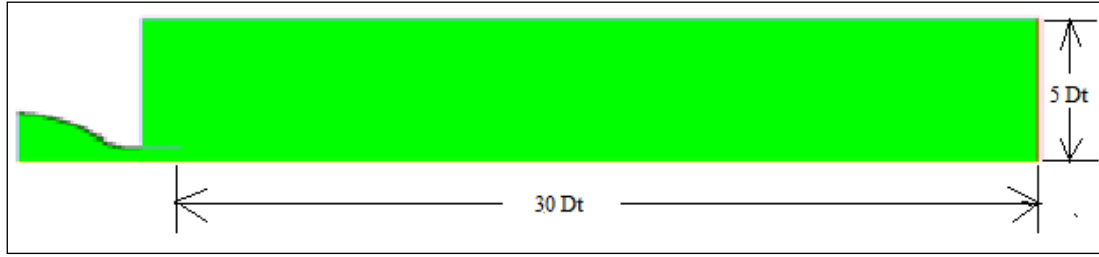


Fig. 6.15 (b) Total computational grid

The first boundary layer mesh near the wall was created in such a way that a wall  $y^+$  value of less than one was generated. In the present work, a grid independence study was carried out for mesh sizes of (196 x 56), (273 x 64) and (409 x 77) in the nozzle core region which generates a computational grid size of 0.11, 0.19 and 0.33 million cells respectively for the full domain. The ratio of the total number of grids for two consecutive models in the present simulation was 1.67 and 1.74. Schomberg *et al.* (2015) conducted a similar grid independence study in their numerical work and reported a grid ratio for two consecutive computational domains as 1.753 and 1.739. The present calculations have also been carried out directly on a more refined mesh, especially in the regions of the nozzle wall, shear layer, and exit. Mesh refinement near the no-slip surfaces is such that the area weighted wall  $y^+$  for all the cases is less than 1. The size of the cells along the shear layer where intense mixing takes place varies from 0.05 mm to 1.0 mm. The minimum orthogonal quality of quadrilateral cell was 0.78 with a maximum skewness of 0.22. Furthermore, second-order accurate discretisation has been used for all the variables and calculations were carried out till the residuals for all the equations were less than  $10^{-6}$ .

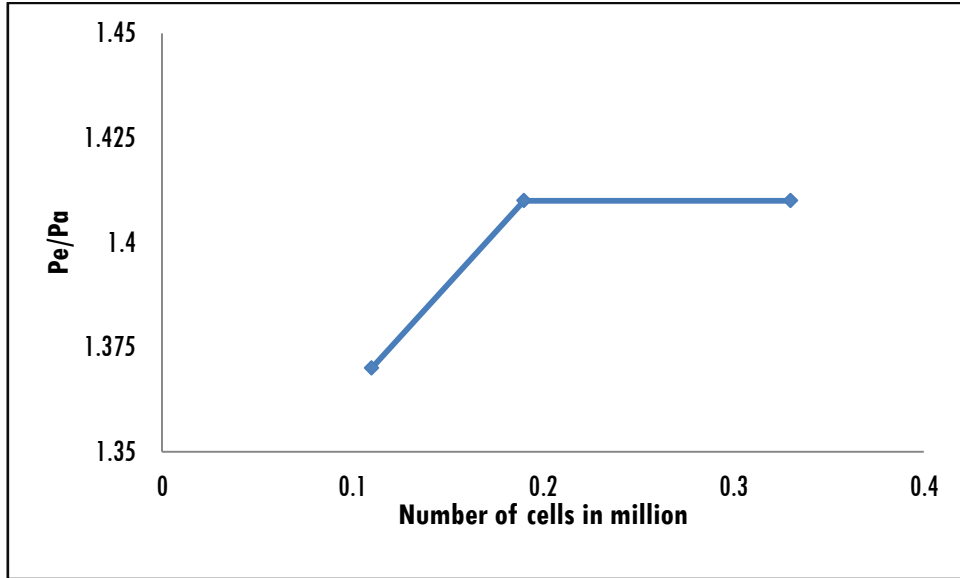


Fig. 6.16 Variation in nozzle exit pressure with grid size for the double parabolic nozzle with  $PM/3$  profile at  $NPR = 5$

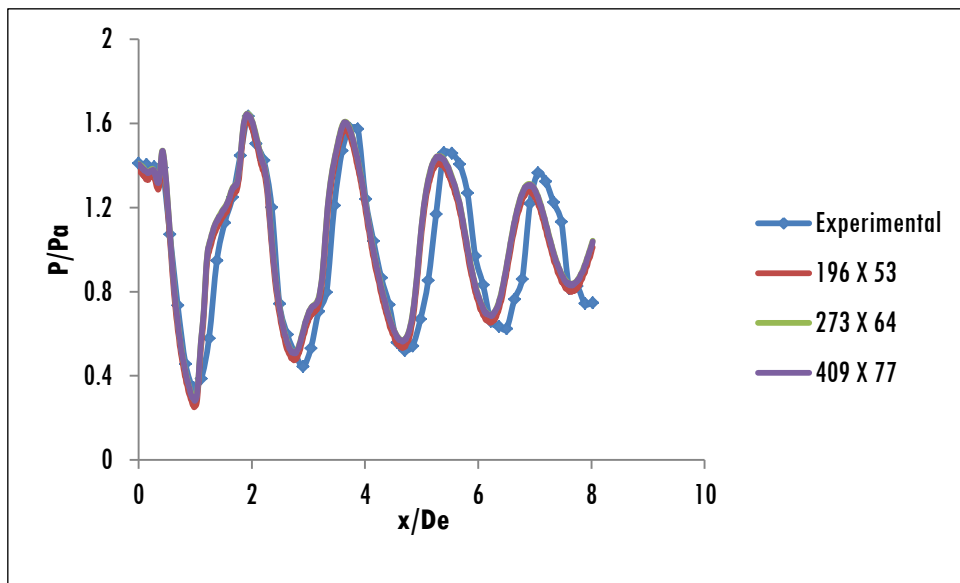


Fig. 6.17 Grid independence study on the nozzle core region of the double parabolic nozzle with  $PM/3$  profile at  $NPR = 5$

The variation in pressure ( $P_e/P_a$ ) at nozzle exit ( $x/D_e = 0$ ) is illustrated for grid size of 0.11, 0.19 and 0.33 million cells in Figure 6.16 where  $P_e$  is the nozzle exit pressure and  $P_a$  is the ambient pressure. It was observed that the variation in properties was

less than 1% for cell count greater than 0.2 million cells. Figure 6.17 shows the comparison between the static pressure predictions along the axis, especially in the nozzle core region for different mesh sizes (196 x 53, 273 x 64, 409 x 77) with the measured experimental data. The comparison showed that the deviations in properties obtained from 0.19 million and 0.33 million cells were less than 1% and hence all further numerical simulations were carried out on a grid size of 0.19 million cells for the full domain. The experimental measurements were also seen to be in good agreement with the numerical predictions.

An implicit formulation with the second-order accurate upwind scheme is used for all the flow variables, turbulent kinetic energy, and specific dissipation rate. The net mass balance in the entire computational domain was less than 0.25% of the inflow. The *CFD* simulations were run for convergence until the residuals of mass, momentum, energy, turbulent kinetic energy, specific dissipation rate etc. were less than  $10^{-6}$ .

### **6.3 NOZZLE FLOW CHARACTERISTICS**

Numerical predictions of flow emanating from different nozzle configurations at design conditions are compared with the experimental data measured for nozzle pressure ratio of 3.7 and 5. Figure 6.18 predicts the free stream static pressure and Figure 6.19 predicts the Mach numbers of (a) Conical, (b) Bell, and (c) Double parabolic nozzles respectively at  $NPR = 3.7$ .



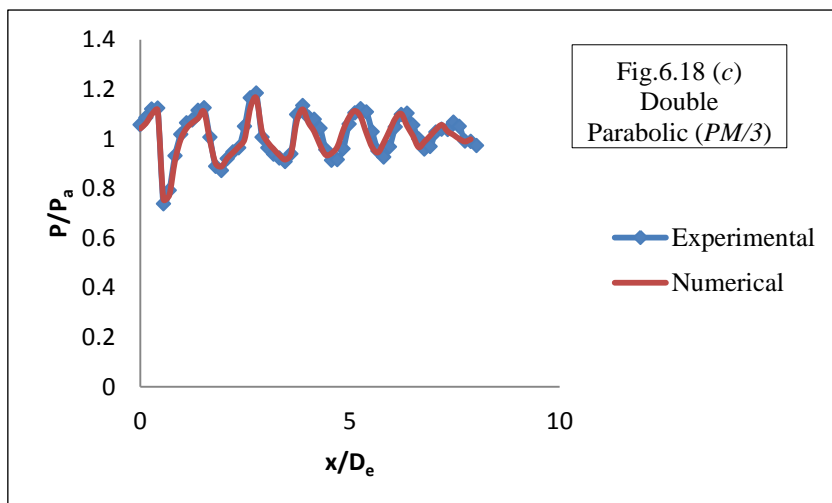
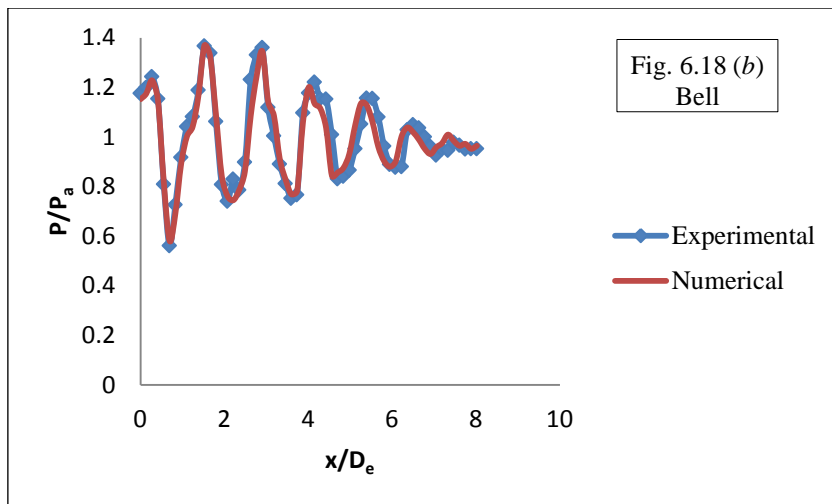
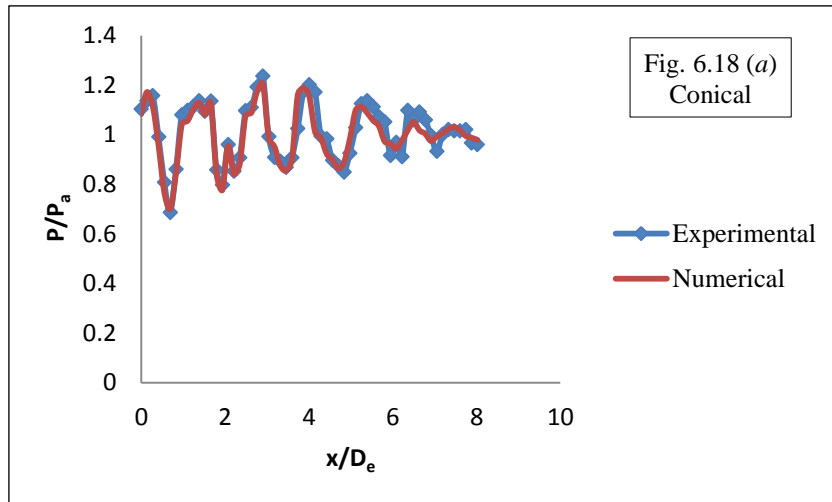


Fig. 6.18 Comparison of experimental data and numerical predictions of pressure variation along the jet axis of different nozzles at  $NPR = 3.7$  (a) Conical (b) Bell (c) Double parabolic ( $PM/3$ )

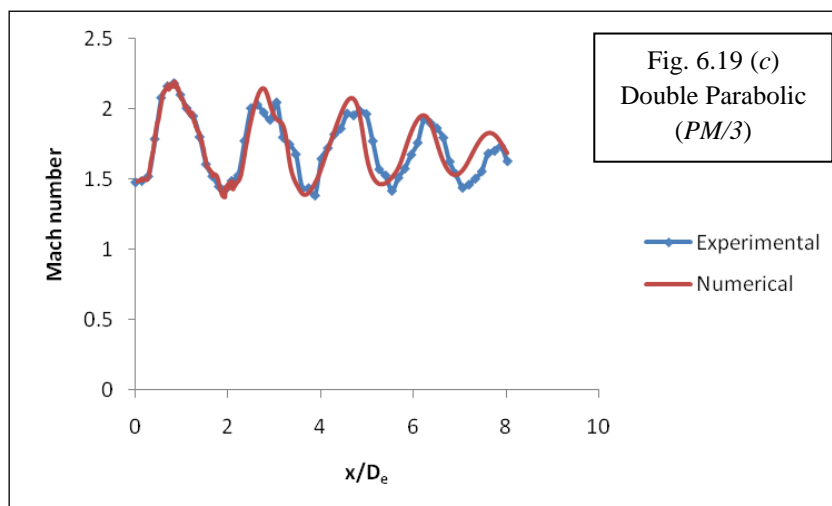
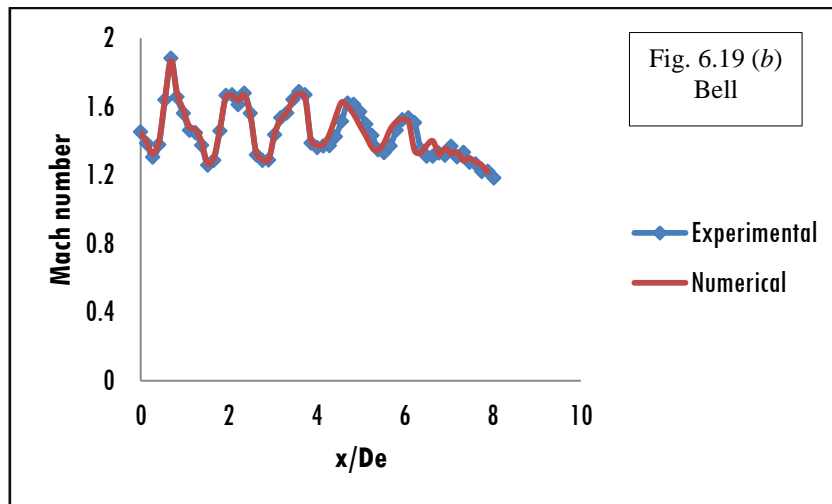
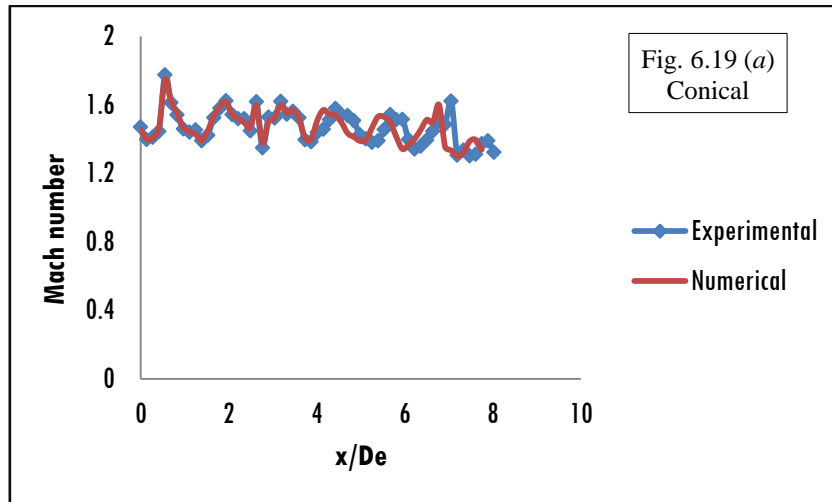


Fig. 6.19 Comparison of experimental data and numerical predictions of Mach number variation along the jet axis of different nozzles at  $NPR = 3.7$  (a) Conical (b) Bell (c) Double parabolic (PM/3)

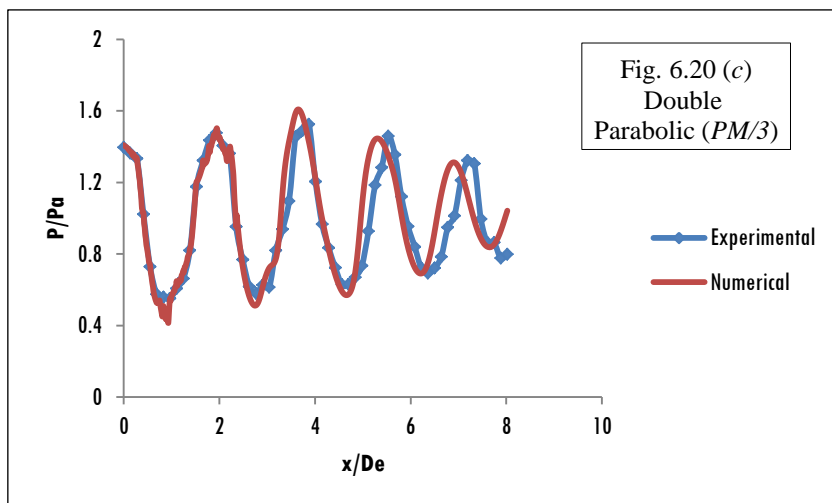
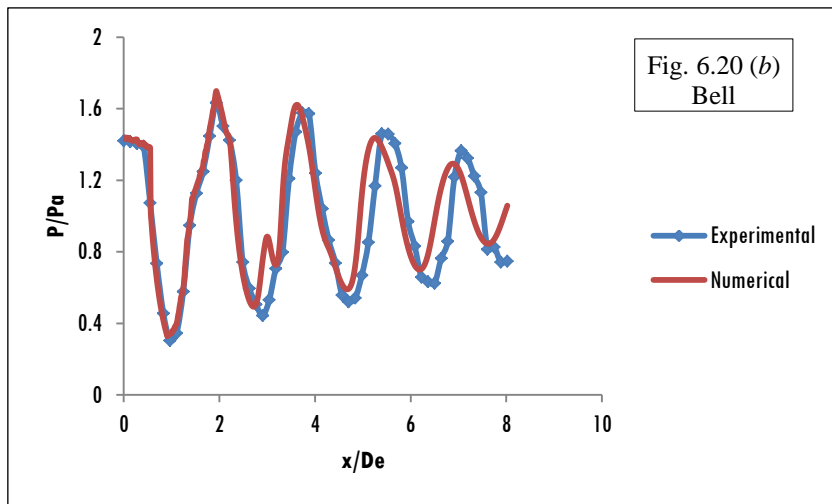
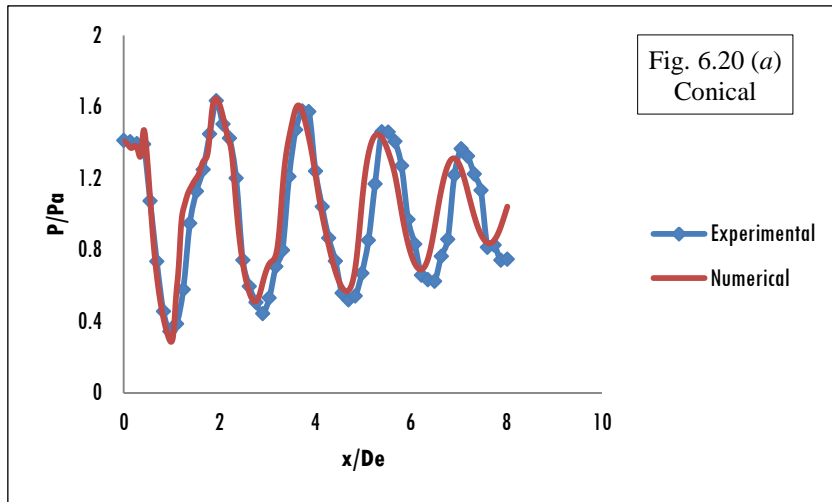


Fig. 6.20 Comparison of experimental data and numerical predictions of pressure variation along the jet axis of different nozzles at  $NPR = 5$  (a) Conical (b) Bell (c) Double parabolic ( $PM/3$ )

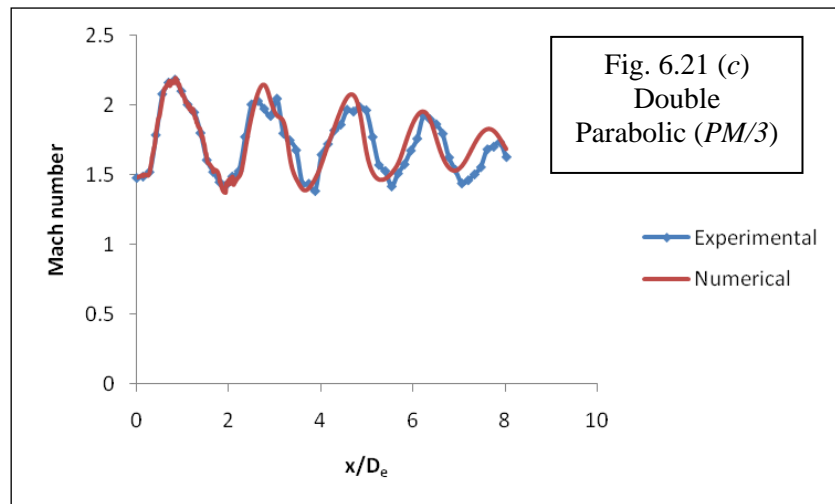
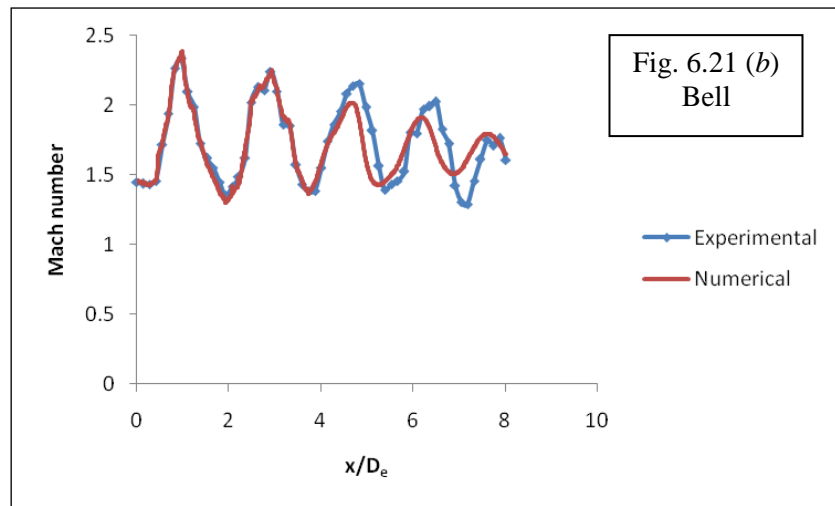
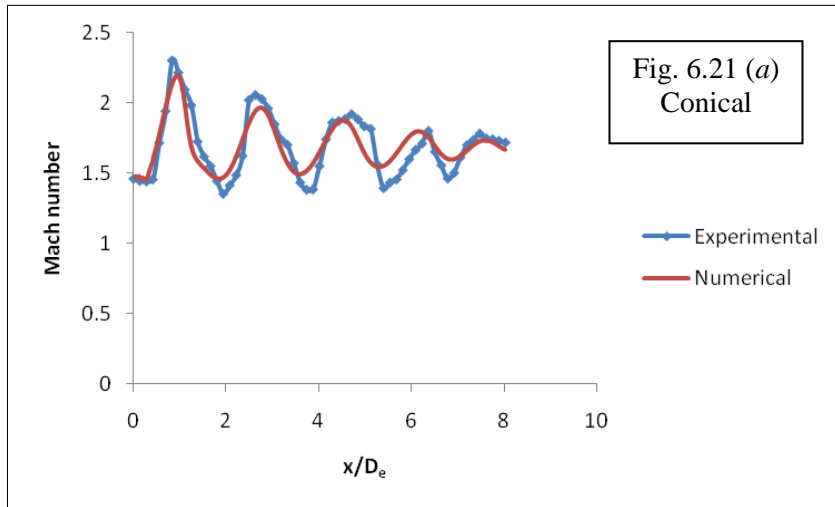


Fig. 6.21 Comparison of experimental data and numerical predictions of Mach number variation along the jet axis of different nozzles at  $NPR = 5$  (a) Conical (b) Bell (c) Double parabolic ( $PM/3$ )

Figures 6.20 (a), (b), and (c) show the comparison of free stream static pressure from nozzle exit to  $8D_e$  of conical, bell, and double parabolic nozzles respectively at  $NPR=5$ . It is evident from the figures that the solution is accurate as it predicts the first four shock cell positions and corresponding pressure amplitudes reasonably well. In the case of bell nozzle, there is a slight under-prediction of shock cell position. However, the presence of double barrel shock is clearly observed. Figures 6.21 (a), (b), and (c) show the comparison of Mach number with experimental data for conical, bell and double parabolic nozzles respectively. It is also observed that the solution matches well with experimental data up to an axial distance of  $7D_e$ . The centreline pressure and Mach number variations decrease along with the nozzle axis and this is due to the supersonic jet mixing entrainment. The percentage of deviation between experimental and numerical results of centreline pressure and Mach number along nozzle axis upto a distance of 5 times the nozzle exit diameter is less than 1.5% for conical, bell, and  $PM/3$  double parabolic nozzle at design conditions. However, at underexpanded condition beyond  $5D_e$  from nozzle exit, the deviation is close to 5% and this is due to the oscillation of shock cells at high  $NPRs$ .

#### **6.4 NOZZLE PERFORMANCE PARAMETERS**

In this section, the flow characteristics and nozzle performance of conical, bell, and double parabolic are compared.

### 6.4.1 Shock Cell Length

Shock cell length is the distance from one shock crossing point to the next (Rathakrishnan E., 2010). It is revealed both experimentally and numerically that the static pressure and Mach number vary in an oscillating manner along the jet axis due to the shock cell formation. The shock cell patterns are captured by Schlieren photography. Pitot pressure and Schlieren image comparison of the double parabolic nozzle at  $NPR$  5 is shown in Figure 6.22.

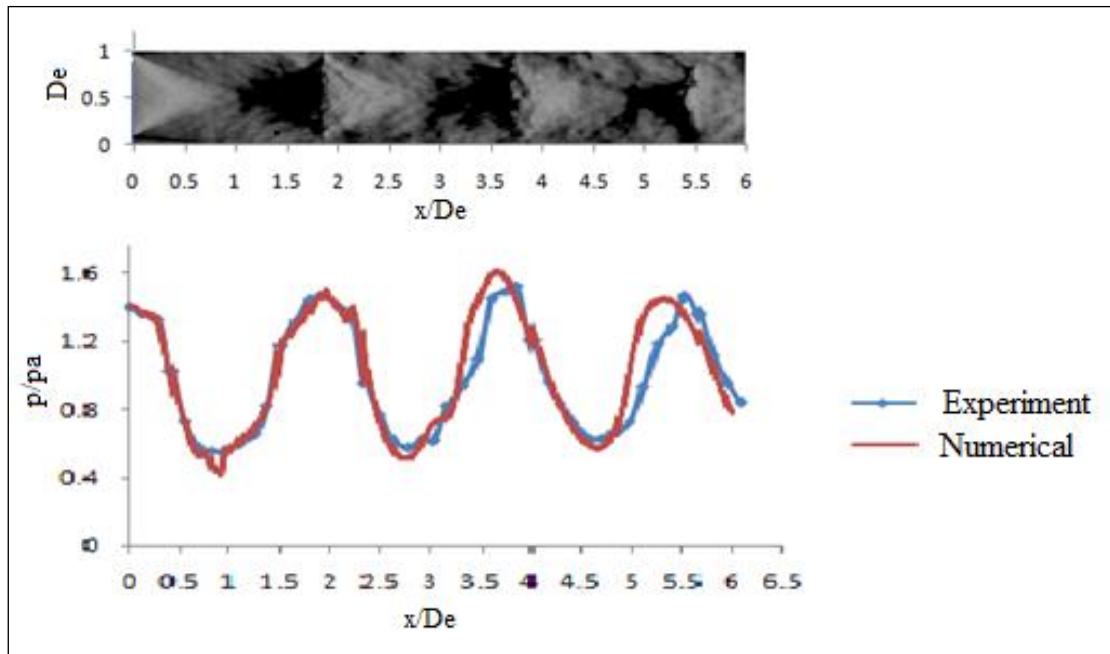


Fig. 6.22 Pitot pressure and Schlieren image comparison for the double parabolic nozzle with  $PM/3$  profile at  $NPR=5$

The simulated shock positions agree well with the experimental visualisation. A low-pressure zone is obtained at the end of the expansion region and a high-pressure zone is obtained at the end of the compression region. Computational predictions and experimental data obtained from Pitot pressure measurements and Schlieren images show the same trend.

Shock cell length of conical, bell, and  $PM/3$  double parabolic nozzles at different  $NPR$ s were measured from Schlieren images. The shock cell lengths may also be predicted by different equations developed by earlier researchers. Pack (1950) developed Equation 6.8 for predicting shock cell length.

$$\lambda = 1.306D_j(\sqrt{M^2 - 1}) \quad (6.8)$$

Shock cell lengths were also predicted by Equation 6.9 developed by Mehta and Prasad (1996).

$$\frac{\lambda}{d^*} = 0.3(M_e + 1)\beta^2 - (2.75M_e - 5.2) \quad (6.9)$$

where  $\beta^2$  is defined as 
$$\frac{2}{\gamma - 1} \left( \frac{P_0}{P_a} \right)^{\frac{\gamma - 1}{\gamma}} - \left( \frac{\gamma + 1}{\gamma - 1} \right)$$

Figures 6.23, 6.24 and 6.25 demonstrate the variations of shock cell lengths at different  $NPR$ s for conical, bell, and  $PM/3$  double parabolic nozzles respectively. The Figures demonstrates that the nozzle contour has not much influence on shock cell length. Table 6.2 shows a comparison of shock cell lengths for different  $NPR$ s by analysing the Schlieren images obtained experimentally and also from the equations developed by earlier researchers. From the table, it is clear that the shock cell length increases with increasing  $NPR$ s and the equation developed by Mehta and Prasad predicts the shock cell length better. The prediction by Pack relation gives a lesser value than actual.

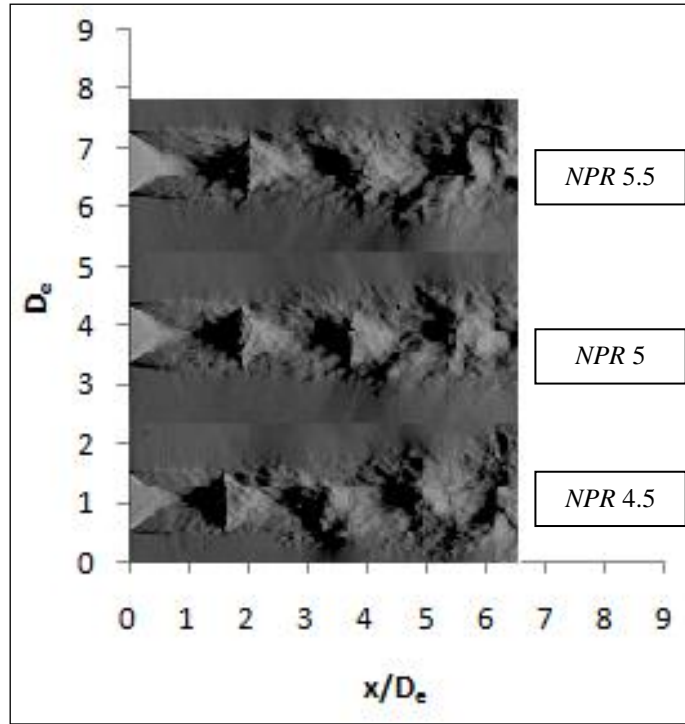


Fig. 6.23 Comparison of Schlieren images of the conical nozzle at *NPRs* of 4.5, 5, and 5.5 (Experimental)

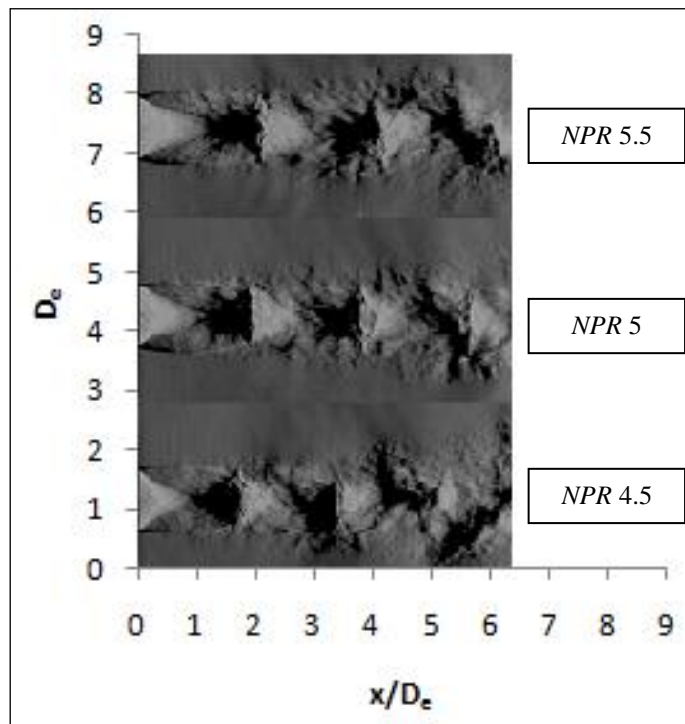


Fig. 6.24 Comparison of Schlieren images of the bell nozzle at *NPRs* of 4.5, 5, and 5.5 (Experimental)



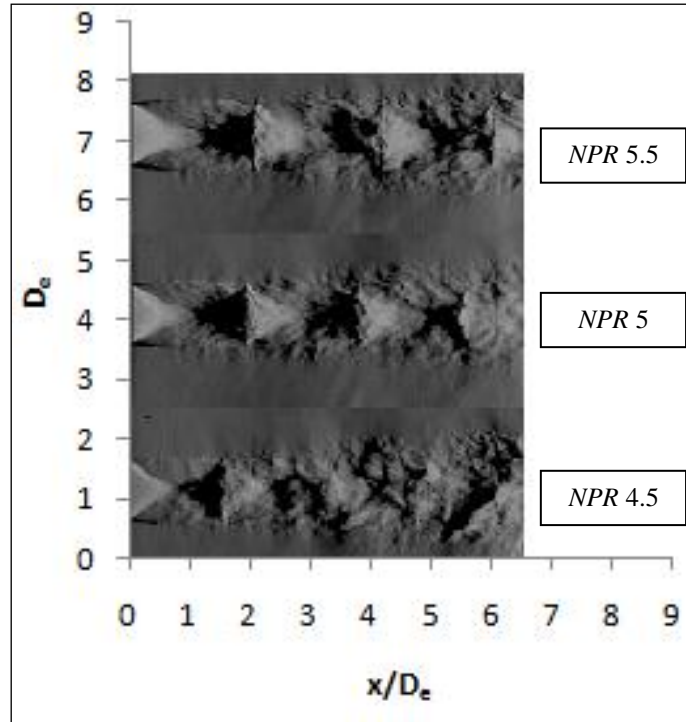


Fig. 6.25 Comparison of Schlieren images of the double parabolic nozzle with *PM/3* profile at *NPRs* of 4.5, 5, and 5.5 (Experimental)

Table 6.2: Variation of shock cell lengths of conical, bell, and *PM/3* double parabolic nozzles at *NPRs* 4.5, 5, and 5.5

Nozzle	<i>NPR</i>	Shock cell length by		
		Schlieren image	Pack relation	Mehta and Prasad relation
Conical	4.5	$1.85 D_e$	$1.70 D_e$	$1.87 D_e$
	5	$1.92 D_e$	$1.81 D_e$	$1.90 D_e$
	5.5	$1.97 D_e$	$1.91 D_e$	$1.95 D_e$
Bell	4.5	$1.85 D_e$	$1.70 D_e$	$1.87 D_e$
	5	$1.93 D_e$	$1.81 D_e$	$1.90 D_e$
	5.5	$1.98 D_e$	$1.91 D_e$	$1.95 D_e$
Double Parabolic ( <i>PM/3</i> )	4.5	$1.83 D_e$	$1.70 D_e$	$1.87 D_e$
	5	$1.90 D_e$	$1.81 D_e$	$1.90 D_e$
	5.5	$1.95 D_e$	$1.91 D_e$	$1.95 D_e$

### 6.4.2 Shock Wave Angle

Shock wave angle is calculated by analysing Schlieren images with an image processing code. Table 6.3 shows the variation of shock wave angle of conical, bell, and double parabolic nozzle with  $PM/3$  profile at different  $NPR$ s. It is observed that shock angle increases with increasing  $NPR$ . Double parabolic nozzle with  $PM/3$  profile has a lesser value of shock angle (weak oblique shocks) than that of conical and bell nozzles.

Table 6.3: Variation of shock wave angle of conical, bell, and double parabolic nozzle with  $PM/3$  profile at  $NPR$ s of 4.5, 5, and 5.5

Nozzle	$NPR$	Shock angle
Conical	4.5	27.60 <sup>0</sup>
	5	29.60 <sup>0</sup>
	5.5	32.20 <sup>0</sup>
Bell	4.5	28.00 <sup>0</sup>
	5	30.10 <sup>0</sup>
	5.5	32.50 <sup>0</sup>
Double parabolic ( $PM/3$ )	4.5	27.25 <sup>0</sup>
	5	29.25 <sup>0</sup>
	5.5	31.90 <sup>0</sup>

### 6.4.3 Shock Cell Count

Figure 6.26 shows that there is negligible influence on the profile of nozzle configuration on shock cell count. Conical and bell nozzle show a sudden change in velocity indicating the presence of stronger shock along the downstream than that of double parabolic. Figures 6.27 and 6.28 show the pressure and density contours obtained numerically for double parabolic nozzle at different  $NPR$ s. It is observed from the figures that the shock cell count increases with increase in  $NPR$ s. Shock cell count for all nozzle configurations at  $NPR$ s 4.5, 5, and 5.5 are 4, 5, and 6 respectively.

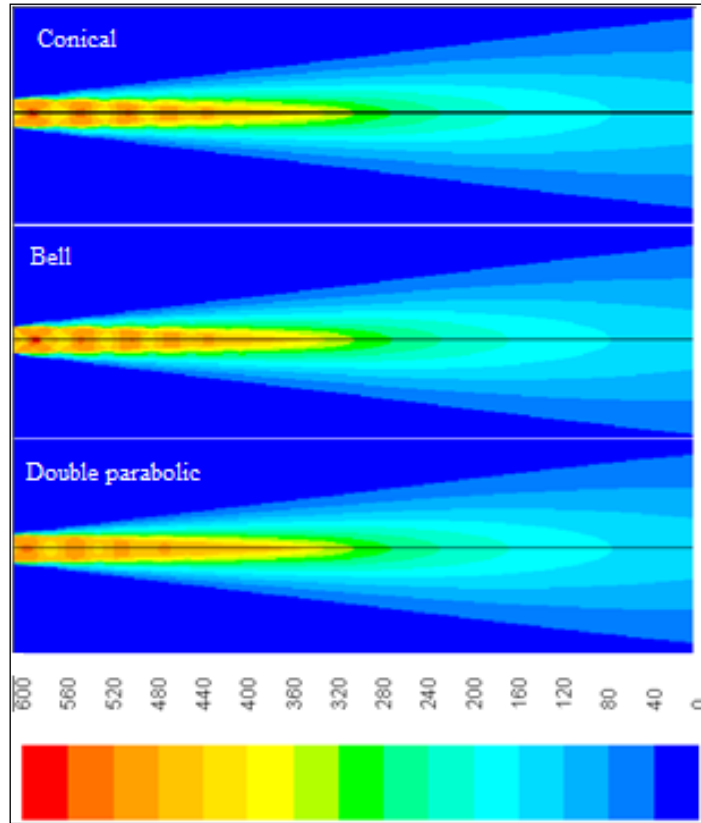


Fig. 6.26 Velocity contours (m/s) of conical, bell, and the double parabolic nozzle with  $PM/3$  profile at  $NPR = 5$  (Numerical)

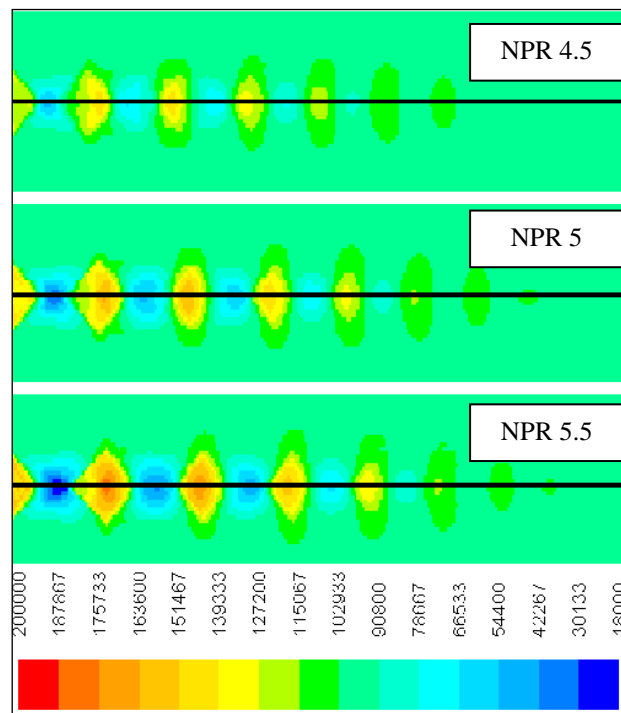


Fig. 6.27 Pressure contours (Pa) of the double parabolic nozzle with  $PM/3$  profile at  $NPRs$  of 4.5, 5, and 5.5 (Numerical)

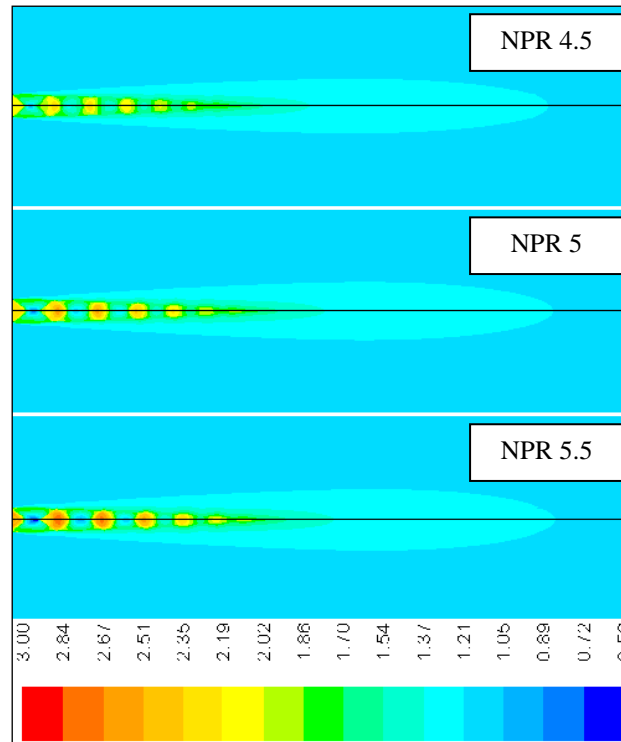


Fig. 6.28 Density contours ( $\text{kg/m}^3$ ) of the double parabolic nozzle with  $PM/3$  profile at  $NPR$ s of 4.5, 5, and 5.5 (Numerical)

#### 6.4.4 Potential Core Length

Potential core length is defined as the distance over which the centre line velocity remains at least 95% of mean axial velocity. Figures 6.29 shows the variation of the ratio of centreline velocity to mean centreline velocity along the jet axis of double parabolic nozzles at  $NPR$  4.5, 5 and 5.5 respectively obtained from numerical simulations. The potential core length for  $NPR$  4.5 is  $9.80D_e$ ,  $NPR$  5 is  $10.35D_e$  and  $NPR$  5.5 is  $10.57D_e$ . From these figures, it is observed that potential core increases with  $NPR$ . Figure 6.30 shows the variation of potential core length of the conical nozzle at different  $NPR$ s. From Figure 6.31 it is clear that the nozzle contour has negligible influence in the potential core region. Table 6.4 reveals the potential core length of the double parabolic nozzle is slightly lesser than that of conical and bell nozzle. The reduction in potential core length indicates better turbulent mixing along the downstream direction from the nozzle exit.

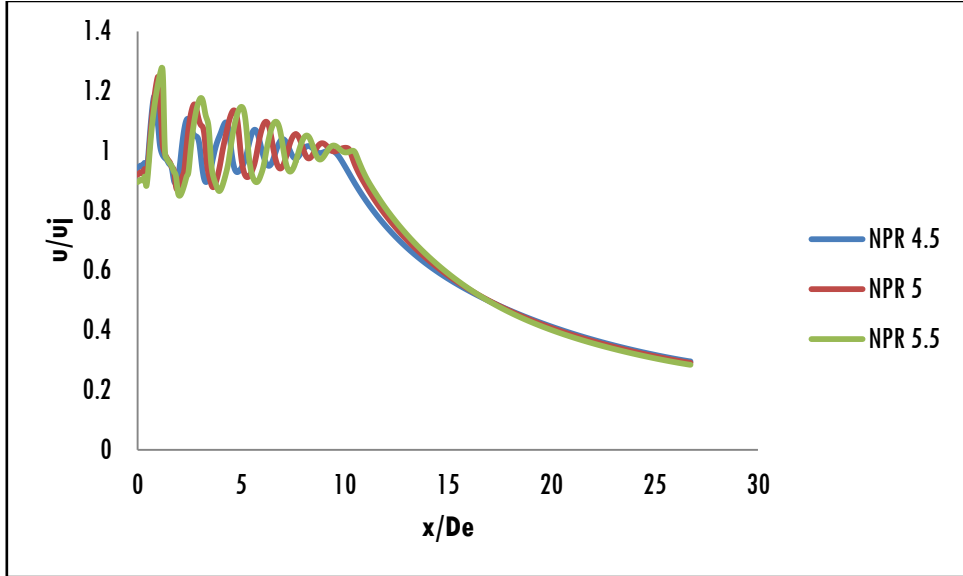


Fig. 6.29 Variation of  $u/u_j$  centreline of the double parabolic nozzle with  $PM/3$  profile along the jet axis at  $NPR = 4.5, 5,$  and  $5.5$

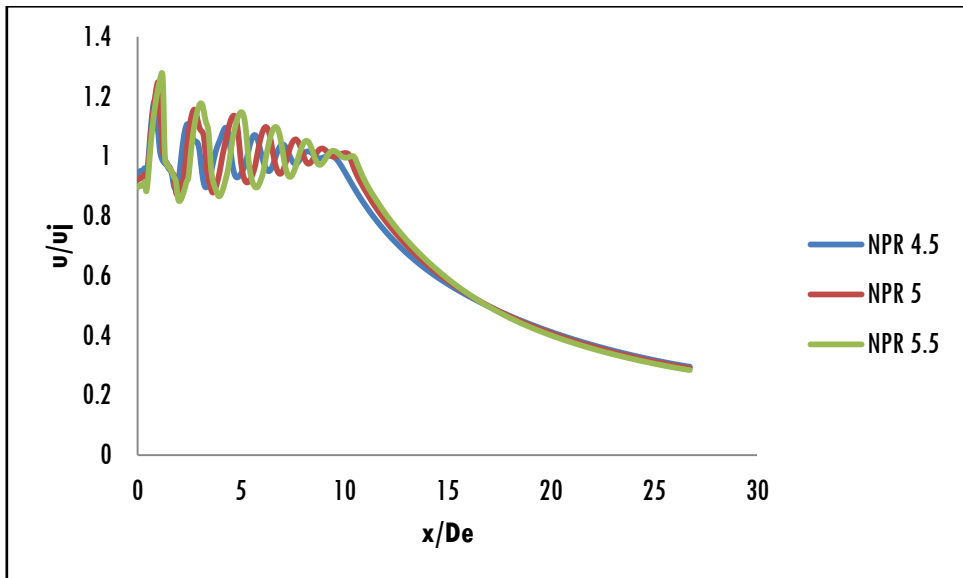


Fig. 6.30 Variation of  $u/u_j$  centreline of the conical nozzle along the jet axis at  $NPRs 4.5, 5,$  and  $5.5$

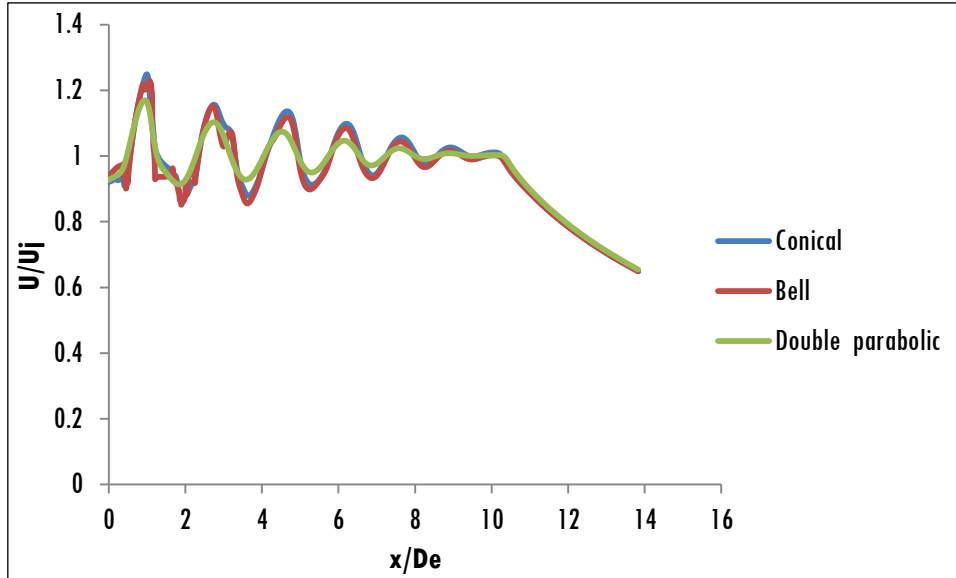


Fig. 6.31 Comparison of the mean axial velocity of different nozzles at  $NPR = 5$

Table 6.4: Potential core length of conical, bell, and the double parabolic nozzle with  $PM/3$  profile at  $NPRs$  4.5, 5, and 5.5

Nozzle	$NPR= 4.5$	$NPR= 5$	$NPR= 5.5$
Conical	9.90 $D_e$	10.41 $D_e$	10.64 $D_e$
Bell	9.92 $D_e$	10.44 $D_e$	10.66 $D_e$
Double parabolic( $PM/3$ )	9.80 $D_e$	10.35 $D_e$	10.57 $D_e$

### 6.4.5 Supersonic Core Length

The supersonic core length is the distance from the  $CD$  nozzle exit to the axial point from where the Mach number continuously decay from sonic. Figure 6.32 show the variation of the Mach number of the double parabolic nozzle with  $PM/3$  profile along the jet axis at  $NPRs$  4.5, 5, and 5.5 respectively. Figure 6.33 shows the variation of supersonic core length of the conical nozzle at different nozzle pressure ratios.

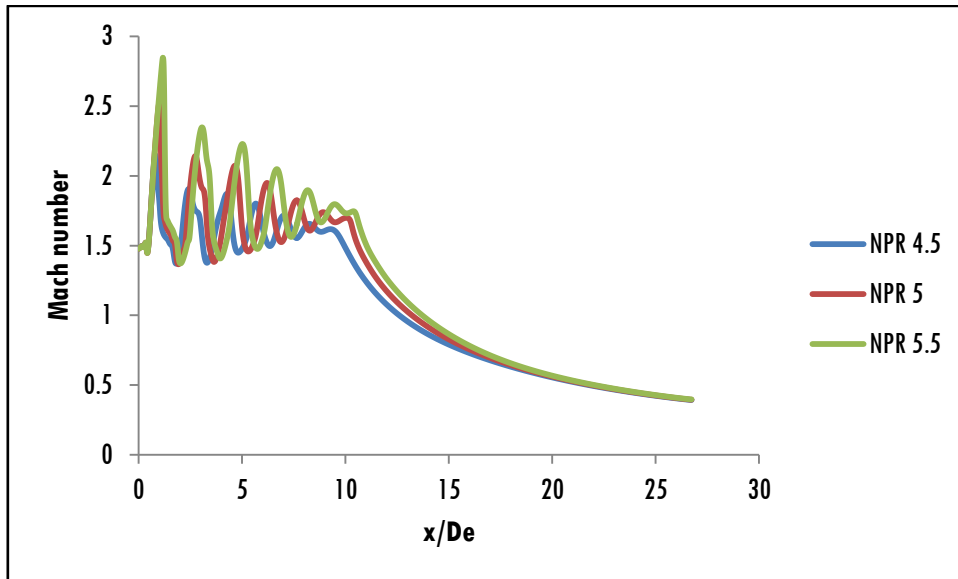


Fig. 6.32 Variation of centreline Mach number of the double parabolic nozzle with  $PM/3$  profile along the jet axis at  $NPR = 4.5, 5$  and  $5.5$

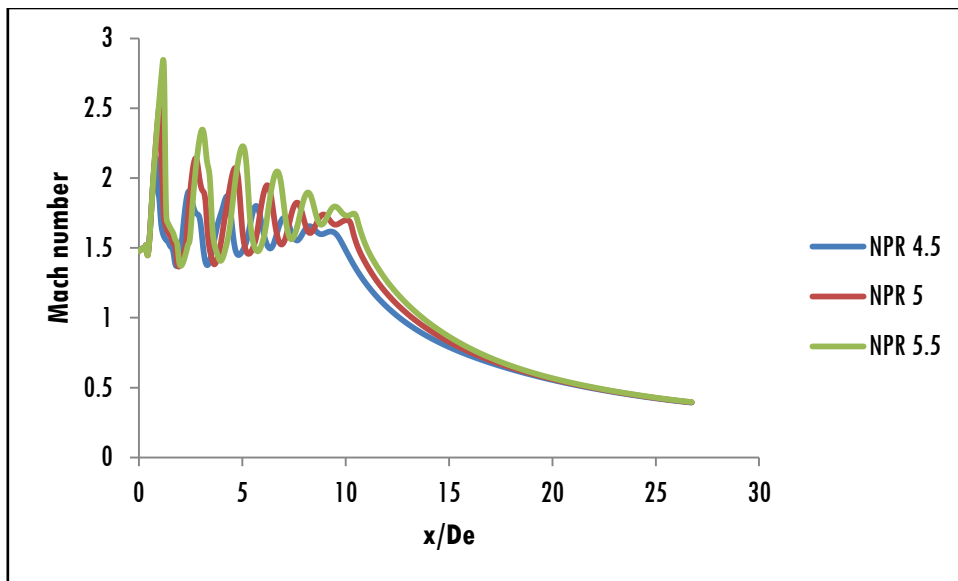


Fig. 6.33 Variation of centreline Mach number of the conical nozzle along the jet axis at  $NPRs$  4.5, 5, and 5.5

Supersonic core length is also found by the total pressure decay graphs as shown in Figure 6.34. The length is determined by measuring the distance from the nozzle exit to the point where the total pressure decay initiates. Figure 6.35 shows the variation of supersonic core length of the conical nozzle at different  $NPRs$ .

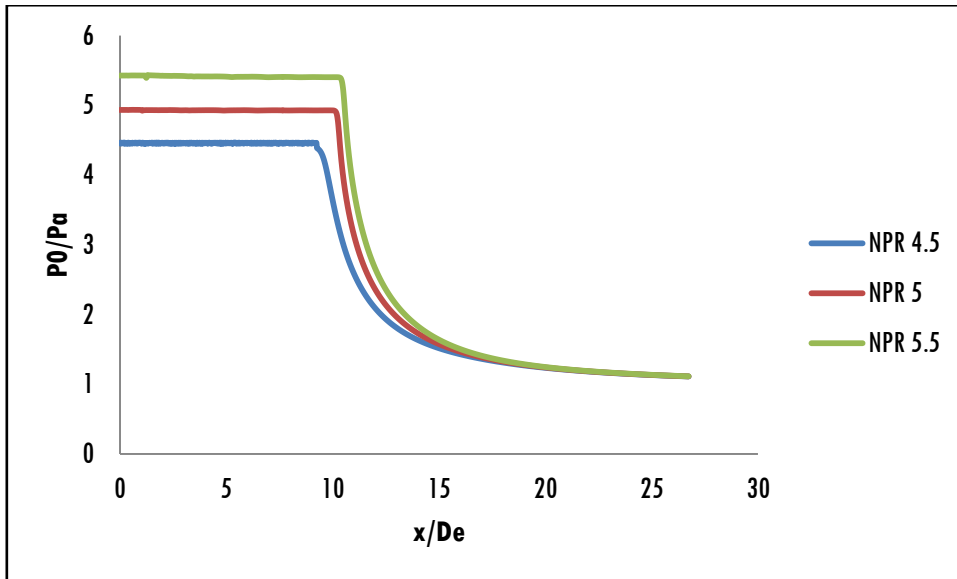


Fig. 6.34 Total pressure decay of the double parabolic nozzle with  $PM/3$  profile along the jet axis at  $NPR = 4.5, 5, \text{ and } 5.5$

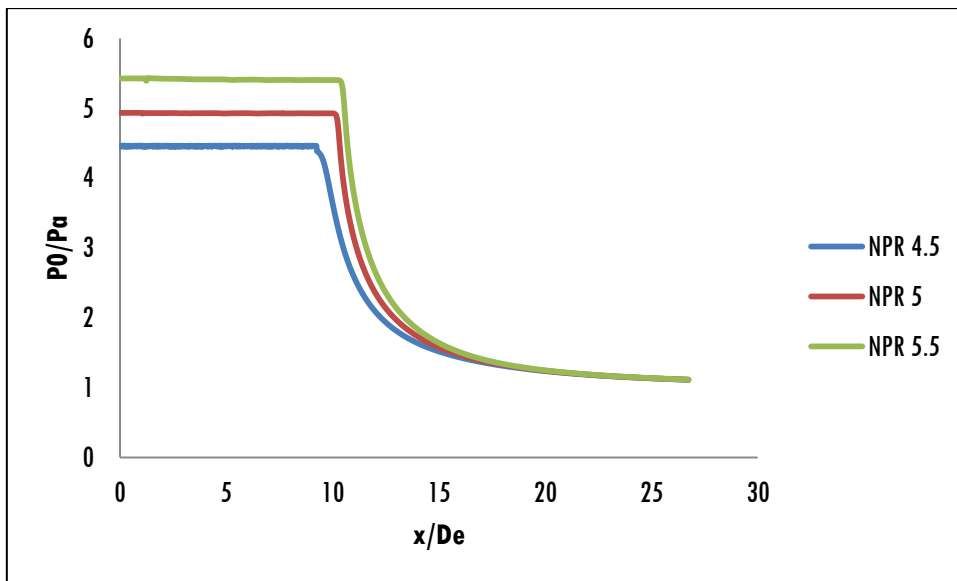


Fig. 6.35 Total pressure decay of conical nozzle along the jet axis at  $NPRs 4.5, 5 \text{ and } 5.5$



Table 6.5: Variation of supersonic core lengths of conical, bell and the double parabolic nozzle with  $PM/3$  profile at  $NPR$ s 4.5, 5, and 5.5

Nozzle	$NPR$	Mach number $V_{sx}/D_e$ graph	Supersonic core length by		
			Mach number decay method	Total pressure decay graph	Shirie and Seubold method
Conical	4.5	12.62 $D_e$	9.51 $D_e$	9.26 $D_e$	11.35 $D_e$
	5	13.23 $D_e$	10.20 $D_e$	10.01 $D_e$	12.55 $D_e$
	5.5	13.74 $D_e$	10.58 $D_e$	10.32 $D_e$	13.30 $D_e$
Bell	4.5	12.63 $D_e$	9.52 $D_e$	9.27 $D_e$	11.35 $D_e$
	5	13.24 $D_e$	10.21 $D_e$	10.02 $D_e$	12.55 $D_e$
	5.5	13.75 $D_e$	10.59 $D_e$	10.33 $D_e$	13.30 $D_e$
Double parabolic ( $PM/3$ )	4.5	12.60 $D_e$	9.50 $D_e$	9.25 $D_e$	11.35 $D_e$
	5	13.21 $D_e$	10.19 $D_e$	10.00 $D_e$	12.55 $D_e$
	5.5	13.72 $D_e$	10.56 $D_e$	10.30 $D_e$	13.30 $D_e$

Table 6.5 shows a comparison of supersonic core lengths for different  $NPR$ s from Mach number decay graph and also from the method developed by Shirie and Seubold (1967). The supersonic core length predicted from the above method was found to be larger than the actual value. The supersonic core length for all the three nozzles are almost the same indicating negligible influence for the profile of nozzle contours on core development.

#### 6.4.6 Nozzle Thrust

The amount of the thrust developed by the engine depends on the mass flow rate through the nozzle, the exit velocity of flow and the pressure at the nozzle exit.

For a jet propulsion device, if the nozzle exit pressure is greater than ambient, a positive contribution of thrust called pressure thrust will be developed in addition to momentum thrust. The total thrust can be obtained from Equation 6.10.

$$T = \int_0^R [\rho u^2 + (p - p_a)] r dr \quad (6.10)$$

Table 6.6: Thrust generation of conical, bell and the double parabolic nozzle with *PM/3* profile at *NPRs* 4.5, 5, and 5.5

Nozzle	<i>NPR</i>	Momentum Thrust (N)	Pressure Thrust (N)	Total Thrust (N)
Conical	4.5	139.01	8.96	147.97
	5	153.13	14.58	167.71
	5.5	165.77	20.7	186.47
Bell	4.5	138.95	8.74	147.69
	5	151.61	14.87	166.48
	5.5	165.25	20.62	185.87
Double parabolic ( <i>PM/3</i> )	4.5	140.92	8.55	149.47
	5	155.78	13.95	169.73
	5.5	167.72	20.27	187.99

Table 6.6 represents the comparison of thrusts for the three nozzle configurations at different *NPRs*. It is observed that the double parabolic nozzle generates higher thrust as compared to the other nozzle configurations. Mubarak and Tide (2018) have reported a thrust augmentation of the double parabolic nozzle as 1% and is persistent with the observations reported by Sternin (2000) for improved nozzle configurations.

#### 6.4.7 Nozzle Thrust Coefficient

Nozzle performance is evaluated by calculating the nozzle thrust coefficient by using Equation 6.11 reported by Spottset *al.* (2013).

$$C_f = \frac{\int_0^R (\rho u^2 + (p - p_a)) r dr}{u_{ideal} \int_0^R \rho u r dr} \quad (6.11)$$

In this equation, the subscript '*ideal*' refers to the quantity calculated for an ideal nozzle based on one-dimensional isentropic flow assumption.

Table 6.7: Variation of nozzle thrust coefficients of conical, bell, and the double parabolic nozzle with *PM/3* profile at *NPRs* 4.5, 5 and 5

Nozzle	<i>NPR</i>	Nozzle Thrust Coefficient
Conical	4.5	0.9861
	5	0.9844
	5.5	0.9733
Bell	4.5	0.9807
	5	0.9717
	5.5	0.9670
Double parabolic ( <i>PM/3</i> )	4.5	0.9878
	5	0.9859
	5.5	0.9756

Table 6.7 represents the comparison of thrust coefficient for the three nozzle configurations at *NPRs* 4.5, 5, and 5.5. From the table, it is observed that the thrust coefficient is higher for the double parabolic nozzle and shows a decreasing trend with an increase in *NPR* for all nozzle configurations. Spotts *et al.* (2013) found that the thrust coefficient based on *CFD* predictions show a higher value than the experimental data as the simulations neglect the effect of base drag included in the experimental measurements. Also, the variation was found to increase with increasing *NPR*.

#### 6.4.8 Nozzle Discharge Coefficient

Nozzle discharge coefficient is a performance parameter of the nozzle and can be calculated by using Equation 6.12 reported by Thornock and Sokhey (2013).

$$Cd = \frac{2\pi \int_0^R \rho u r dr}{\dot{m}_{ideal}} \quad (6.12)$$

In this equation also, the subscript '*ideal*' refers to quantity calculated for an ideal nozzle based on one-dimensional isentropic flow assumption. Table 6.8 represents the comparison of the discharge coefficient for the three nozzle configurations at different *NPRs*. From the table, it is observed that there is a negligible influence for different nozzle configurations on discharge coefficients.

Table 6.8: Variation of nozzle discharge coefficients of conical, bell, and *PM/3* double parabolic nozzles at *NPRs* 4.5, 5, and 5.5

<b>Nozzle</b>	<b><i>NPR</i></b>	<b>Nozzle Discharge Coefficient</b>
Conical	4.5	0.9933
	5	0.9931
	5.5	0.9911
Bell	4.5	0.9882
	5	0.9879
	5.5	0.9861
Double parabolic ( <i>PM/3</i> )	4.5	0.9960
	5	0.9959
	5.5	0.9942

## CHAPTER - 7

# EFFECT OF THE MAXIMUM EXPANSION ANGLE IN THE DIVERGENT PORTION OF A DOUBLE PARABOLIC NOZZLE

### 7.1 INTRODUCTION

The experimental investigation on double parabolic nozzle discussed in the previous Chapter reveals that these nozzles have much higher performance than conical and bell nozzles. However, the effect of the expansion angle in the diverging portion of a double parabolic nozzle has been further investigated in this Chapter. The double parabolic nozzles with three different expansion angles such as  $PM/3$ ,  $PM/4$ , and  $PM/5$  have been designed for conducting experiments. In the case of the double parabolic nozzle with  $PM/3$  profile, the maximum expansion angle in the diverging portion is one-third of Prandtl-Meyer angle. The effect of the expansion angle in the diverging portion of the double parabolic nozzles for different expansion angles such as one-third, one-fourth and one-fifth of Prandtl-Meyer angles are analysed numerically and experimentally. Here expansion angles used are less than one-half of the Prandtl-Meyer angle in order to get a more uniform flow at nozzle exit (Puckett, 1946). The measured static pressure and Mach number of different nozzles at different nozzle pressure ratios are compared. Shock cell length and shock angle have been captured from Schlieren images. Potential core length, shock cell count, thrust, nozzle discharge coefficient and thrust coefficients of different nozzles have also been compared.

## 7.2 EXPERIMENTAL ANALYSIS

The flow emanating from the nozzle exit with different expansion angles for the diverging section have been compared by analysing the static and stagnation pressure measurement data and Schlieren images.

### 7.2.1 Static & Stagnation Pressure Measurements

The static and stagnation pressures at different locations along jet axis up to 8 times the exit diameter ( $D_e$ ) were measured for comparing static pressure and Mach number downstream of the flow. Figure 7.1 and 7.2 represents the variation of static pressure along the jet axis at  $NPR$  3.7 and  $NPR$  5 respectively. Theoretically, at design condition, the nozzle exit pressure is same as the atmosphere. The pressure at exit ( $x/D_e=0$ ) of all nozzles is almost atmospheric. Normally, in the case of thrust optimised nozzles even at the designed condition, there is slightly higher value of pressure at the nozzle exit above ambient. This is due to the internal shock formation at the inflation points in thrust optimised nozzle.

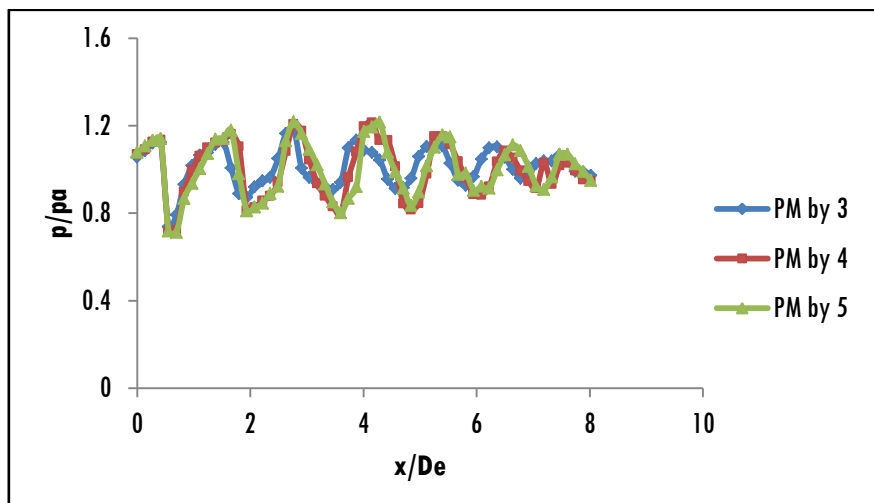


Fig. 7.1 Pressure variation along the jet axis for different nozzles at  $NPR = 3.7$  (Experimental)

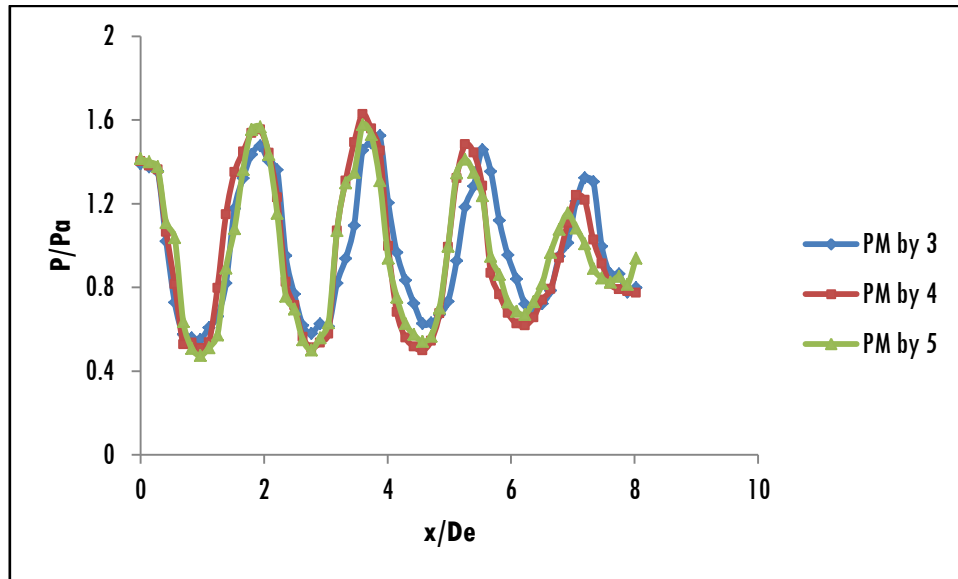


Fig. 7.2 Pressure variation along the jet axis for different nozzles at  $NPR = 5$  (Experimental)

The formation of internal shock is avoided by the development of double parabolic concept. Figure 7.2 shows the static pressure measurements at the under-expanded condition with  $NPR = 5$  at different locations along the centre line of the jet from the nozzle exit to  $8D_e$  for different nozzles. All the three nozzles show almost same exit pressure.

### 7.2.2 Mach Number

The variation of Mach number along the jet axis at  $NPR 3.7$  and  $NPR 5$  are shown in Figure 7.3 and 7.4 respectively. From the figures, it is clear that the variations of pressure and Mach number show a similar trend for all the three nozzle configurations. The exit Mach numbers of double parabolic nozzles with  $PM/3$ ,  $PM/4$ , and  $PM/5$  profiles are almost same at designed and underexpanded conditions.

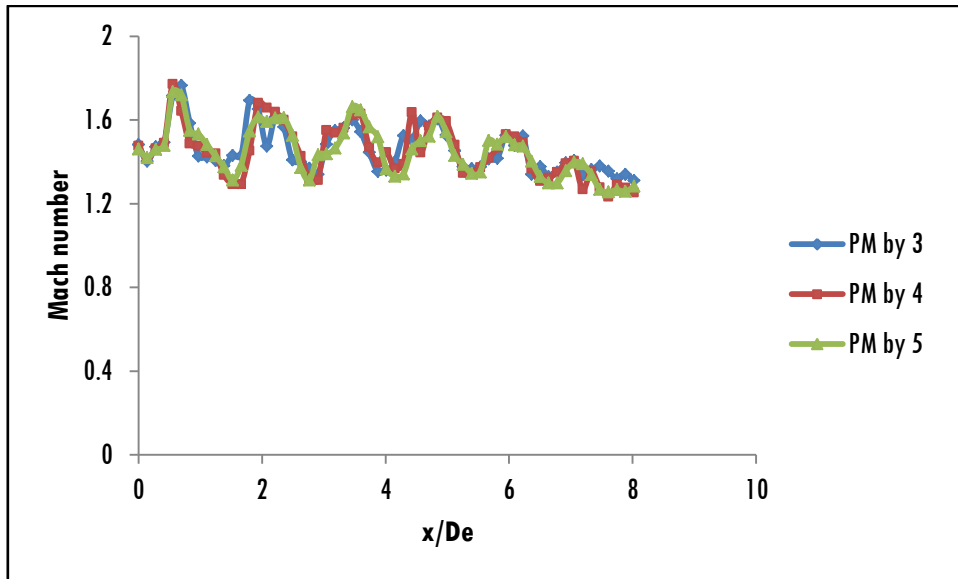


Fig. 7.3 Mach number variation along the jet axis for different nozzles at  $NPR = 3.7$  (Experimental)

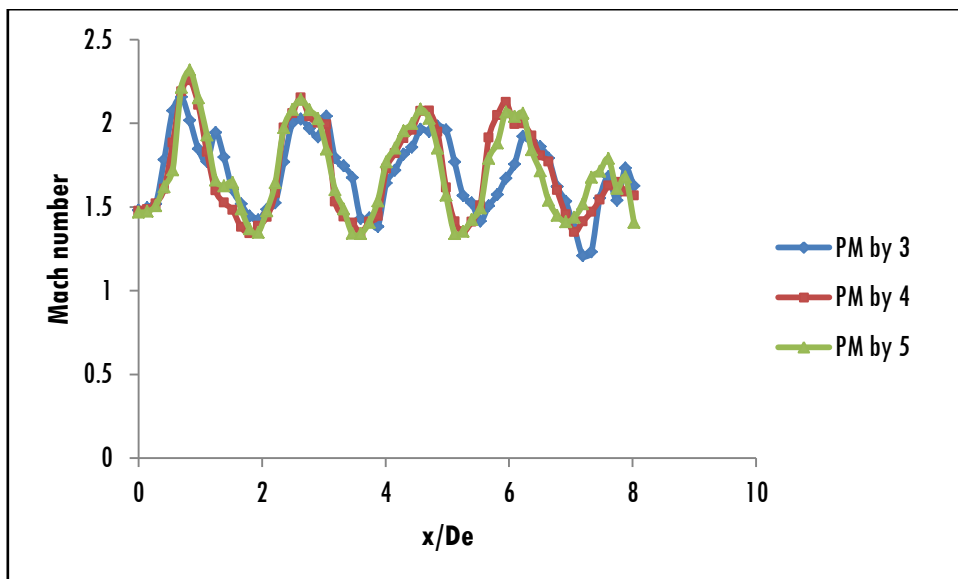


Fig. 7.4 Mach number variation along the jet axis for different nozzles at  $NPR = 5$  (Experimental)

### 7.2.3 Schlieren Image

Schlieren imaging technique has used for capturing flow structure of free stream flow emanating from nozzle exit.



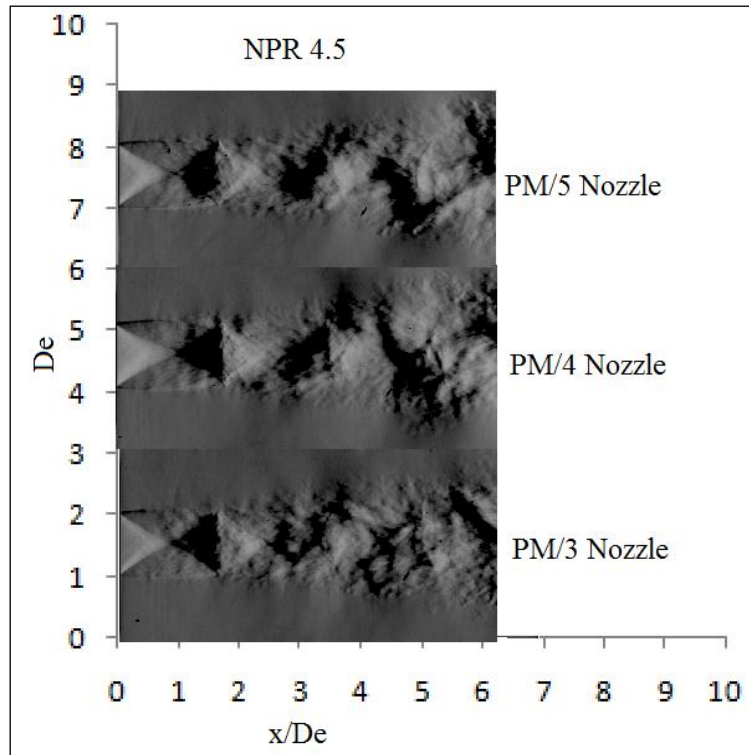


Fig. 7.5 Schlieren images of the double parabolic nozzles with  $PM/3$ ,  $PM/4$ , and  $PM/5$  profiles at  $NPR = 4.5$  (Experimental)

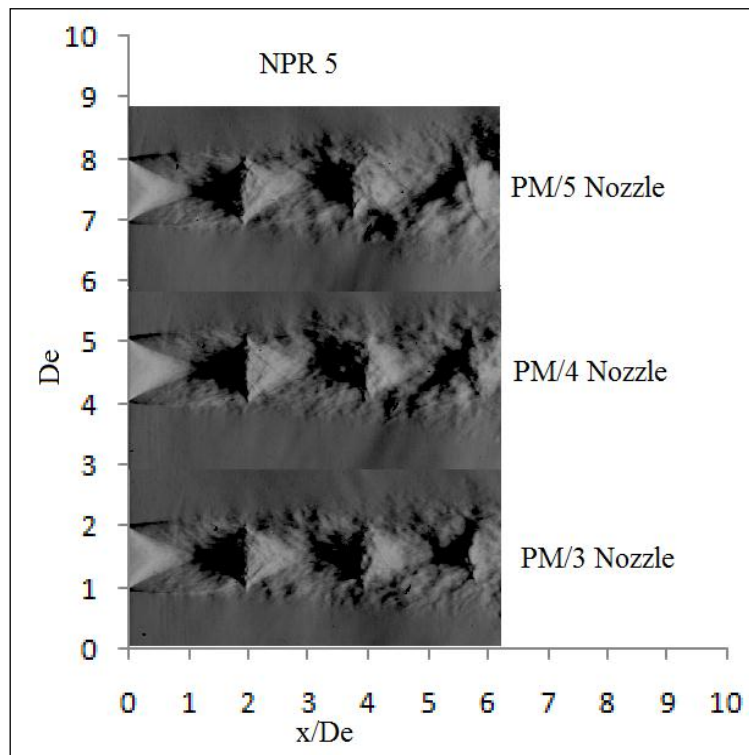


Fig. 7.6 Schlieren images of the double parabolic nozzles with  $PM/3$ ,  $PM/4$ , and  $PM/5$  profiles at  $NPR = 5$  (Experimental)

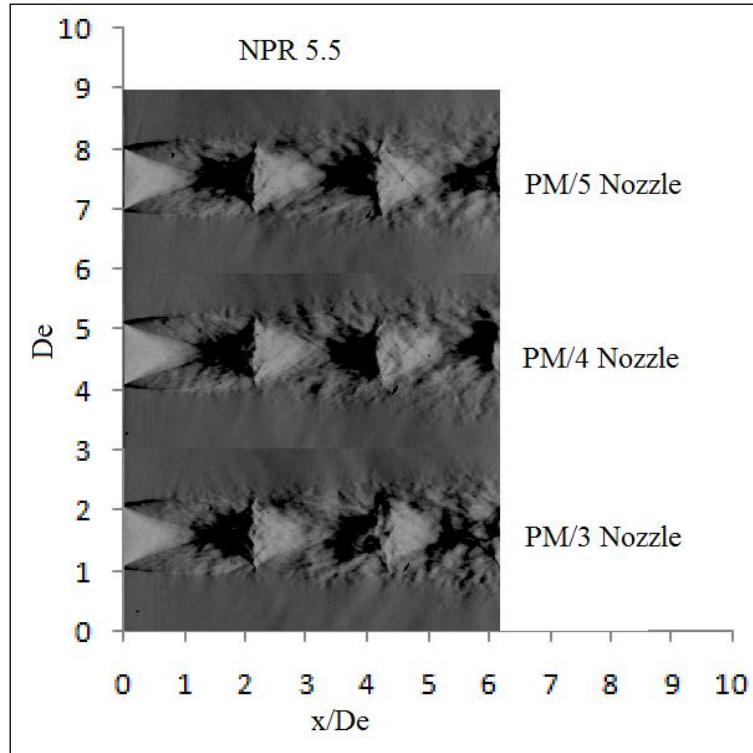


Fig. 7.7 Schlieren images of double parabolic nozzles with  $PM/3$ ,  $PM/4$ , and  $PM/5$  profiles at  $NPR = 5.5$  (Experimental)

Figures 7.5, 7.6, and 7.7 show the comparison of Schlieren images captured for double parabolic nozzles with  $PM/3$ ,  $PM/4$ , and  $PM/5$  profiles at  $NPR$ s 4.5, 5, and 5.5 respectively. It is evident from the figures that there is a negligible variation of shock cell structure with respect to variation in  $PM$  expansion angles.

### 7.3 NUMERICAL ANALYSIS

*ANSYS CFD Academic Version 16.0* with unlimited nodes was used for obtaining the numerical solutions of turbulent compressible supersonic jets incorporating two equations *SST  $k-\omega$*  turbulence model. A 2D computational domain was chosen with a domain length of  $30D_t$  downstream of the nozzle exit and a domain height of  $5D_t$  normal to the jet axis, where  $D_t$  is the throat diameter of the nozzle. A multi-block strategy was used for the construction of grid.

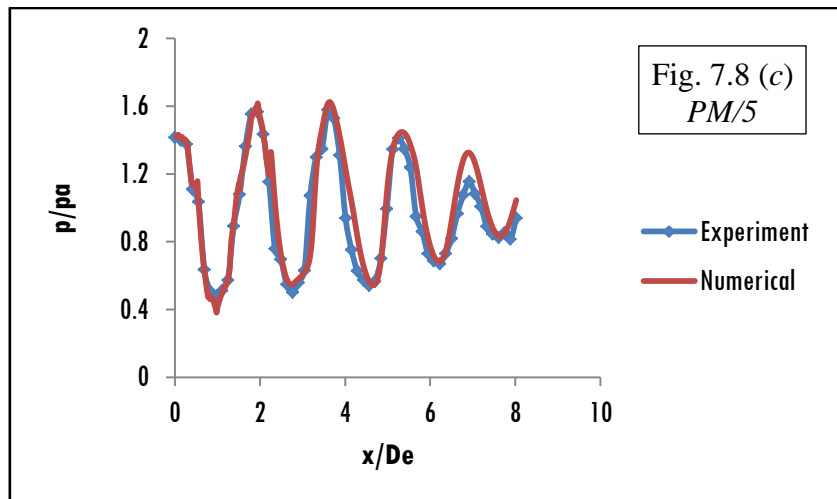
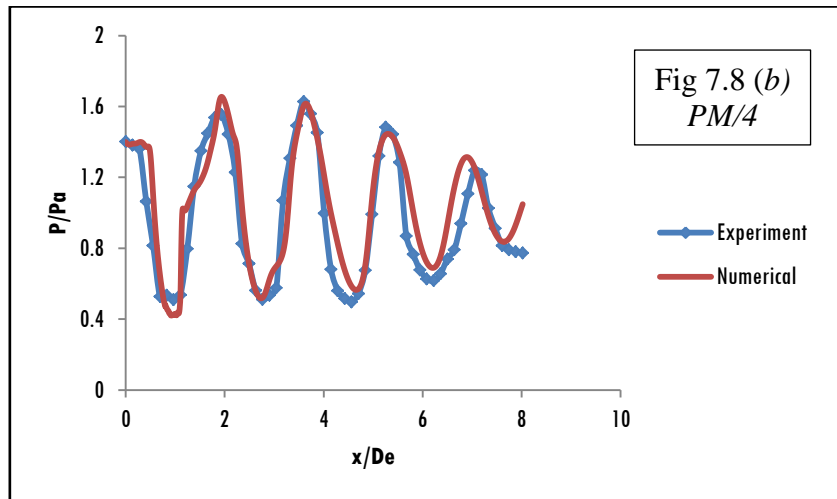
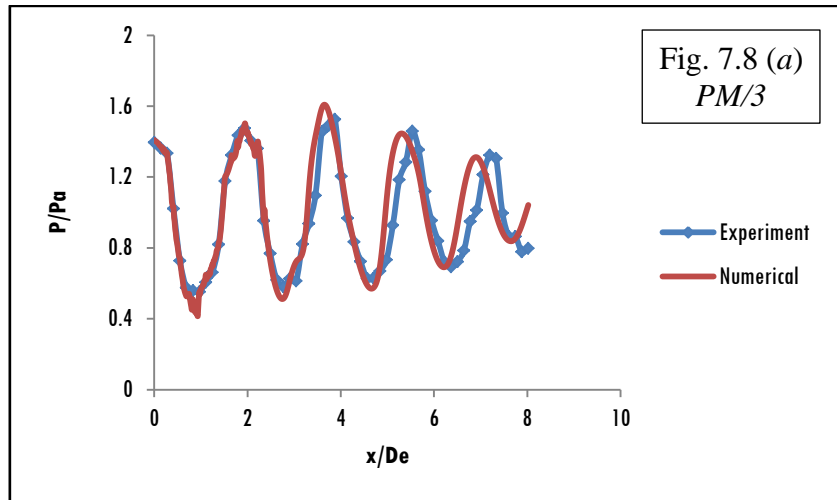


Fig. 7.8 Comparison of experimental data and numerical predictions of pressure variation along the jet axis of different nozzles at  $NPR = 5$  (a)  $PM/3$  (b)  $PM/4$  (c)  $PM/5$

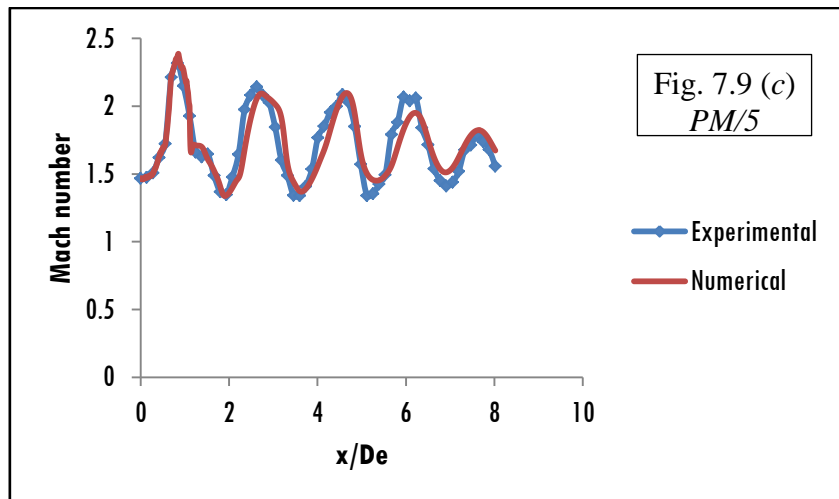
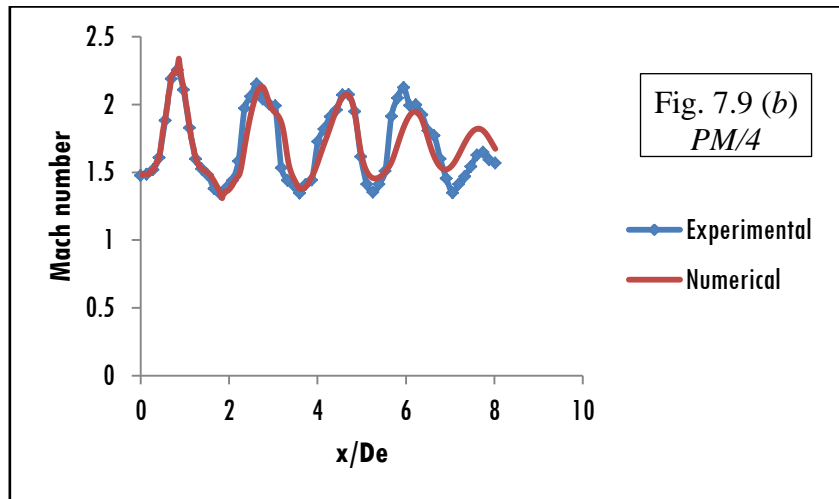
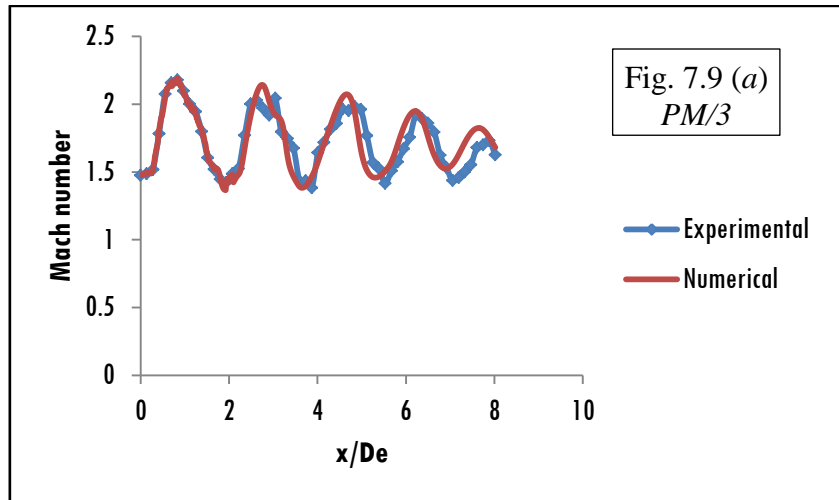


Fig. 7.9 Experimental data and numerical predictions of Mach number variation along the jet axis of different nozzles at  $NPR = 5$   
(a) *PM/3* (b) *PM/4* (c) *PM/5*

Numerical predictions of flow emanating from different nozzle configurations at design conditions were compared with the experimental data measured for the same nozzle pressure ratio of 3.7 and 5. Figure 7.8 predicts the free stream static pressure and Figure 7.9 predicts the Mach numbers of (a)  $PM/3$ , (b)  $PM/4$ , and (c)  $PM/5$  double parabolic nozzles respectively at  $NPR = 5$ . It is observed that the solution matches well with experimental data up to an axial distance of  $7D_e$ . The percentage of deviation between experimental and numerical results is less than 5% even at a distance of  $7 D_e$  from the nozzle exit. This is due to lesser magnitude of shock cell oscillations at underexpanded conditions of all double parabolic nozzles than that of conical and bell. Hence  $SST k-\omega$  turbulent model is well suited for the prediction of centre line pressure and Mach number of supersonic flows emanating from conical, bell, and  $PM/3$  double parabolic nozzles at design condition as well as at underexpanded condition.

## **7.4 NOZZLE PERFORMANCE PARAMETERS**

In this section, the flow characteristics and nozzle performance parameters of double parabolic nozzles with  $PM/3$ ,  $PM/4$ , and  $PM/5$  profiles are compared.

### **7.4.1 Shock Cell Length**

Shock cell length of double parabolic nozzles with  $PM/3$ ,  $PM/4$ , and  $PM/5$  profiles at different  $NPRs$  were determined from the Schlieren images. The shock cell lengths were also predicted by equations developed by Pack (1950) and Mehta and Prasad (1996).

Figures 7.10, 7.11, and 7.12 demonstrate the variations of shock cell lengths at different  $NPR$ s for double parabolic nozzles with  $PM/3$ ,  $PM/4$ , and  $PM/5$  profiles. The figures demonstrate that the nozzle contour has not much influence on shock cell length. Table 7.1 shows a comparison of shock cell lengths for different  $NPR$ s by analysing the Schlieren images obtained experimentally and also from the equations developed by earlier researchers. From the table, it is clear that the shock cell length increases with increasing  $NPR$ s and the equation developed by Mehta and Prasad predicts the shock cell length better.

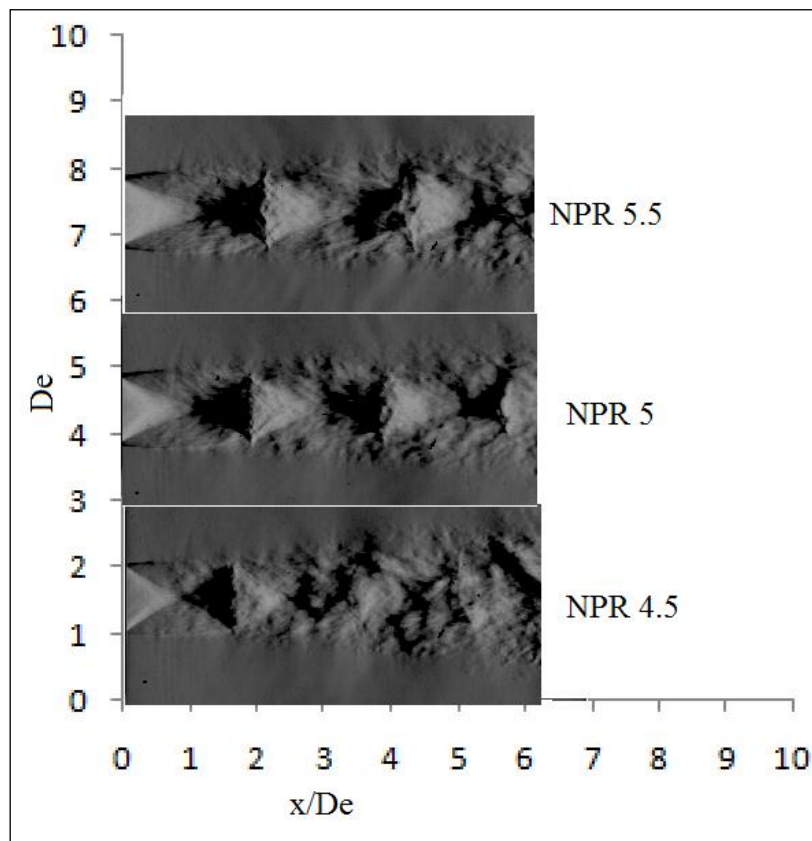


Fig. 7.10 Schlieren images of the double parabolic nozzle with  $PM/3$  profile at  $NPR$ s of 4.5, 5, and 5.5 (Experimental)

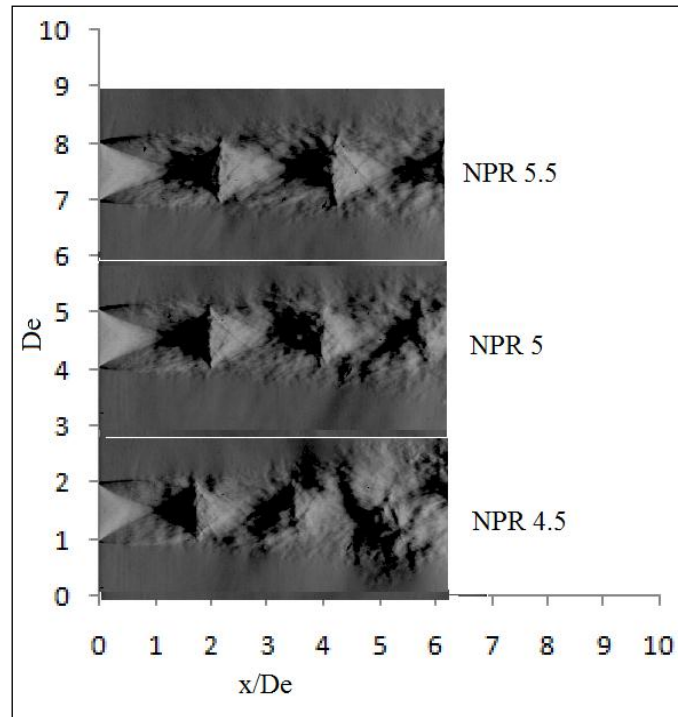


Fig. 7.11 Schlieren images of the double parabolic nozzle with  $PM/4$  profile at  $NPR$ s of 4.5, 5, and 5.5 (Experimental)

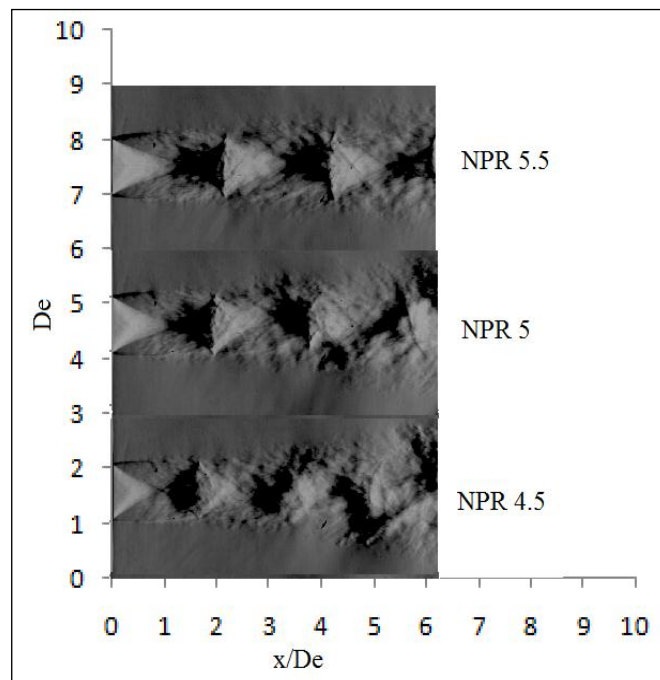


Fig. 7.12 Schlieren images of the double parabolic nozzle with  $PM/5$  profile at  $NPR$ s of 4.5, 5 and 5.5 (Experimental)

Table 7.1: Variation of shock cell lengths of the double parabolic nozzles with  $PM/3$ ,  $PM/4$ , and  $PM/5$  profiles at  $NPR$ s 4.5, 5, and 5.5

Nozzle	$NPR$	Shock cell length from		
		Schlieren image	Pack relation	Mehta and Prasad relation
$PM/3$ Double Parabolic	4.5	$1.83 D_e$	$1.70 D_e$	$1.87 D_e$
	5	$1.90 D_e$	$1.81 D_e$	$1.90 D_e$
	5.5	$1.95 D_e$	$1.91 D_e$	$1.95 D_e$
$PM/4$ Double Parabolic	4.5	$1.83 D_e$	$1.70 D_e$	$1.87 D_e$
	5	$1.90 D_e$	$1.81 D_e$	$1.90 D_e$
	5.5	$1.96 D_e$	$1.91 D_e$	$1.95 D_e$
$PM/5$ Double Parabolic	4.5	$1.83 D_e$	$1.70 D_e$	$1.87 D_e$
	5	$1.90 D_e$	$1.81 D_e$	$1.90 D_e$
	5.5	$1.96 D_e$	$1.91 D_e$	$1.95 D_e$

#### 7.4.2 Shock Cell Count

Figures 7.13 and 7.14 represent the velocity and density contour of the double parabolic nozzles with  $PM/3$ ,  $PM/4$ , and  $PM/5$  profiles at  $NPR = 5$ . These figures show that there is a negligible influence on the expansion angle of double parabolic nozzle configuration on shock cell count. However, the strength of the shock inside the shock cell seems to be less for the double parabolic nozzle with  $PM/3$  profile. Shock cell count for all nozzles at  $NPR$ s 4.5, 5, and 5.5 are 4, 5, and 6 respectively.



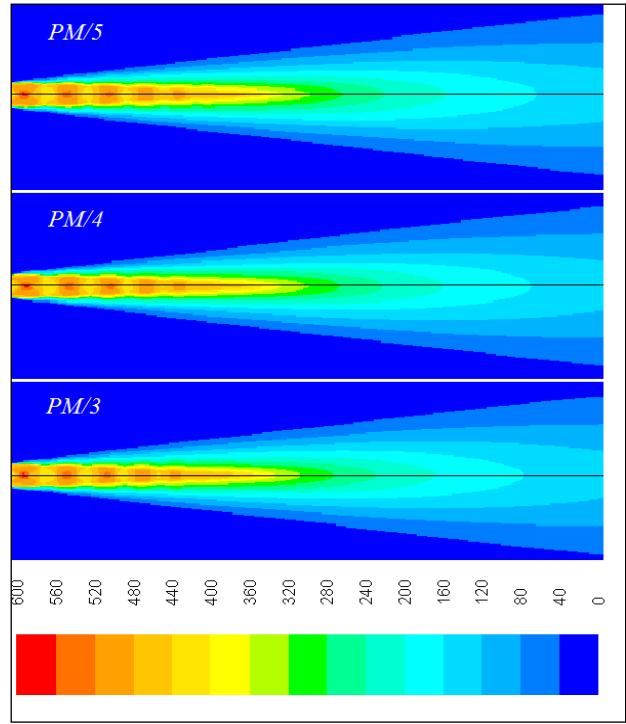


Fig. 7.13 Velocity contours (m/s) of the double parabolic nozzles with *PM/3*, *PM/4*, and *PM/5* profiles at  $NPR = 5$  (Numerical)

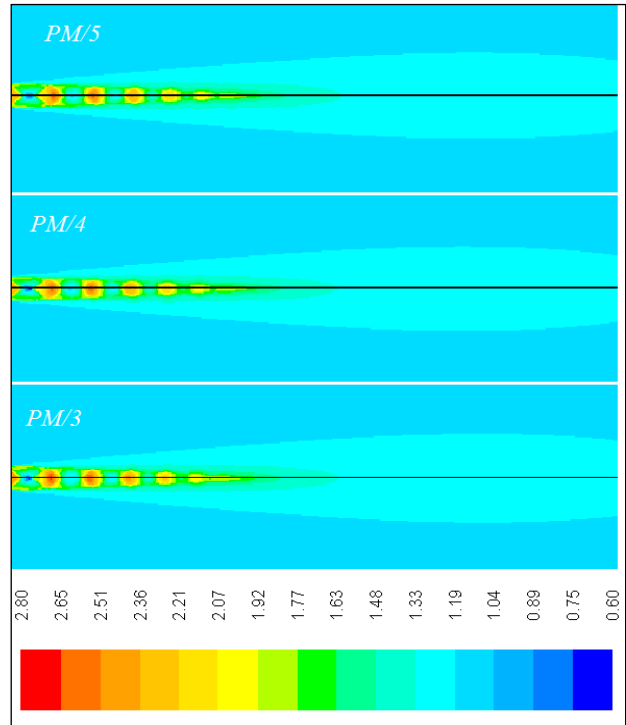


Fig. 7.14 Density contours ( $\text{kg/m}^3$ ) of the double parabolic nozzles with *PM/3*, *PM/4*, and *PM/5* profiles at  $NPR = 5$  (Numerical)

### 7.4.3 Potential Core Length

Potential core length may be defined as the distance over which the centre line velocity remains at least 95% of mean axial velocity. Figure 7.15 shows the variation of the ratio of centreline velocity to mean centreline velocity along the jet axis of *PM/3*, *PM/4*, and *PM/5* double parabolic nozzles at *NPR* 5 obtained from numerical simulations. From the figure, it is clear that all the graphs are superimposing each other. Table 7.2 reveals that there is no influence of expansion angle in the double parabolic nozzle in the development of potential core.

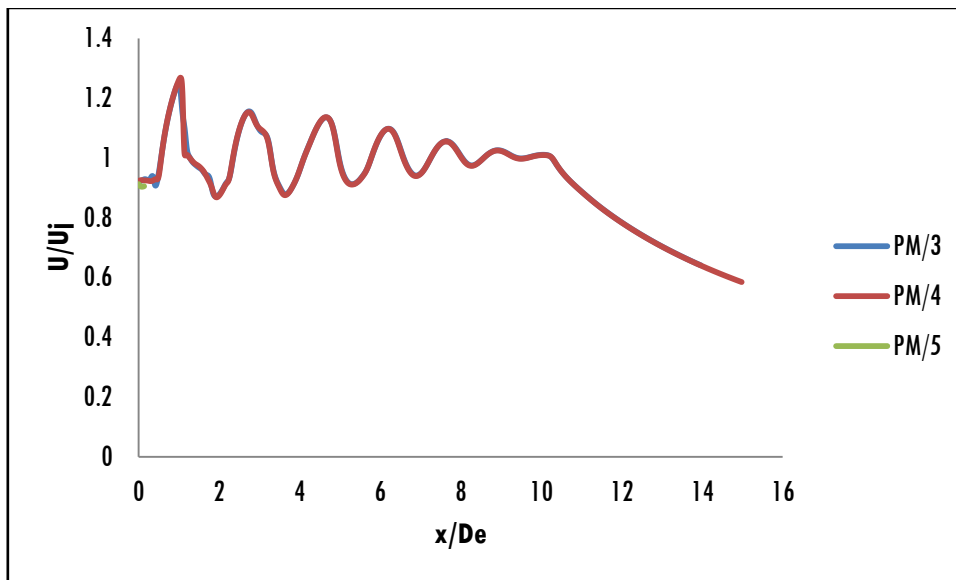


Fig. 7.15 Comparison of the mean axial velocity of the double parabolic nozzles with *PM/3*, *PM/4*, and *PM/5* profiles at *NPR* = 5

Table 7.2: Potential core length of the double parabolic nozzles with *PM/3*, *PM/4*, and *PM/5* profiles at *NPRs* 4.5, 5, and 5.5

Nozzle	<i>NPR</i> = 4.5	<i>NPR</i> = 5	<i>NPR</i> = 5.5
<i>PM/3</i> Nozzle	9.80 $D_e$	10.35 $D_e$	10.57 $D_e$
<i>PM/4</i> Nozzle	9.80 $D_e$	10.35 $D_e$	10.58 $D_e$
<i>PM/5</i> Nozzle	9.80 $D_e$	10.35 $D_e$	10.58 $D_e$

#### 7.4.4 Nozzle Thrust

Table 7.3 represents the comparison of thrusts for double parabolic nozzles with *PM/3*, *PM/4*, and *PM/5* profiles at different *NPRs*. The double parabolic nozzle with *PM/3* profile has a marginal thrust augmentation of only 0.1% with respect to *PM/4* and *PM/5* profiles, which can only be considered as a favourable trend among DP nozzles for further analysis. However, double parabolic nozzles with *PM/3* profile seems to have a better thrust when compared with the other nozzles, especially at higher *NPRs*.

Table 7.3: Thrust generation of the double parabolic nozzles with *PM/3*, *PM/4*, and *PM/5* profiles at *NPRs* 4.5, 5, and 5.5

Nozzle	<i>NPR</i>	Total Thrust (N)
<i>PM/3</i> Double parabolic	4.5	149.47
	5	169.73
	5.5	187.99
<i>PM/4</i> Double parabolic	4.5	149.47
	5	169.70
	5.5	187.85
<i>PM/5</i> Double parabolic	4.5	149.47
	5	169.69
	5.5	187.81

Table 7.4: Nozzle thrust coefficients of the double parabolic nozzles with *PM/3*, *PM/4*, and *PM/5* profiles at *NPRs* 4.5, 5, and 5

Nozzle	<i>NPR</i>	Nozzle Thrust Coefficient	Nozzle Discharge Coefficient
<i>PM/3</i> Double parabolic	4.5	0.9878	0.9960
	5	0.9859	0.9959
	5.5	0.9756	0.9942
<i>PM/4</i> Double parabolic	4.5	0.9878	0.9960
	5	0.9855	0.9956
	5.5	0.9742	0.9935
<i>PM/5</i> Double parabolic	4.5	0.9878	0.9960
	5	0.9853	0.9954
	5.5	0.9742	0.9932

#### 7.4.5 Nozzle Thrust and Discharge Coefficients

Table 7.4 represents the comparison of thrust and discharge coefficient for the double parabolic nozzles with  $PM/3$ ,  $PM/4$ , and  $PM/5$  profiles at  $NPR$ s 4.5, 5, and 5.5. From the table, it is observed that the thrust and discharge coefficients for the three nozzles have approximately the same value with a marginal advantage for  $PM/3$  expansion nozzle.

### 7.5 SUMMARY

A detailed experimental and numerical analysis of supersonic jets emanating from different double parabolic nozzles with expansion angles  $PM/3$ ,  $PM/4$ , and  $PM/5$  were carried out. The static and stagnation pressure measurements were taken and Schlieren images captured for experimental analysis. The numerical analysis has been carried out by using *RANS* calculations with *SST  $k-\omega$*  turbulence model. The predictions seem to be matching reasonably well with experimental results. Shock cell length, shock cell count, potential core length, nozzle thrust, thrust and discharge coefficients have been calculated. It was observed that there is only negligible variation in flow characteristics by reducing the expansion angle lesser than one-third of Prandtl-Meyer angle. Even though the double parabolic nozzle with  $PM/3$  profile is having only marginal advantage in thrust and discharge coefficients, the weight of the nozzle is less (as divergent section is of lesser length due to larger divergent angle) which is an added advantage of this nozzle configuration, especially for space applications. The comparison of the length of the divergent portion of the nozzles reveals that the double parabolic nozzles with  $PM/4$  and  $PM/5$  profiles have longer length of 33.39% and 64.74% respectively when compared with that of the double

parabolic nozzle with  $PM/3$  profile. Nowadays the major focus is on weight reduction of propulsive systems which in turn allow the designers to prefer shorter nozzle configurations. There is no augmentation in thrust by reducing the maximum expansion angle in the diverging portion of the double parabolic nozzle with  $PM/4$  and  $PM/5$  profile rather than an increase in weight. It may be concluded that double parabolic nozzle with an expansion angle of  $PM/3$  seems to be ideal for generating required thrust without any weight penalty after meticulously analysing the performance of the different nozzle configurations.

## **CHAPTER - 8**

### **CONCLUSIONS**

A novel concept has been introduced in the design of a convergent-divergent nozzle for generating supersonic flow at the exit and subsequently, the flow characteristics and nozzle performance parameters analysed systematically. The performance of the newly designed 'double parabolic nozzle' has been evaluated experimentally and compared with the conventional conical and bell nozzles of similar dimensions. A comprehensive numerical investigation has also been carried out after selecting the best turbulence model for predicting the flow characteristics of supersonic jets. The effect of maximum expansion angles ( $PM/3$ ,  $PM/4$ , and  $PM/5$ ) in the divergent portion of the double parabolic nozzle was analysed and the generation of thrust for each nozzle profile was evaluated.

#### **8.1 EXPERIMENTAL & NUMERICAL ANALYSIS OF PERFORMANCE PARAMETERS OF CONICAL, BELL, AND DOUBLE PARABOLIC NOZZLES**

The double parabolic nozzle was designed in such a way that the divergent portion is a combination of two parabolas; one starting from the throat and the other ending at the nozzle exit and the intersection point of the two parabolas is a function of the Prandtl-Meyer ( $PM$ ) angle. The lengths of the double parabolic nozzle with  $PM/3$  profile, bell, and conical nozzles were kept identical for the sake of comparison with the same nozzle throat diameter of 20 mm and a design Mach number of 1.5.

The experimental investigation basically focused on the static and stagnation pressure measurements by static and stagnation pitot probes respectively. The pressure probe was housed in a three-axis traverse of pitch 3 mm for measuring the static and stagnation pressures at 660 points in the flow field downstream of the nozzle at intervals of 3 mm in the axial and radial directions at *NPRs* of 3.7, 4.5, 5, and 5.5. Moreover, the flow field was visualised by using a conventional Z-type Schlieren system and images of the shock cell structure captured for all nozzle pressure ratios.

A commercially accessible finite volume solver was used for obtaining the numerical solutions of turbulent compressible supersonic jets based on density based solver with *RANS* equations employing appropriate turbulence model. The best-suited turbulence model for the flow characteristics of a supersonic jet was selected after conducting numerical simulations employing different turbulence models such as Standard *k-ε* model, *RNG k-ε* model, Realizable *k-ε* model, and *SST k-ω* model. Later the centreline and radial profiles of density, velocity, and temperature of the numerical predictions from the above models were compared with the experimental data. *SST k-ω* was selected as the best-suited turbulence model for predicting supersonic flow characteristics. Hence all numerical simulations were then carried out with the aid of *SST k-ω* turbulence model.

Even though nozzle exits pressure is the same as atmospheric theoretically, while operating at designed conditions, the corresponding values of conical and bell nozzles are slightly higher than atmospheric. It is primarily due to the formation of internal shocks at the throat of the conical nozzle and along the circular arc region for bell nozzle. However, it was noticed that the nozzle exit pressure of the double parabolic

nozzle is almost atmospheric which means that these internal shock formation can be considerably eliminated with the introduction of double parabolic arcs, especially at design conditions.

At under-expanded condition of  $NPR = 5$ , the experimental value of double parabolic nozzle remains at 1.36 bar in proportion to the expected static pressure at nozzle exit of 1.36 bar theoretically. However, both conical and bell nozzles have shown a higher exit pressure than the double parabolic nozzle. The expected Mach number at the nozzle exit under these conditions is 1.5. Due to the presence of internal shock formation in the regions close to the throat and circular arc profile, the Mach numbers at the exit of conical and bell nozzles are less than what was expected.

Schlieren images captured depict multiple dark and white regions, which indicate the high-density compression zone and low-density expansion zone. The sharp vertical boundaries at the compression zone represent the extinction position of each shock. It was observed from the images that the flow was unsteady and oscillating in axisymmetric and helical mode. The shock cell length and shock wave angle of conical, bell, and double parabolic nozzle with  $PM/3$  profile at  $NPR$ s 4.5, 5 and 5.5 were determined from image analysing codes. It was observed that shock cell lengths increase with increasing  $NPR$  and nozzle contour has less influence on shock cell length. Shock cell count also increases with increasing  $NPR$  and its dependence on the profile of nozzle contour is negligible. The calculations of shock cell length by using Mehta and Prasad (1996) equation closely matches with experimental results. However, Prandtl-Pack relation gave slight variations in the values of shock cell length.



Potential core length and supersonic core length of conical, bell, and double parabolic ( $PM/3$ ) nozzles at  $NPR$ s 4.5, 5, and 5.5 have also been determined. Both potential core and supersonic core lengths increase with increasing  $NPR$ s. It is observed that there is a slight reduction in potential core length of the jet emanating from double parabolic ( $PM/3$ ) nozzle than conical and bell nozzles. This reduction in length indicates the improvement of turbulent mixing and thereby flow structure for the double parabolic ( $PM/3$ ) nozzle. Moreover, the enhancement in turbulent mixing reduces noise which is again an added benefit. Supersonic length has been calculated from the Mach number decay method, total pressure decay method, and the method developed by Shirie and Seubold. The magnitude of supersonic length was over-predicted by the Shirie and Seubold method when compared with the numerical predictions.

The thrust developed by the double parabolic nozzle with  $PM/3$  profile is higher when compared with that of conical and bell nozzles. The augmentation in thrust for the double parabolic nozzle is calculated to be 1% and is persistent with the observations reported by Sternin (2000) for improved nozzle configurations. The thrust coefficient was also determined by the equation reported by Spottset *al.* (2013) and found to decrease with increase in  $NPR$ . The thrust coefficients of the double parabolic nozzle with  $PM/3$  profile at all  $NPR$ s are higher than that of conical and bell nozzles. The nozzle discharge coefficient calculated from the equation reported by Thornock and Sokhey (2013) was also found to decrease with increasing  $NPR$ . It has been observed that the nozzle profile has less influence on the nozzle discharge coefficient. The analysis of performance parameters indicates that the double parabolic nozzle with  $PM/3$  profile is a better choice for creating supersonic flow than conventional conical and bell nozzles.

## 8.2 EFFECT OF EXPANSION ANGLE IN THE DIVERGENT PORTION OF DOUBLE PARABOLIC NOZZLES

The maximum expansion angle in the divergent portion of a double parabolic nozzle with  $PM/3$  profile is one-third of Prandtl-Meyer angle. For the comprehensiveness of the analysis, experimental and numerical investigations have also been carried out for finding the effect of maximum expansion angle in the diverging portion of a double parabolic nozzle. With this purpose in mind, double parabolic nozzles with different expansion angles such as one-third, one-fourth, and one-fifth of Prandtl-Meyer angles were designed and fabricated. Here the lengths of the nozzles are different and the  $DP$  nozzle with  $PM/3$  profile is the smallest among them. The comparison in length of the divergent portions clearly shows an increase in length of 33.39% and 64.74% respectively for  $PM/4$  and  $PM/5$  profiled double parabolic nozzle when compared with that of  $DP$  nozzle with  $PM/3$  profile. However, there is only marginal difference in shock cell length, potential core length, thrust, thrust/discharge coefficients etc. between  $PM/3$ ,  $PM/4$ , and  $PM/5$  profiled nozzles. Among all these nozzles for producing same Mach number,  $PM/3$  is the smallest one and thereby the least weight. The current trend in rocketry, as well as aerospace industry, is to reduce the weight of the propulsive system. The comprehensive analysis of the flow and performance parameters including nozzle weight, economical and environmental metrics demonstrates that the double parabolic nozzle with  $PM/3$  profile is best suited for supersonic flows than any other conventional conical and bell nozzles.

### **8.3 FUTURE WORK**

The current investigation was carried out on convergent-divergent nozzles with a throat diameter of 20 mm which was decided on the basis of time taken for emptying the storage tank corresponding to the range of *NPRs* studied. A comprehensive study may also be performed with nozzles having larger throat diameters so that the nozzle performance parameters may be evaluated to a better level of accuracy. The present analysis may also be extended to the acoustic measurements and calculations to determine the noise benefits if any, as the noise regulations recommended by ICAO have become more and more stringent.

## REFERENCES

1. **Allamaprabhu Y., Raghunandan B.N., and Morinigo J.A.** (2011) Improved prediction of flow separation in thrust optimised parabolic nozzles with Fluent. *47th AIAA/ASME/SAE/ASEE Joint Propulsion Conference and Exhibit*, AIAA 2011-5689.
2. **Allamaprabhu Y., Raghunandan B.N., and Morinigo J.A.** (2016) Numerical prediction of nozzle flow separation: Issue of turbulence modeling. *Aerospace Science and Technology*, 50, 31-43.
3. **Allman J.G., and Hoffman J.D.** (1981) Design of maximum thrust nozzle contours by direct optimization methods. *AIAA Journal*, 19 (6), 750-751.
4. **Anderson Jr. J.D.** (1982) Fundamentals of aerodynamics. *McGraw-Hill Book Company*, New York.
5. **Anderson Jr. J.D.** (1988) Modern compressible flow: with historical perspective. *McGraw-Hill Book Company*, New York.
6. **Anderson J.D.** (1997) A history of aerodynamics and its impact on flying machines. Cambridge University Press.
7. **Andre B., Castelain T., and Bailly C.** (2014a) Investigation of the mixing layer of underexpanded supersonic jets by particle image velocimetry. *International Journal of Heat and Fluid Flow*, 50, 188-200.
8. **Andre B., Castelain T., and Bailly C.** (2014b) Experimental exploration of an underexpanded supersonic jet. *Shock waves*, 24(1), 21-32.
9. **Andreopoulos J., Muck K., and Dussauge J.** (1988) Unsteady nature of shock wave boundary layer interaction. *AIAA Journal*, 26(2), 179-187.
10. **Argrow B.M., and Emanuel G.** (1988) Comparison of minimum length nozzles. *Journal of Fluid Engineering*, 110, 283-288.
11. **Baek S.C., Kwon S.B., Kim H.D., Setoguchi T., and Matsuo S.** (2006) Study of moderately underexpanded supersonic moist air jets. *AIAA Journal*, 44(7), 1624-1627.
12. **Balabel A., Hegab A.M., Nasr M., and Samy M. El-Behery** (2011) Assessment of turbulence modeling for gas flow in two-dimensional convergent-divergent rocket nozzle. *Applied Mathematical Modelling*, 17, 3408-3422.
13. **Bayeh A.C.** (2009) Analysis of mach disks from an underexpanded nozzle using experimental and computational methods. *AIAA paper*, AIAA 2009-217.

14. **Chen C.I., Chakravarthy S.R., and Hung C.M.** (1994) Numerical investigation of separated nozzle flows. *AIAA Journal*, 32(9), 1836-1843.
15. **Cuppoletti D., Gutmark E., Hafsteinsson H., and Eriksson L.E.** (2014) The role of nozzle contour on supersonic jet thrust and acoustics. *AIAA Journal*, 52(11), 2594-2614.
16. **Dumitrescu L.Z.** (1975) Minimum length axisymmetric laval nozzles. *AIAA Journal*, 13, 520-532.
17. **Emami B., Bussmann M., and Tran H.N.** (2009) A mean flow field solution to a moderately under/over-expanded turbulent supersonic jet. *Comptes Rendus Mecanique*, 337, 185-191.
18. **Emanuel G.**(1986) Gas dynamic: Theory and application. *AIAA Educational Series*, New York.
19. **Frey M., and Hagemann G.** (1998) Status of flow separation prediction in rocket nozzles. *34th AIAA/ASME/SAE/ASEE Joint Propulsion Conference and Exhibit, Cleveland*, AIAA 1998-3619.
20. **Frey M., and Hagemann G.** (2000) Restricted shock separation in rocket nozzles. *Journal of propulsion and power*, 16(3), 478-484.
21. **Frey M., Stark R., Ciezki H.K., Quessard F., and Kwan W.** (2000) Subscale nozzle testing at the P6.2 test stand. *36th AIAA/ASME/SAE/ASEE Joint Propulsion Conference and Exhibit, Las Vegas*, AIAA 2000-3777.
22. **Gamble E., Dwain Terrell P. E., Rich Defrancesco** (2004) Nozzle selection and design criteria. *AIAA 2004-3923*.
23. **Genin C., and Stark R.** (2009) Flow transition in dual bell nozzles. *Shock waves*, 19, 265-270.
24. **Genin C., and Stark R.** (2010) Experimental study on flow transition in dual bell nozzles. *Journal of Propulsion and power*, 26(3), 497-502.
25. **Genin C., and Stark R.** (2016) Experimental investigation of cold flow TIC nozzles, a spectral analysis. *52nd AIAA/SAE/ASEE Joint Propulsion Conference, Salt Lake*, AIAA 2016-4668.
26. **Gross A., and Weiland C.** (2007) Numerical simulation of separated cold gas nozzle flows. *Journal of Propulsion and Power*, 20(3), 509-519.
27. **Gustafsson K.M.B., Cuppoletti D., Gutmark E., Hafsteinsson H. E., Eriksson L.E., and Prisell E.** (2012) Nozzle throat optimization for supersonic jet noise reduction. *50th AIAA Aerospace Sciences Meeting including the New Horizons Forum and Aerospace Exposition, Nishville, Tennessee*, AIAA 2012-0247.

28. **Hagemann G., and Frey M.** (2008) Shock pattern in the plume of rocket nozzles: needs for design consideration. *Shock Waves*, 17(6), 387-395.
29. **Hagemann G., Frey M., and Koschel W.**(2002) Appearance of restricted shock separation in rocket nozzles. *Journal of Propulsion and Power*, 18(3), 577-584.
30. **Hamed A., and Vogiatzist C.** (1997) Overexpanded two-dimensional convergent-divergent nozzle flow simulations, assessment of turbulence models. *Journal of Propulsion and Power*, 13(3), 444-445.
31. **Hamed A., and Vogiatzist C.** (1998) Overexpanded two-dimensional convergent-divergent performance, effects of three-dimensional flow interactions. *Journal of Propulsion and Power*, 14(2), 234-240.
32. **Hiers R., MacKinnon H., and Beitel G.** (2004) Validation of stream thrust probes for turbine engine thrust measurement. *42nd AIAA Aerospace Science meeting*, AIAA 2004-1297.
33. **Hoffman J.D.** (1987) Design of compressed truncated perfect nozzles, *Journal of propulsion and power*, 3(2), 150-156.
34. **Huang D. H., Huzel D.K.** (1992) Modern engineering for design of liquid-propellant rocket engines. *Progress in Astronautics and Aeronautics*, AIAA.
35. **Hunter C.A** (1998) Experimental, theoretical, and computational investigation of separated nozzle flows. *34<sup>th</sup> AIAA/ASME/SAE/ASEE Joint Propulsion Conference and Exhibit, Joint Propulsion Conferences*, AIAA 1998-3107.
36. **Jegade O. O., and Crowther. W. J.** (2016) Low order supersonic nozzle design using superimposed characteristics. *54th AIAA Aerospace Science Meeting, AIAA SciTech Forum*, AIAA 2016-0805.
37. **Jeronimo A., Riethmuller M.L., and Chazot O.**(2002) PIV application to Mach 3.75 overexpanded jet. *11th International symposium on Application of laser techniques to fluid mechanics*, Lisbon.
38. **Katanoda H., Miyazato Y., Masuda M., and Matsuo K.** (2000) Pitot pressures of correctly-expanded and underexpanded free jets from axisymmetric supersonic nozzles. *Shock waves*, 10(2), 95-101.
39. **Kaushik M., and Hanmaiahgari P.R.** (2015) Effects of underexpansion level on sonic turbulent jets propagation. *American Journal of Fluid Dynamics*, 5(3A), 12-18.
40. **Knuth E.L** (1960) Optimum contours for propulsion nozzles. *ARS Journal*, 30(10), 983-984.

41. **Kuehner J.P., Dutton J.C., and Lucht R.P.** (2000) High resolution N2 CARS measurements of pressure, temperature and density using a modelless dye laser. *22nd AIAA Aerodynamic Measurement Technology and Ground Testing Conference*, AIAA 2002-2915.
42. **Kulhanek S.L.** (2012) Design, analysis, and simulation of rocket propulsion system. *Thesis of Master of Science*, University of Kansas.
43. **Launder B.E. and Sharma B.I.** (1974) Application of the energy dissipation model of turbulence to the calculation of flow near a spinning disc. *Letters in Heat and Mass Transfer*, 1(2), 131-137.
44. **Li X., Zhou R., Yao W., and Fan X.** (2017) Flow characteristic of highly underexpanded jets from various nozzle geometries. *Applied Thermal Engineering*, 125, 240-253.
45. **Love E.S., Grigsby C.E., Lee L.P., and Woodling M.J.** (1959) Experimental and theoretical studies of axisymmetric free jets. *NASA TR R-6*, 1-298.
46. **Manski D., and Hagemann G.** (1996) Influence of rocket design parameters on engine nozzle efficiencies. *Journal of Propulsion and Power*, 12, 41-47.
47. **Meerbeek W.B.A., Zandbergen B.T.C., and Sonverein L.J.** (2013) A procedure for altitude optimisation of parabolic nozzle contours considering thrust, weight and size. *5th European conference for Aeronautics and space science (EUCASS)*, 1-10.
48. **Mehta R.C., Natarajan G., and Bose N.** (2012) Fully expanded supersonic flow inside conical and contour nozzle. *Journal of Spacecraft and rockets*, 49(2), 422-424.
49. **Mehta R.C., and Prasad J.K.** (1996) Estimation of shock cell structure of axisymmetric supersonic free jets. *Indian Journal of Engineering and Materials Sciences*, 3(4), 141-147.
50. **Meier G.E.A.** (2002) Computerized background-oriented schlieren. *Experiments in Fluids*, 33(1), 181-187.
51. **Melnikova D.A., Pirumov U.G., and Sergienko A.A.** (1976) Jet engine nozzles. *Aeromechanics and Gas dynamics (in Russian)*, Nauka, Moscow, 1976, 57-75.
52. **Menter F.** (1994) Two-equation eddy-viscosity turbulence model for engineering applications. *AIAA Journal*, 32, 1598-1605.
53. **Mern J., and Agarwal R.** (2013) A study of numerical simulations of supersonic conical nozzle exhaust. *49th AIAA/ASME/SAE/ASEE Joint Propulsion Conference*, AIAA 2013-3697.

54. **Migdal D., and Landis F.** (1962) Characteristics of conical supersonic nozzles. *ARS Journal*, 32(12), 1898-1901.
55. **Mitra S., Chaskar M., and Phadke S.** (1981) Design and fabrication of a simple schlierenscope. *American Journal of Physics*, 49(2), 158-161.
56. **Miyajima H., Nakahashi K., Hirakoso H., and Sogame H.** (1983) Performance of a low thrust LO<sub>2</sub>/LH<sub>2</sub> engine with a 300:1 area ratio nozzle. *19th Propulsion Conference Seattle*, AIAA 1983-1313.
57. **Morinigo J.A., and Salva J.J.** (2008) Numerical study of the start-up process in an optimized rocket nozzle. *Aerospace Science and Technology*, 12(6), 485-489.
58. **Mousavi S.M., and Roohi E.** (2014) Three dimensional investigation of shock train structure in a convergent-divergent nozzle. *Acta Astronautica*, 105(1), 117-127.
59. **Mubarak A. K. and Tide P. S.** (2018) Design of a double parabolic supersonic nozzle and performance evaluation by experimental and numerical methods. *Aircraft Engineering and Aerospace Technology*, Emerald Publishers, (2018) 91(1), pp. 145-156.
60. **Munday D., Gutmark E., Liu J., and Kailasanath K.** (2009) Flow structure of supersonic jets from conical C-D nozzles. *39th AIAA Fluid Dynamic Conference, Texas*, AIAA 2009-4005.
61. **Munday D., Gutmark E., Liu J., and Kailasanath K.** (2011) Flow structure and acoustics of supersonic jets from conical convergent-divergent nozzles. *Physics of Fluids*, 23, 116102.
62. **Nallasamy M.** (1999) Survey of turbulence models for the computation of turbulent jet flow and noise. *NASA/CR*, 1999-206592.
63. **Nasuti F., Onofri M., and Martelli E.** (2007) Numerical analysis of flow separation structures in rocket nozzles. *43rd AIAA/ASME/SAE/ASEE Joint Propulsion Conference and Exhibit, Cincinnati*, AIAA 2007-5473.
64. **Nasuti F., and Onofri M.** (2009) Shock structure in separated nozzle flows. *Shock waves*, 19(3), 229-237.
65. **Nebbache A., and Pilinski C.** (2006) Pulsatory phenomenon in thrust optimized contour nozzle. *Aerospace Science and Technology*, 10(4), 295-308.
66. **Norum T.D., and Seiner J.M.** (1982) Measurements of mean static pressure and far field acoustics of shock containing supersonic jets, *NASA Technical memorandum*, 84521.



67. **Norum T.D., and Shearin J.G.** (1988) Shock structure and noise of supersonic jets in simulated flight to Mach 0.4, *NASA Technical paper*, 2785.
68. **Oosthuisen P.H., and Carscallen W.F.** (1997) Compressible fluid flow. *McGraw-Hill*, New York.
69. **Ostlund J.** (1999) Assessment of turbulence models in overexpanded rocket nozzle flow simulations. *35th Joint Propulsion Conference and Exhibit*, Los Angeles, AIAA 1999-2583.
70. **Ostlund J.** (2002) Flow processes in rocket engine nozzles with focus on flow-separation and side-loads. *Ph.D. Thesis*, Royal Institute of Technology, Stockholm.
71. **Ostlund J.** (2005) Supersonic flow separation with application to rocket engine nozzles. *Applied Mechanics Reviews*, ASME, Vol. 58.
72. **Otobe Y., Kashimura H., Matsuo S., Setoguchi T., and Kim H.D.** (2008) Influence of nozzle geometry on the near field structure of a highly underexpanded sonic jet. *Journal of Fluids and Structures*, 24(2), 281-293.
73. **Pack D.C.** (1950) A note on Prandtl's formula for the wave-length of a supersonic gas jet. *Quarterly Journal of Mechanics and Applied Mathematics*, 3(2), 1950, 173-181.
74. **Panda J.** (1998) Shock oscillation in underexpanded screeching jets. *Journal of Fluid Mechanics*, 363, 173-198.
75. **Panda J.** (1999) An experimental investigation of screech noise generation. *Journal of Fluid Mechanics*, 378, 71-96.
76. **Panda J., and Seasholtz R.G.** (1999) Velocity and temperature measurement in supersonic free jets using spectrally resolved Rayleigh scattering. *NASA /TM*, 2004-212391.
77. **Papamoschou D., Zill A., and Johnson A.** (2009) Supersonic flow separation in planar nozzles. *Shock waves*, 19(3), 171-183.
78. **Pilinski C., and Nebbache A.** (2004) Flow separation in a truncated ideal contour nozzle. *Journal of Turbulence*, 5(5).
79. **Puckett A.E.** (1946) Supersonic nozzle design. *Journal of Applied Mechanics*, 13(4), A265-A270.
80. **Raltson A., and Rabinowitz A.** (1985) A first course in numerical analysis. *McGraw-Hill Book Company*.

81. **Ramsey M.C., Pitz R.W., Jenkins T.P., Matsutomi Y., Yoon C., and Anderson W.E.** (2012) Planar 2D velocity measurements in the cap shock pattern of a thrust optimised rocket nozzle. *Shock waves*, 22, 39-46.
82. **Rao G.V.R.** (1958) Exhaust nozzle contour for optimum thrust. *Journal of Jet Propulsion*, 28(6), 377-382.
83. **Rao G.V.R.** (1960) Approximation of optimum thrust nozzle contour. *ARS Journal*, 3(6), 561.
84. **Rao G.V.R.** (1962) Recent developments in rocket nozzle configurations. *ARS Journal*, 31(11), 1488-1494.
85. **Rao S.M.V., Asano S., and Saito T** (2016) Comparative studies on supersonic free jets from nozzles of complex geometry. *Applied Thermal Engineering*, 99, 599-612.
86. **Rathakrishnan E.** (2010) Applied gas dynamics, *John Wiley*.
87. **Reijasse P., Morzenski L., Blacodon D., and Birkemeyer J.**(2001) Flow separation experimental analysis in overexpanded subscale rocket nozzles. *37th Joint Propulsion Conference and Exhibit*, Salt Lake City, AIAA 2001-3556.
88. **Richard H., and Raffel M.** (2001) Principle and applications of the background-oriented schlieren (BOS) method. *Measurement Science and Technology*, 6, 1576-1585.
89. **Samitha Z.A., Swaraj Kumar, and Balachandran P.** (2007) Experimental study on supersonic mixing using clover nozzle. *45th AIAA Aerospace Science Meeting and Exhibit*, Reno, AIAA 2007-839.
90. **Schomberg K., Olsen J., Neely A. and Doing G.** (2015) Suppressing restricted shock separation in thrust-optimized rocket nozzles using contour geometry. *51st AIAA/SAE/ASEE Joint Propulsion Conference*, AIAA 2015-4220.
91. **Seiner J.M, and Norum T.D.** (1980) Aerodynamic aspects of shock containing jet plumes. *6th Aeroacoustics Conference*, Hartford, AIAA 1980-0965.
92. **Seiner J.M., and Gilinsky M.M.** (1997) Nozzle thrust optimization while reducing jet noise. *AIAA Journal*, 35(3), 420-427.
93. **Settles G.S.**(2006) Direct Schlieren and shadowgraph techniques: Visualizing phenomena in transparent media. *Springer*, 2nd edition.
94. **Shih T.H., Liou W.W., Shabbir A., Yang Z., and Zhu J.** (1995) A new  $k-\epsilon$  eddy-viscosity model for high Reynolds number turbulent flows - Model development and validation. *Computational Fluids*, 24(3), 227-238.

95. **Shmyglevsky Yu. D. (1958)** Supersonic profiles with minimum drag. *Prikl. Mat. Mekh.* 22, 2, 269-273.
96. **Shirie J.W., and Seubold J.G. (1967)** Length of the supersonic core in high-speed jets. *AIAA Journal*, 5(11), 2062-2064.
97. **Shope F.L. (2006)** Contour design techniques for super/hypersonic wind tunnel nozzles. *24th Applied Aerodynamics Conference*, Sanfrancisco, AIAA 2006-3665.
98. **Spotts N., Guzik S., and Gao X. (2013)** A CFD analysis of compressible flow through convergent-conical nozzles. *49th AIAA/ASME/SAE/ASEE Joint Propulsion Conference*, AIAA 2013-3734.
99. **Stark R., Bohm C., Haiden O.J., and Zimmermann H. (2006)** Cold flow testing of dual-bell nozzles in altitude simulation chambers. *European Conference for Aerospace sciences*, DLR, German Aerospace Center.
100. **Sternin L.E. (2000)** Analysis of the thrust characteristics of jet nozzles designed by various methods. *Fluid dynamics*, 35(1), 123-131.
101. **Sternin L.E. (2003)** Calculating the thrust characteristics of nozzles from their outlet cross-section parameters. *Fluid Dynamics*, 38(1), 153-163.
102. **Sutton G.P., and Biblarz O., (2010)**, Rocket propulsion elements. *John Wiley & Sons*, 7th edition.
103. **Suzuki H., Endo M., and Sakakibara Y. (2013)** Structure and oscillation of underexpanded jet. *Open Journal of Fluid Dynamics*, (3), 85-91.
104. **Taha A., Tiwari S., and Mohieldin T. (2001)** Validation of Fluent CFD code in supersonic flow fields. *15th AIAA Computational Fluid Dynamics Conference*, AIAA 2001-2637.
105. **Terhardt. M., Hagemann G., and Frey M. (1999)** Flow separation and side load behaviour of the Vulcain engine. *AIAA paper*, AIAA 99-2762.
106. **Thornock R.L., and Sokhey J. S. (2013)** Propulsion aerodynamic workshop I, Comparison of participant analysis with experimental results for convergent conical nozzle flow fields and performance. *49th AIAA/ASME/SAE/ASEE Joint Propulsion Conference*, AIAA 2113-3735.
107. **Tide P.S., and Babu V. (2009)** Improved noise predictions from subsonic jets at Mach 0.75 using URANS calculations. *Progress in Computational Fluid Dynamics*, 9(8), 460-474.
108. **Tropea C., Yarin A.L., and Fross J.F. (2007)** Springer handbook of experimental fluid mechanics.

109. **Venkatapathy E., and Feiereisen W.J.** (1988) 3-D Plume flow computations with an upwind solver. *24th Joint Propulsion Conference*, Boston, AIAA 1988-3158.
110. **Verma S.B., and Ciezki H.K.** (2003) Unsteady nature of flow separation inside a thrust optimized parabolic nozzle. *41st Aerospace Science Meeting and Exhibit, Reno*, AIAA 2003-1139.
111. **Verma S.B., and Haidn O.** (2009) Study of restricted shock separation phenomena in thrust optimized parabolic nozzle. *Journal of Propulsion Power*, 25(5), 1046-1057.
112. **Verma S.B., and Koppenwallner G.** (2002) Unsteady separation in flare-induced hypersonic shock wave boundary layer interaction flow field. *Journal of space crafts and rockets*, 9(3), 467-470.
113. **Versteeg H., and Malalasekera W.** (1995) An Introduction to Computational Fluid Dynamics: The Finite Volume Method. Second Edition, *Pearson Education Ltd.*
114. **Weiss A., Grzona A., and Oliver H.** (2010) Behaviour of shock trains in a diverging duct. *Experiments in Fluids*, 49(2), 355-365.
115. **Wilson B.M., and Smith B.L.** (2013) Uncertainty on PIV mean and fluctuating velocity due to bias and random errors, *Measurement Science and Technology*, 24(3):035302.
116. **Yakhov V., Orszag S.A., Thangam S., Gatski T.B., and Speziale C.G.** (1992) Development of turbulence models for shear flows by a double expansion technique. *Physics of Fluids A: Fluid Dynamics*, 4(7), 1510-1520.
117. **Yang V., Habiballah M., Hulka J., and Popp M.** (2004), Liquid rocket thrust chambers: Aspects of modeling, analysis and design. *Progress in Astronautics and Aeronautics Inc., Virginia*, volume 200.
118. **Yen J.C., and Martindale W. R.** (2008) An inviscid supersonic nozzle design approach to perfect flow uniformity for wind tunnel applications. *26th AIAA Applied Aerodynamics Conference, Hawaii*, AIAA 2008-7059.
119. **Yonezawa K., Morimoto T., Tsujimoro Y., Watanabe Y., and Yokota K.** (2007) A study of an axisymmetric flow in an overexpanded rocket nozzle. *Journal of Fluid Science and Technology*, 2(2), 400-409.
120. **Zapryagaev V., Kiselev N. and Gubanov D.** (2018) Shock-wave structure of supersonic jet flows. *Aerospace*, 5 (2018), 60.
121. **Zebbiche T.** (2006) New generalized form of the Prandtl Meyer function application for air at high temperature. *25th Applied Aerodynamic Conference, Sanfrancisco*, AIAA 2006-3674.

122. **Zebbiche T.** (2007) Stagnation temperature effect on the Prandtl Meyer function. *AIAA journal*, 45(4), 952-954.
123. **Zebbiche T.** (2011) Stagnation temperature effect on the supersonic axisymmetric minimum length nozzle design with application for air. *Advances in Space Research*, 48, 1656-1675.
124. **Zebbiche T., and Youbi Z.** (2006) Supersonic plug nozzle design at high temperature application for air. *44th Aerospace Science Meeting and Exhibit, Reno Nevada*, AIAA 2006-0592.
125. **Zhu Y., and Jiang P.** (2014) Experimental and analytical studies on the shock wave length in convergent and convergent-divergent nozzle ejectors. *Energy Conversion and Management*, 88, 907-914.
126. **Zucker R.D. and Biblarz O.** (2002) Fundamentals of Gas Dynamics. 2nd edition, *John Wiley and Sons*, New York.

## **LIST OF PUBLICATIONS**

### **SUBMITTED ON THE BASIS OF THESIS**

#### **REFEREED JOURNALS**

1. Mubarak A. K., Tide P. S. “Experimental and Computational Exploration of Under expanded Jets from Conical, Bell and Double Parabolic nozzles”, *International Review of Mechanical Engineering*, Praise Worthy Prize Publishers, Vol. 12, No. 1, (2018) pp. 33-41 (Scopus indexed).
2. Mubarak A. K., Tide P. S. “Design of a Double Parabolic Supersonic Nozzle and Performance Evaluation by Experimental and Numerical Methods”, *Aircraft Engineering and Aerospace Technology*, Emerald Publishers, (2018) Vol. 91, No.1, pp. 145-156 (Scopus indexed).

#### **PRESENTATIONS IN INTERNATIONAL CONFERENCES**

1. “Review on the Application of Ablative Materials for Solid Rocket Motor Nozzles and their Fabrication”, Mubarak A. K., Sandhya M., Tide P. S., Second International Conference on Materials for the Future - Innovative Materials, Processes, Products and Applications- ICMF 2011, pp. 205-209.
2. “Review on the Drag Reduction Technologies in Aircraft”, Mubarak A. K., Tide P. S., Proceedings of International Conference on Materials for the Future - Innovative Materials, Processes, Products and Applications- ICMF 2013, pp. 221-224.
3. “Estimation of Performance of Turbulence Models in Imperfectly Expanded Jets from a Convergent Divergent Nozzle”, Mubarak A. K., Jaison K. A., Tide P. S., International Conference on Energy, Environment, Materials and Safety ICEEMS 2014, pp. 471-476.

## **CURRICULUM VITAE**

1. Name : **MUBARAK A. K.**
2. Date of Birth : 12.05.1973

### **3. Educational Qualifications**

#### **1995 Bachelor of Technology (BTech)**

Institution : Government Engineering College Trichur, Kerala.  
University of Calicut

Specialization : Mechanical Engineering

#### **2007 Master of Technology (MTech)**

Institution : National Institute of Technology, Calicut, Kerala  
Specialization : Energy Management

#### **Doctor of Philosophy (PhD)**

Institution : Cochin University of Science and Technology Kochi,  
Kerala

Registration Date : 12.10.2010